Università degli studi di Catania
Dottorato di Ricerca in Fisica

Tesi per il conseguimento del titolo

N/Z Effects on Nuclear Reactions Near the Fragmentation Threshold

Tutors

Prof. Francesco Porto
Dr. Giuseppe Cardella

Candidato

Ivano Lombardo

Coordinatore Ph.D.

Prof. F. Riggi

Ciclo XXIII - 2007/2010

Contents

Introduction

The study of heavy-ion collisions represents one of the most fascinating subjects in Nuclear Physics. From nuclear reactions involving heavy nuclei, a large amount of information can be derived. Elastic and inelastic scattering, multi-nucleon transfer, fusion and incomplete fusion, deeply-inelastic and dissipative mechanisms: all these subjects contribute to a deeper understanding of nuclear structure and reaction mechanisms.

Many open questions are nowadays unsolved. One of them concerns the role played by the neutron to proton ratio (N/Z) degree of freedom on dynamics and thermodynamics of heavy-ion nuclear reactions near multifragmentation threshold ($\approx 20 - 30$ MeV/nucleon). Many questions arise from the analysis of central and mid-peripheral collisions. Does the N/Z degree of freedom influence the production of evaporation residues? Are the thermodynamical parameters characterizing quasi-fusion sources influenced by N/Z? In mid-peripheral collisions, does N/Z distribute uniformly throughout the formed di-nuclear system? In Chapter 1 I will describe briefly these questions, in light of results achieved in past and recent scientific literature.

To investigate on N/Z effects on physical observables, many nuclear reactions involving medium mass nuclei (mainly Calcium isotopes) at 25 MeV/nucleon bombarding energy have been performed and analyzed. To detect the reaction products emitted in the output channels, we used the Chimera 4π detector. Details on the experimental apparatus, together with the characterization of newly developed detectors coupled to the Chimera array are discussed in Chapter 2.

Chapter 3 focuses on the main results obtained from the data analysis of $^{40}Ca +^{40} Ca$ (N/Z=1.0), $^{40}Ca +^{46} Ti$ (N/Z=1.05) and $^{40}Ca +^{48} Ca$ (N/Z=1.2) reactions at 25 MeV/nucleon. The large N/Z range explored by the projectile and target nuclei in the entrance channel allows to perform investigations on the influence of the N/Z degree of freedom on physical observables in inclusive, central and mid-peripheral events.

In the case of central collisions, incomplete fusion was studied and a strong influence of N/Z of entrance channel of the reaction on the competition between evaporation residues and binary-like emission is observed. In particular, for the neutron rich reaction, $^{40}Ca +^{48} Ca$, evaporation residue emission is enhanced; at variance, for symmetric $N \approx Z$ systems, binary-like phenomena prevail. This effect can be attributed to the strong interplay between Coulomb and symmetry term in nuclear equation of state. In this light, the dynamics of nuclear reactions near the fragmentation threshold seems to be strongly influenced by the N/Z degree of freedom. Comparison of our experimental data to dynamical calculations performed with CoMD-II model allows to extract information about the stiffness of the density dependence of the symmetry potential at sub-saturation densities.

I also analyzed thermodynamical features characterizing the hot sources produced in incomplete fusion events. Apparent temperatures are estimated by means of a moving source analysis of kinetic energy spectra of protons emitted in coincidence with evaporation residues and by using the method of double isotope ratios. For quasi-fusion events, the excitation energy was estimated event by event by using a calorimetric procedure. Despite of the large variation of N/Z in the entrance channel, the measured thermodynamical parameters are quite similar. It seems therefore that the N/Z degree of freedom has only a weak influence on the measured thermal parameters.

In the case of mid-peripheral collisions, I studied isospin diffusion and drift phenomena by analyzing the behavior of isotopic and isobaric ratios of light nuclei, such as $^{6,7}Li$ and $^{7,9}Be$. The analysis of quasi-projectile emission seems to testify a net neutron exchange from ^{48}Ca targets to ^{40}Ca projectiles, validating an isospin diffusion scenario. Mid-velocity emission seems to be neutron enriched compared to quasi-projectile sources, even in the case of symmetric $^{40}Ca +^{40} Ca$ reaction. This effect can be attributed to the isospin drift phenomenon occurring in the mid-velocity region of the phase space.

In Chapter 4 I will show results obtained by studying the reaction system $^{48}Ca +^{48} Ca$ (N/Z=1.4) at 25 MeV/nucleon, characterized by a very large neutron excess. After a brief presentation of inclusive observables (such as isotopic and charge distributions at forward angles), I will discuss the behavior of central incomplete fusion events in details. A strong enhancement in the emission of evaporation residues to the detriment of binary-like phenomena is seen. The overall study of all combinations of $^{40,48}Ca +^{40,48} Ca$ reactions is also discussed. The experimental results strongly confirm the key role played by the N/Z degree of freedom on fusion dynamics near fragmentation threshold, opening the perspective for further investigations with radioactive beams at low and near-Fermi energies.

Chapter 1

Incomplete Fusion of Heavy Ions

The growth of heavy ion physics started during the '70s and represented one of the most important and fascinating chapters among the various topics of Nuclear Physics [1]. Many topics were investigated: attempts to synthesize transuranic elements, the search for limits of existence for excited nuclear systems, the description of multi-nucleon transfer phenomena and generally the comprehensive understanding of Nuclear Dynamics involved in collisions between heavy ions. The golden age of heavy ion science could be fixed, based on the number of citation of the most important papers produced, since 1984 (*Physical Review Letters* article by Bohne, Morgenstern et al. on incomplete fusion [2]) until 1995 (*Physical Review Letters* by ALADiN collaboration on nuclear phase transition [3]). The experimental work described in the following sections will focus especially on dynamics and thermodynamics of heavy ion reactions at 25 MeV/nucleon. For this reason, we will briefly describe along this chapter typical processes dominating nuclear reactions at 20-30 MeV/nucleon, i.e. around the so-called multi-fragmentation threshold.

1.1 Incomplete Fusion Phenomena near 20 MeV/nucleon

A pictorial view of the evolution of reaction mechanisms as a function of the impact parameter in heavy ion collisions at near-barrier energies is shown on Figure 1.1. Distant and Peripheral collisions are characterized by elastic and inelastic scattering, while deep inelastic phenomena are typical of grazing trajectories [1]. Central collisions involving medium mass nuclei (with $A \leq 100$) at bombarding energies above the Coulomb Barrier (few MeV/nucleon) lead essentially to complete fusion [4]. This process is characterized by the formation of a single compound nucleus, due to the merging of the two mean

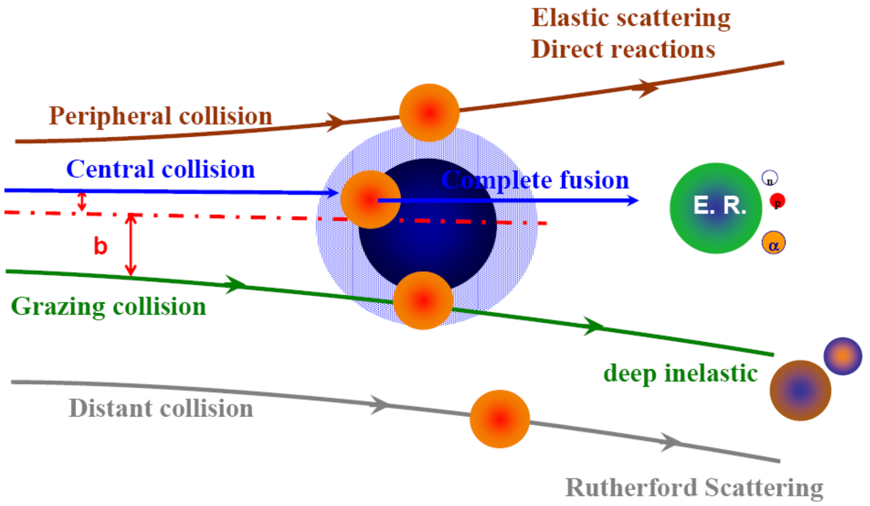

Fig. 1.1: Scheme of the various reaction mechanisms characterizing low energy heavy ion reactions, as a function of impact parameter of the collision (b).

fields of projectile and target. The compound nucleus formed is excited; it may de-excite by emitting only γ rays (in this case, typical of near-barrier energies, the phenomenon is called heavy ion *radiative capture* [5]) or by emitting light particles such as neutrons, protons and α particles, followed by γ ray emission. As a key example, in Figure 1.2 we plot the mass-kinetic energy correlation (in the laboratory frame) for nuclei emitted at 10° in the reaction $^{20}Ne +^{26} Mg$ at 6 MeV/nucleon [6]. Two contributions are clearly visible: the first one, involving nuclei in the region of $A \simeq 20$ and $E_{Lab} \simeq 100MeV$, is due to quasi-elastic phenomena (few nucleon transfer etc.); the second one, dominating the scatter plot, concerns the emission of nuclei with $A \simeq 35$. They are evaporation residues emitted in complete fusion events (in the parameterization suggested by Bass [7], the complete fusion cross section is about 1000 millibarn). In this bombarding energy regime, near the Coulomb Barrier, calculations performed with statistical models and based on Hauser-Feshbach or Thomas-Porter approaches (such as CASCADE, LILITA, JULIAN and PACE) reproduce quite well the emission yields of the different evaporation residues [6, 8].

When the beam energy exceeds 7-10 MeV/nucleon, the velocity of the projectile nucleus becomes noticeably high, and the interaction times between the overlapping projectile and target nuclei become short (few hundreds of fm/c). As an example, let us consider the "historical" case of $^{20}Ne +^{40} Ca$ at 14.5 MeV/nucleon discussed in ref. [9]. The ^{20}Ne projectile is a quite light nucleus having a pronounced alpha particle structure.

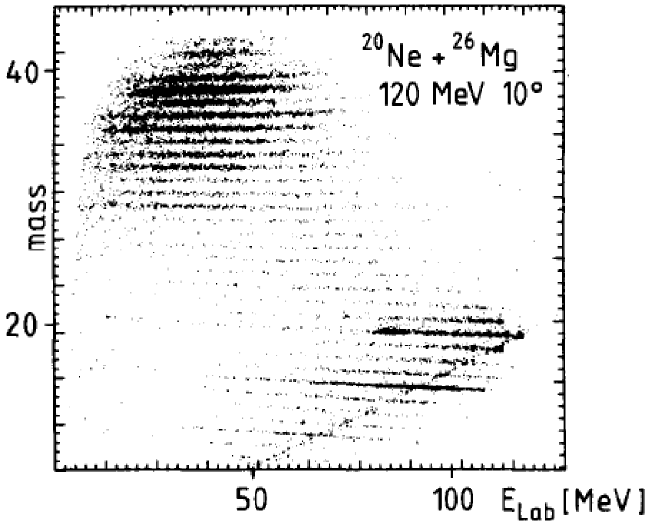

Fig. 1.2: Mass-kinetic energy correlation for the largest nuclei emitted at $\theta = 10°$ in laboratory frame, in $^{20}Ne+^{26}Mg$ reaction at 6 MeV/nucleon [6]. Contributes due to peripheral collisions (quasi-elastic events, $A \simeq 20$) and fusion events ($A \simeq 35$) are distinguishable.

In semi-central collisions, this projectile can undergo a rapid break-up when it enters in the mean field of ^{40}Ca target. Moreover, one of the nuclei formed in the projectile break-up (generally, the largest) can be attracted by the target nucleus to form a quasi-compound system, leading to the so-called "incomplete fusion" phenomena (see Figure 1.3). The mass of this quasi-compound system would be clearly lower than the mass of the compound nucleus formed in complete fusion events. The excitation energy reached by these quasi-compound systems can be estimated by using the momentum conservation law (*linear momentum transfer*) [10]. A deep understanding of incomplete fusion was achieved by means of kinematical studies on the recoil velocities of the evaporation residues, although signals of the presence of incomplete fusion processes were found two decades before in the pionieristic work of Britt and Quinton [11]. In the '70, moreover, a japanese group deduced the existence of this process by means of gamma ray spectroscopy studies [12].

In Figure 1.4 we show the invariant velocity spectrum of recoiling evaporation residues emitted in $^{20}Ne +^{27} Al$ collision. Experimentally, velocity spectra were obtained by using an high-resolution time of flight spectrometer at the `HMI` facility in Berlin [2]. The presence of complete fusion mechanisms would be characterized by velocity spectra peaked near the compound nucleus recoil velocity ($v - v_{CN} \simeq 0$). Instead data show velocity spectra peaked at velocities lower than the compound nucleus velocity. By applying

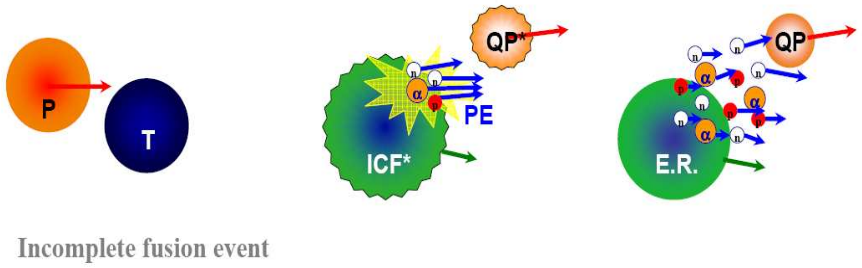

Fig. 1.3: Pictorial view of a typical incomplete fusion event, involving a massive transfer from the projectile to the target nucleus. P and T indicate projectile and target nuclei. QP represents the quasi-projectile source. PE stays for the pre-equilibrium emission. ICF indicates the incomplete fusion source. ER is the evaporation residue resulting from the de-excitation of incomplete fusion source.

momentum conservation, this is an indication that only a fraction of the projectile momentum is transferred to the quasi-compound system, while a fast and light quasi-projectile partner flies at near beam velocity (see also Figure 1.3).

In the specific case of Figure 1.4, only 43% of the spectrum could be associated to complete fusion mechanisms; the remaining (dominating) part is due to incomplete fusion events. Similar conclusions were drawn from reaction studies in direct kinematics, such as $^{20}Ne +^{40} Ca$, and in inverse kinematics, such as $^{40}Ar +^{12} C$, at bombarding energies between 10 and 20 MeV/nucleon [2, 9]. It is interesting to underline that it was more difficult to extract information about incomplete fusion phenomena for symmetric kinematics reactions, such as $^{40}Ar +^{40} Ca$, when the experiment was performed inclusively [2]. In this case, in fact, the velocity spectrum was always peaked near the compound velocity. For symmetric systems, as $^{28}Si +^{28} Si$ or $^{40}Ca+^{40}Ca$, further details were obtained only when it was possible to detect in coincidence evaporation residues and quasi-projectile or quasi-target partners of incomplete fusion events [13].

In ref. [2] the authors extracted the maximum quasi-projectile velocity beyond which complete fusion ceases to exist ($v_P \simeq 0.2c, E \simeq 20$ MeV/nucleon). When $v_P \simeq 0.06c$ complete fusion is gradually replaced by incomplete fusion; in the range $0.06 \lesssim \frac{v_P}{c} \lesssim 0.2$ there is coexistence of complete and incomplete fusion [14], and experimentally it is difficult to separate the contributions of the two mechanisms [15]. Above $v_P \approx 0.2c$, for semi-central collisions of medium mass nuclei, incomplete fusion dominates up to the limit of Fermi Energies domain ($\approx$ 35 MeV/nucleon) [16]. Near 30 MeV/nucleon, in fact, the available energy in center of mass becomes quite high, while interac-

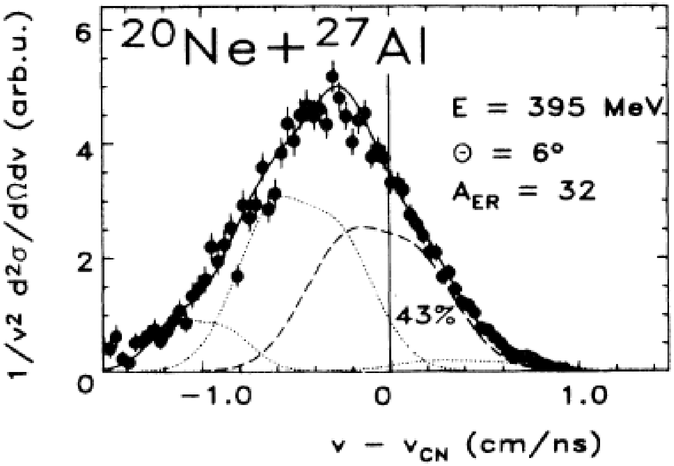

Fig. 1.4: Velocity distribution of evaporation residues (with A=32) emitted in ^{20}Ne+^{27}Al reaction at 20 MeV/nucleon, at a polar angle $\theta = 6°$ [2]. Only a limited fraction of fusion residues can be ascribed to complete fusion events (dashed line).

tion times are noticeably shorter; emission of fast protons and α particles in the first phases of the collision can be observed, while the intermediate system formed in the first phase of the collision is interested by instability phenomena that lead to fragmentation (multi-fragment emission) [17]. We recall that all the conclusions reported in this paragraph are valid for medium mass nuclei ($A < 60$); in nuclear reactions involving heavier nuclei we cannot neglect the contribution due to fusion-fission, at least for the most peripheral reactions (highest angular momentum [4]). We underline moreover that, due to its binary nature, incomplete fusion was considered as an extension of deep inelastic collisions at higher bombarding energies and for semi-central impact parameters. Nevertheless, the two processes are quite different, because the quasi-projectile acts as a "spectator" in incomplete fusion events, while in DIC both the partners are strongly modified by the reaction mechanism.

Let us consider now the system $^{40}Ca + ^{40}Ca$ at 35 MeV/nucleon [18]; in Figure 1.5 charge distribution for nuclei emitted in the most violent collision (low impact parameters) is shown. The absence of evaporation residues is quite evident, while the presence of fragments and light particles, with charges from Z=20 up to Z=1 is dominant. For systems at Fermi Energies, the largest part of events is therefore dominated by the production of intermediate mass fragments. The observed mean fragment multiplicity was between 2 and 3. However, for the most violent collisions, we can recognize events where the emission of six fragment is observed. Experimental charge distributions are sufficiently well reproduced only by using dynamical calcu-

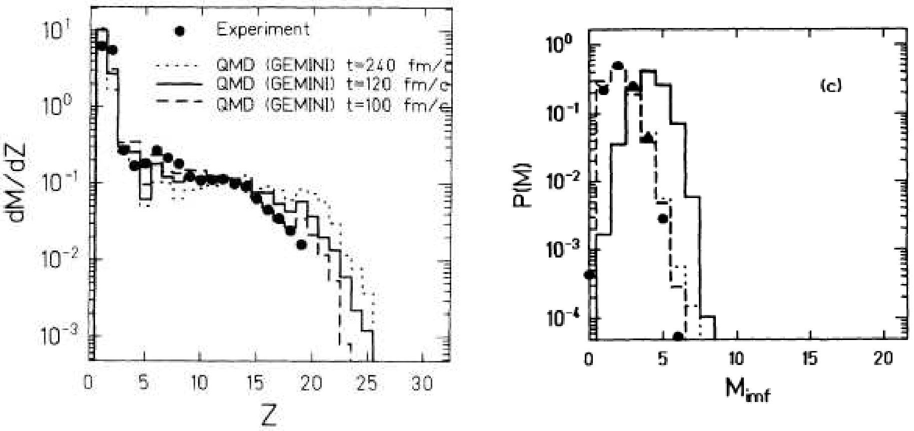

Fig. 1.5: (Left) Charge distribution of fragments emitted in the most violent collisions of $^{40}Ca+^{40}Ca$ reaction at 35 MeV/nucleon; QMD+GEMINI calculations are also shown. In detail, calculations have been obtained by varying the starting time of the statistical de-excitation phase (studied with GEMINI). Dynamical phases of reaction were simulated by QMD code. (Right) Multiplicity spectrum of emitted fragments in the most central collisions of the reaction before mentioned.

lations (in particular, in this case the authors used the Quantum Molecular Dynamics QMD model [19]) that describes the first phase of collision in a reasonable way. After the dynamical phase (followed up to 240, 120 and 100 fm/c in the calculation of ref. [18]), the de-excitation of produced fragments is simulated by means of statistical models, such as GEMINI [20].

At the end of this short introduction, it is clear that nuclear reactions involving medium mass nuclei ($A \approx 50$) at bombarding energies near 20 MeV/nucleon constitute a very interesting benchmark of nuclear dynamics, because a transition in the dominating reaction mechanisms appears. In particular, as soon as one enters the Fermi Energies domain, incomplete fusion reactions (characterized by the production of evaporation residues) are replaced by multi-fragmentation reactions (where many fragments are emitted in the exit channel) [21]. This transition in reaction mechanisms has been interpreted both by introducing a limiting excitation energy sustainable by hot nuclei (Sect. 2.2) and by considering that, at Fermi Energies, nuclear matter enters the *spinodal region* of nuclear phase diagram. In this region, large density fluctuations can lead to the fragmentation of nuclear systems [21]. Nowadays, the knowledge of the limits of existence of excited nuclei populated in heavy ion reactions constitutes one of the challenges in nuclear physics.

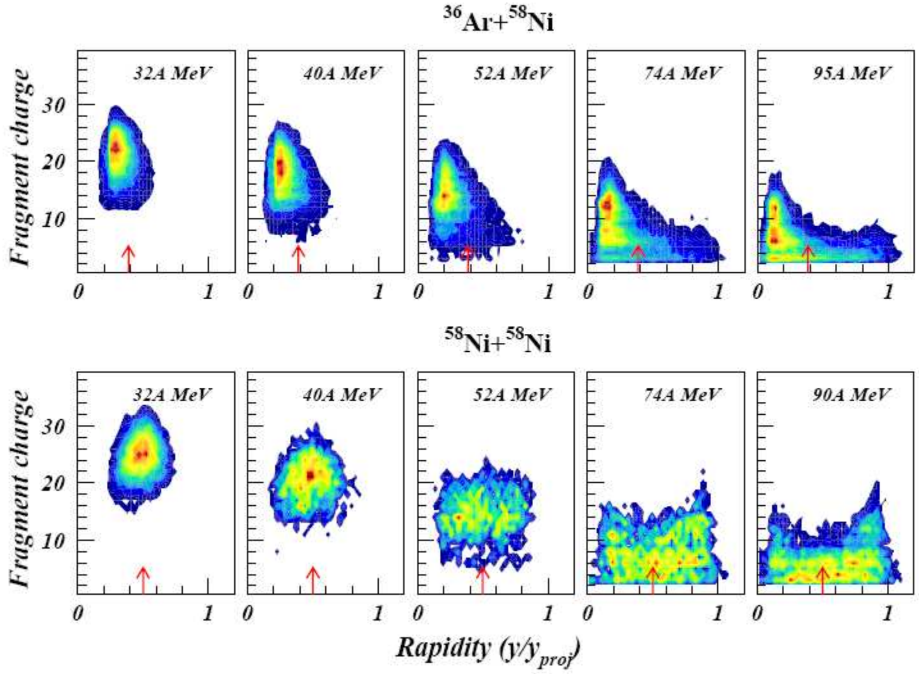

Fig. 1.6: Charge-rapidity correlation of largest nucleus emitted in semi-central collisions of $^{36}Ar,^{58}Ni+^{58}Ni$ reactions at various bombarding energies, from 32 to 95 MeV/nucleon. Data obtained by INDRA collaboration. Adapted from ref. [22].

1.1.1 Incomplete Fusion: present status

The development of high-performances multi-detectors allows to deeply understand incomplete fusion mechanisms. Indeed, these detector arrays allow one to perform exclusive investigations on various aspects related to this phenomenon. In this respect, an interesting study was performed by the INDRA collaboration at GANIL. In this experiment evaporation residues production as a function of bombarding energy and for different medium mass systems was investigated. More in details, they analyzed the collisions $^{36}Ar+^{58}Ni$ and $^{58}Ni+^{58}Ni$ from 32 to 95 MeV/nucleon. In Figure 1.6 charge-rapidity correlations for the largest fragment emitted in each event of reaction are shown [22].

It appears that the presence of incomplete fusion mechanisms, dominating at 32 and 40 MeV/nucleon, drops out at bombarding energies larger than 50 MeV/nucleon. In the same article a compilation of systematic data on the ratio between fusion (complete+incomplete) cross section versus reaction cross section ($\frac{\sigma_{fus}}{\sigma_r}$) as a function of the bombarding energy for various medium mass systems is reported (Figure 1.7).

From Figure 1.7 we can see that the fusion cross section (including both

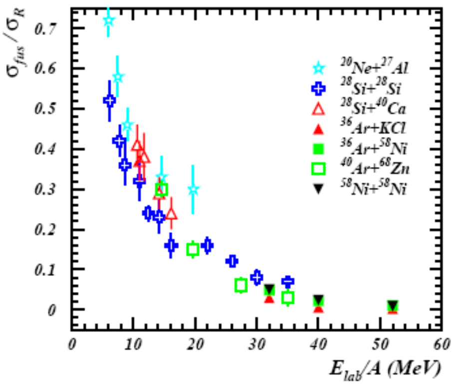

Fig. 1.7: Ratio between evaporation residue cross section (complete+incomplete fusion) and total reaction cross section as a funtion of bombarding energies, for medium mass systems ($30 \lesssim A \lesssim 60$) having various mass asymmetries in entrance channels. From ref. [22]. Emission of residues drops out rapidly; it becomes less than 10% of the total reaction cross section overcoming 30 MeV/nucleon bombarding energy.

complete and incomplete fusion contributions) goes from ≈50% of the total reaction cross section at 8 MeV/nucleon up to a few percent at bombarding energies above 40 MeV/nucleon. The mass asymmetry of the entrance channel seems to play only a secondary role in evaporation residue emission. The main parameter affecting the ratio $\frac{\sigma_{fus}}{\sigma_r}$ is the bombarding energy. At bombarding energies near 20 MeV/nucleon, $\frac{\sigma_{fus}}{\sigma_r} \simeq 0.15$.

In semi-central collisions other phenomena could coexist with the incomplete fusion ones. More in details, these are binary-like events, an extension of deep inelastic phenomena to higher energies. The coexistence between these two phenomena is possible because, near 20 MeV/nucleon, the interaction time between projectile and target nuclei is relatively long and various mean-field modes can be simultaneously present [23]. For this reason, the present knowledge about mean-field dynamics and, in general, about fundamental properties of nuclear forces can be improved by studying the competition between these two phenomena. These investigations have been considered one of the unsolved questions in nuclear physics.

In Chapters 3 and 4 I will discuss experimental results obtained during my Ph.D. work. In particular, I will show that the N/Z degree of freedom plays a fundamental role in the production of evaporation residues in incomplete fusion events. The comparison of the experimental results with dynamical calculations allowed us to extract new details about the poorly known behavior of the density dependent part of the symmetry potential, at densities near saturation (see also Sect. 1.3.2).

1.1.2 Light particles emitted by thermalized systems

Nuclear systems formed by means of complete or incomplete fusion are characterized by large values of excitation energy, due to the strong kinetic energy damping. In order to de-excite, these systems typically emit light particles such as neutrons, α particles, protons, deuterons, tritons and heavier ones. In this way, after the whole de-excitation chain, the initial hot system losses a sizeable part of its mass and excitation energy, down to an excitation energy below its particle emission threshold. At this point, the system de-excites down to ground state by emitting low-energy gamma rays [4]. The shape of the energy spectra of light particles emitted in a de-excitation cascade is typical of systems in thermodynamical equilibrium. In fact, their energy spectra can be parameterized as a Maxwellian function in the reference frame of the emitting source [24]. In the laboratory frame, these Maxwellian functions for charged particles are described as:

$$\frac{d^2N}{dEd\Omega} = N\sqrt{E-E_c} \times \exp[-\frac{E-E_c+E_S-2\sqrt{(E-E_c)E_S}\cos\theta}{T}] \quad (1.1)$$

where N is a normalization constant linked to the emission yield, E_S is the kinetic energy of the moving source in the laboratory frame, E_c is the Coulomb barrier, θ is the polar angle of emission in the laboratory frame and T is the slope of the Maxwellian that could represent the apparent temperature of the emitting source [24, 25]. Neutrons do not experience the effects of the Coulomb barrier. For this reason, their spectra are described by Equation 1.1 with $E_c = 0$. In the case of collisions leading to complete fusion, light particles energy spectra (especially neutrons, protons and α particles) show almost purely Maxwellian shapes. Then the slope parameter T obtained by fitting the experimental data with Equation 1.1 represents the apparent temperature of the hot compound nucleus formed in the reaction [1]. The concept of ”nuclear temperature” will be discussed in details in the next sections.

In Figure 1.8 light particles spectra (n, p, α) detected in coincidence with evaporation residues in $^{35}Cl +^{24} Mg$ reactions at 260 MeV bombarding energy are reported. The experimental data are quite well reproduced by a single component moving source with a Maxwellian shape. An apparent temperature around 2.5 MeV has been extracted from these spectra [26].

By increasing the bombarding energy, it has been observed that the shape of light particle energy spectra can not be fitted with one Maxwellian function. More in details, the spectra measured at forward angles show an additional contribution as compared to the case of emissions at backward angles. As an example, in $^{32}S +^{58} Ni$ collisions at 30 MeV/nucleon [27], the spectra at backward angles ($\theta > 90°$) can be fitted by using a single Maxwellian function (in direct kinematics, this angular region is dominated

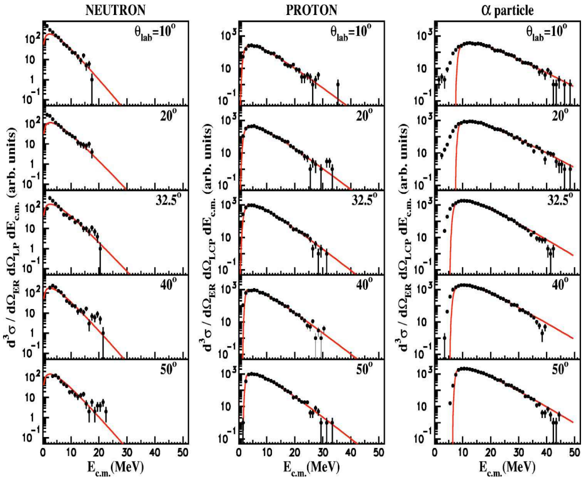

Fig. 1.8: Light particles spectra (neutrons, protons and αs) emitted at various polar angles (in laboratory frame) in coincidence with fusion residue with charge Z=22 at $\theta = -10°$ in $^{35}Cl + ^{24}Mg$ reaction at 7.4 MeV/nucleon. Red line represents the fit performed with a single Maxwellian moving source that takes into account the mission due to complete fusion source. From ref. [26].

by the emission from the equilibrated fusion source); at variance, the presence of another emitting source was recognized by measuring spectra at forward angles (see figure 1.9). This additional contribution was generally termed as "pre-equilibrium" [27] to indicate emissions that can not be attributed to equilibrated fusion or incomplete-fusion sources. In the next Section we will see that the term "pre-equilibrium" has been associated to phenomena having very different origins (emission due to the weakly excited quasi-projectile, nucleon-nucleon collisions in the medium, etc). Below ≈ 10 MeV/nucleon bombarding energies, nucleon-nucleon collisions in the nuclear medium do not lead to the direct emission of nucleons due to the Pauli principle. For this reason, in this energy domain the non-fusion contribution can originate only from a weakly excited quasi-projectile emitting source.

Experimental data confirmed these hypotheses. Extra-yields of protons, neutrons and α particles observed in their spectra at forward angles can be reproduced by introducing a second Maxwellian, moving with a velocity near to the projectile one and characterized by an apparent temperature noticeably lower than that of the fusion source [28]. Above 15 MeV/nucleon bombarding energies, nucleon-nucleon collisions in the medium can lead to a direct emission of protons and neutrons. This leads to the presence of another contribution to neutron and proton kinetic energy spectra. The currently used parameterizations of such emissions will be discussed in the following section.

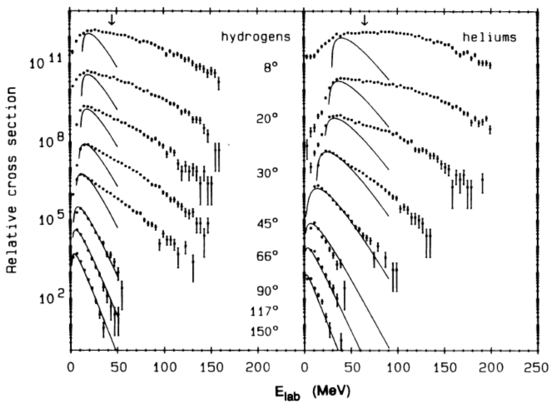

Fig. 1.9: Energy spectra of hydrogen and helium isotopes emitted at various polar angles in incomplete fusion events of $^{32}S + ^{58}Ni$ reaction at 30 MeV/nucleon. The most backward spectra are fitted by a single Maxwellian moving source (contribute of quasi-fusion source); at variance, spectra of particles emitted at forward angles show more complex shapes. From ref. [27]

1.1.3 One-body and two-body pre-equilibrium

Historically, ”pre-equilibrium emissions” have been attributed to those phenomena involving particles not participating in the formation of quasi-fused compound in incomplete fusion phenomena and emitted before thermalization [29]. This generic definition must be refined by considering that there are two main categories of pre-equilibrium emissions: the first one involves one-body phenomena, the second one is correlated to two-body effects.

”One-body pre-equilibrium” is ascribed to the interaction of many nucleons within the nuclear mean field. All phenomena reported in literature as *promptly emitted particles (PEP), fast projectile break-up, Fermi jets* are one-body pre-equilibrium phenomena and demonstrated the existence of a quasi-projectile partner in incomplete fusion events. The experimental evidences for these phenomena was reported in refs. [16, 30]. For clarity reasons in the following sections we will indicate such emissions as quasi-projectile emission in incomplete fusion events.

”Two body pre-equilibrium” effects are of a more complex nature. These phenomena are related to nucleon-nucleon scattering in the nuclear medium during the first phases of the collision; for this reason they may represent a useful probe of the first step of nuclear collisions at intermediate energies [31, 32, 33]. In literature these phenomena are often termed as *hot-spot emissions, first-chance emissions* etc. The experimentally observed angular distributions of these particles are symmetric in the reference frame moving with half beam velocity. This fact suggested an equal participation of target

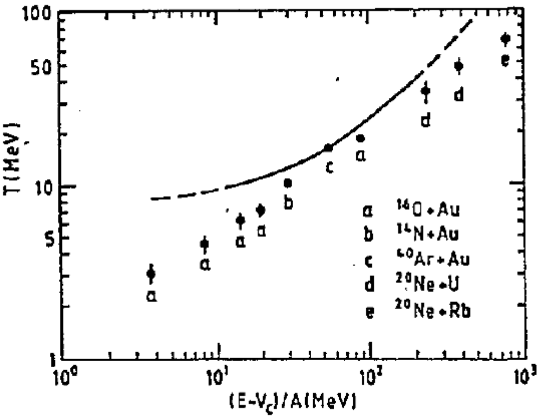

Fig. 1.10: Systematics of slope parameters extracted by means of Maxwellian fit of nucleon-nucleon emission, as a function of bombarding energy, for various systems. The solid line indicates prediction obtained by using a first chance model. From Fuchs and Mohring [34].

and projectile nucleons to direct emission due to nucleon-nucleon scatterings. In the following sections, the term ”pre-equilibrium” will refer to two-body nucleon-nucleon emissions.

In the literature, pre-equilibrium contributions have been often simulated by using a volume-emission Maxwellian source [31] moving with velocity $v \simeq \frac{1}{2}v_{beam}$. This parameterization is useful only to put some constraints in the phase space, in order to isolate the different contributions to light particles emission; it must be regarded always with some caution, because pre-equilibrium is a non-equilibrium phenomenon, while the presence of a Maxwellian distribution is linked to a thermalyzed and equilibrated system. Nevertheless, in the past years systematics on the slope parameter T extracted from the Maxwellian fit to pre-equilibrium emission has been collected, as it is shown in Figure 1.10 [34].

Different interpretations have been given to the slope parameter T for pre-equilibrium emission; they range from viewing T as a simple fit parameter to associating to it the meaning of a ”temperature of the *fireball* source” formed in the early stage of the collision between the two overlapping nuclei [35]. Probably T does not have a real thermodynamical meaning, but rather it could be interpreted by considering coupling effects between the Fermi motion of nucleons in nuclei and the projectile motion.

In Figure 1.11 we show the results of fits of proton kinetic energy spectra taken in coincidence with evaporation residues in incomplete fusion events for the reaction $^{36}Ar +^{98} Mo$ at 37 MeV/nucleon. The spectra have been fitted by considering three types of emission: the first one is due to the equilibrated quasi-fusion source; the second one is due to the weakly excited quasi-projectile and the third one takes into account nucleon-nucleon pre-

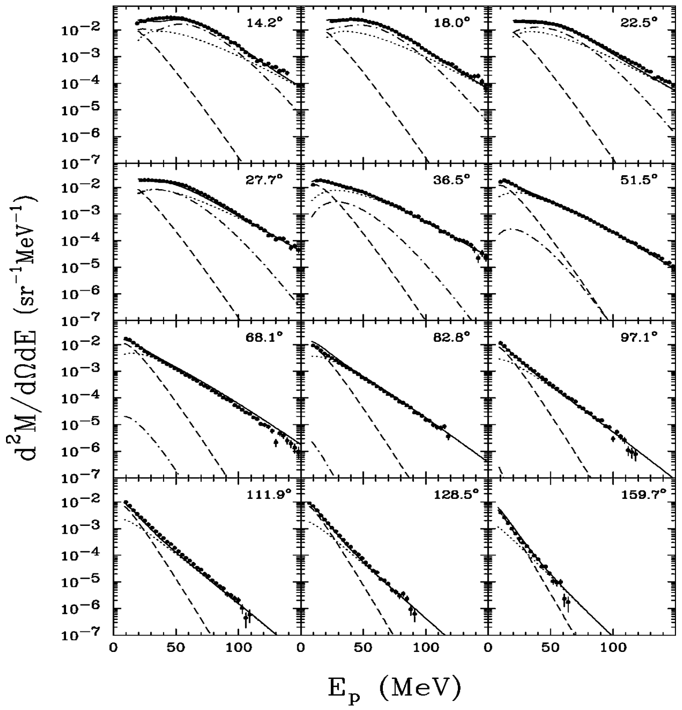

Fig. 1.11: Proton spectra emitted at various polar angles in $^{36}Ar + ^{98}Mo$ reactions at 37 MeV/nucleon, in coincidence with evaporation residues. Dots: experimental data obtained with the MEDEA array. Dashed line: Maxwellian moving source representing emission from the hot source populated in incomplete fusion. Dotted line: pre-equilibrium contribution. Dash-dotted line: emission from quasi-projectile source. Thick solid line: sum of all contributions. From ref. [36].

equilibrium contributions [36].

1.1.4 GDR γ rays emission

Analysis of γ ray emissions is complementary to the study of light charged particles in nuclear reactions at 10-20 MeV/nucleon. γs provide plenty of information about spectroscopy of the emitting system; they allow to extract data about spin, deformations and excitation energies of the system [37].

In nuclear reactions around 20 MeV/nucleon, γ rays spectra are mainly composed by four contributions [38, 39]; the first one, up to $E_\gamma = 2$ MeV, is due to γ rays emitted during the de-excitation phase of rotating nuclei along the yrast line; the second one, at $2 < E_\gamma < 8$ MeV, corresponds to statistical γ rays emitted by highly excited systems below particle emission threshold; the third one, with $10 < E_\gamma < 30$ MeV, is associated to giant dipole resonance γ rays emission; the fourth one, $E_\gamma > 35$ MeV, is due to

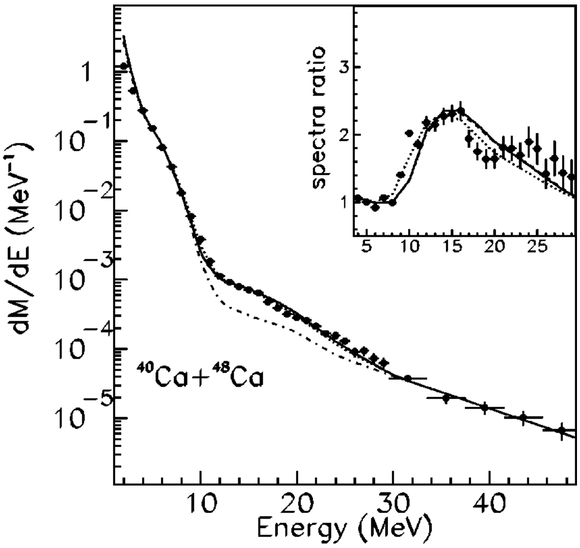

Fig. 1.12: γ rays spectrum taken in coincidence with fusion residues emitted in incomplete fusion events in $^{40}Ca +^{48} Ca$ reactions at 25 MeV/nucleon. Data have been obtained by means of the TRASMA-BaF$_2$ array [40]. The dash-dotted line is the result of a CASCADE [41] calculation assuming zero-strength for GDR emission (useful for the normalization shown in the insert). The solid line is obtained as a result of CASCADE calculations by assuming 15 MeV of GDR width and 260 MeV of GDR saturation energy. From ref. [42].

high energy γ rays belonging to brehmstrhalung emission in nucleon-nucleon collisions during the first phase of the reaction.

As an example, in Figure 1.12 we show the energy spectrum of γ rays emitted in the reaction $^{40}Ca +^{48} Ca$ at 25 MeV/nucleon [42]. This spectrum has been obtained by taking in coincidence γ rays with evaporation residues. Different contributions can be recognized.

In the context of this work, the most important contribution is represented by giant dipole emissions. It has been pointed out since a long time ago that compound nuclei formed in fusion (or incomplete fusion) reactions can evolve into a dipolar oscillation mode involving protons and neutrons (*giant dipole resonance*) [4, 43].

Two main parameters characterize GDR emissions: its *strenght* (yield compared to statistical γ rays) and its full width at half maximum (width). At very high excitation energies ($\approx$ 500 MeV) a simultaneous increase of width and the saturation of GDR strength have been reported [44]. This fact has been often considered as a signature of the existence of a *limiting* value of excitation energy beyond which nuclear systems cease to exist as bound systems [45]. From this point of view, the bombarding energy range near

20-30 MeV/nucleon constitutes a quite good benchmark for these effects; nuclear systems at multi-fragmentation threshold can be populated and the saturation of GDR strength could be a further clue of limits of nuclear matter existence.

1.2 Elements of Nuclear Thermometry and Calorimetry

The concept of temperature for macroscopic bodies is introduced by means of the zero-th principle of thermodynamics. Temperature is a measurable quantity; it is sufficient that the body is at thermal equilibrium with a given thermometer [46]. The kinetic theory of gases gives a more microscopic interpretation of temperature; the internal energy of gases and temperature are strongly linked. Finally, statistical mechanics described temperature starting from state functions as internal energy and entropy, by using Maxwell relations, as it follows [47]:

$$\frac{1}{T} = \frac{dS}{dE} \tag{1.2}$$

Among these three different contextualization of temperature, the proper one to be applied to the microscopical case of nuclei is the third. For the case of nuclei, as for other many-body systems, in fact, we may define entropy. A nuclear system can be in a given microstate (from ground-state to excited states) as a function of the different interplaying particle-hole or many-particles-many-holes configurations. The number of microstates falling into the energy interval ΔE is given by:

$$\Gamma = \rho(E, A) \cdot \Delta E \tag{1.3}$$

where $\rho(E, A)$ is the density level, a quantity commonly used in nuclear physics ($\rho = \frac{dN}{dE}$). Therefore, it is quite simple to evaluate the entropy of the system by means of the Boltzmann law:

$$S = ln\Gamma = ln\rho + ln\Delta E \tag{1.4}$$

and then we obtain: $\frac{1}{T} = \frac{d(ln\rho)}{dE}$. In this merely theoretical formulation it is evident the strong connection between temperature, level density and excitation energy of nuclear systems. The validity of Equation 1.2 to define a temperature in micro-canonical ensembles requires that the states involved in the calculation of $\rho(E, A)$ are equally populated [48]. This equilibrium condition is achieved only in compound nuclei at quite low excitation energy. By increasing the excitation energy, in fact, the time scales of evaporation of nucleons become similar to those required to achieve thermalization [49].

In the interacting Fermi-gas model, the relationship between excitation energy and temperature is $E^* = a \cdot T^2$ (an outline of demonstration can be found in [50]), where a is called density level parameter. Typical values of a range from A/8 to A/14. The density level parameter is influenced by different factors; for example it is linked to the total spin J reached by the compound nucleus. Moreover also the N/Z of the system seems to play an important role to explain subtle variations of the a parameter [51].

The thermodynamical characteristics of excited compound nuclei have been described since a long time ago by using the quantities discussed before (temperature, excitation energy, density level parameter) [52]. Moreover, in the last years, a strong analogy between the intermolecular potential energy characterizing ordinary liquids and the nucleon-nucleon interaction led to the search for the signals of a possible liquid-gas phase transition in nuclei, similar to that of liquids. There is a strong analogy between hot liquid drop that cools down by emitting molecules and light particles evaporation by an excited compound nucleus [53]. Overcoming a certain value of excitation energy, nuclei may undergo boiling-like phenomena, leading to the disintegration in clusters of bound nucleons (fragments, liquid phase) in co-existence with free nucleons (gas phase). This theoretically predicted phenomenon was called *nuclear liquid-gas phase transition*. Many possible experimental signature of this effects have been studied, until a correlation between T and E^* that seemed to confirm the attainment of phase-transition has been observed at GSI [3]. By increasing E^*, the temperature is observed to first increase following the formula $T \propto \sqrt{E^*}$. From $E^* \approx$3 MeV/nucleon to $E^* \approx$9 MeV/nucleon temperature stays almost constant (*plateau*). Overcoming $E^* \approx$9 MeV/nucleon, the temperature increases quite linearly, following a behavior typical of non interacting gases (free nucleon gas), see Figure 1.13.

After the pionieristic work of the ALADiN collaboration at GSI, other investigations have been done on liquid-gas phase transitions in nuclei. For example, the mass dependence of the starting point of the excitation energy plateau seen in caloric curves was studied [54]. Nowadays the study of the N/Z influence on this physical quantity is a subject of interest. From this point of view, nuclear thermometry is still today an exciting field of nuclear physics.

1.2.1 What is Nuclear Thermometry ?

Building a thermodynamical theory for excited nuclear systems is a difficult task. It presents some conceptual difficulties that we briefly discuss in this section. For example, nuclei are isolated systems; for this reason they can not exchange their excitation energy with the neighboring space. The quantum nature of nuclear systems imposes to replace classical statistical mechanics with quantum statistical theories. The presence of Coulomb forces between

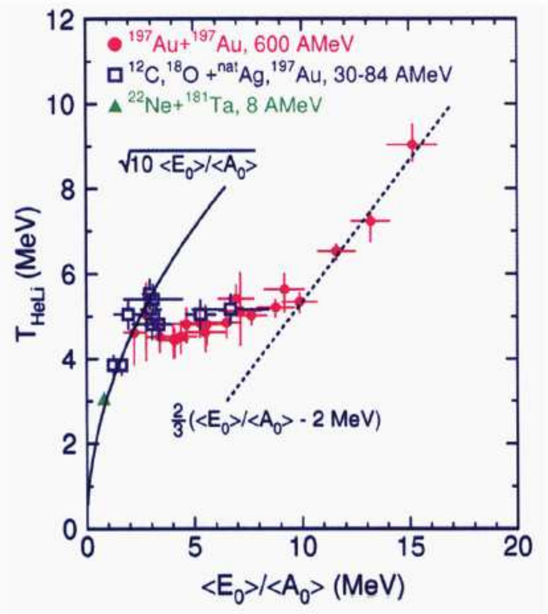

Fig. 1.13: Caloric curve obtained by ALADiN collaboration at GSI, Darmstadt. Temperature is obtained by using HeLi thermometer (see text). Excitation energy is extracted by means of calorimetry. Taken from ref. [3].

protons bound in nuclei can moreover introduce a further instability factor in hot nuclear systems. Finally we must take into account that, from an experimental point of view, secondary decays can distort thermodynamical quantities extracted with the methods shown in the following sections. These complications suggest that nuclear thermodynamics (especially for extremely excited systems) is a matter to be considered with caution.

Often, experimentally extracted values of temperatures reported in the literature are called *apparent temperatures*. This means that effects due to the de-excitation cascade and secondary decays can modify the measured value of temperature compared to their real values. In particular, the measured values are often the convolution of temperatures characterizing different steps of the de-excitation cascade. However, it has been shown recently [55] that apparent temperature can give quite robust signals of a liquid-gas phase transition in nuclei.

1.2.2 Limiting temperature

A fascinating subject in nuclear thermodynamics is represented by the limiting temperature and the maximum excitation energy sustainable by hot finite nuclei. This question was studied by physicists such as N. Bohr and H. Bethe. The liquid drop model parameterization, leading to the Weizsacker formula, suggested a mean binding energy of about 8 MeV/nucleon for stable nuclei; for this reason it was supposed that overcoming this value of excitation energy, a nuclear system would disaggregate in free neutrons and protons. With the development of modern heavy ion accelerators (seventies of 20-th century) experimental investigations on this topic became possible.

Nuclei can not be heated continuously. Beyond $T \approx 7MeV$, the time scales characteristic of particle evaporation become similar to those of expansion (followed by break-up) of nuclear system (around 150 fm/c, according to calculations of ref. [56]). Moreover, from a static point of view, the interplay between the Coulomb and the Surface term is strongly dependent on temperature. For this reason, overcoming a certain threshold of temperature (the *limiting temperature*, T_{lim}) surface tension become too weak to balance the repulsive Coulomb forces [57, 58]. This leads to the disintegration of nuclear systems in various parts, the disappearing of evaporation residues produced in incomplete fusion events and the suppression of collective motions characterizing excited quasi-compound nuclei (see Sect. 1.1.4). The existence of a limiting temperature has been often taken as a signature of liquid-gas phase transitions in nuclei.

The mass of the populated quasi-compound nuclei has a strong influence on T_{lim}; experimentally [54] it has been reported that light systems can reach values of T_{lim} higher than heavy system ones, for which the presence of many protons causes the lowering of T_{lim}.

More debated is the dependence of T_{lim} on the N/Z ratio of the nuclear system. In past times, some *liquid drop model* calculations showed a large correlation between T_{lim} and the N/Z of hot nuclei [59]. In Figure 1.14 we report results of these calculations.

From Figure 1.14 we can argue that, for a fixed value of Z, T_{lim} values are quite different as a function of the neutron number of excited system. To make some numerical examples, taken from ref. [60], calculations of ref. [59] predict $T_{lim} \simeq 8.2MeV$ for ^{124}Sn (having $N/Z = 1.48$), while for ^{124}La (having $N/Z \simeq 1.18$) T_{lim} is lower, being around $T_{lim} \simeq 6.3MeV$. More recent calculations performed with the SMM [61] code show, at variance, a more weak dependence of T_{lim} on N/Z; this hypothesis is borne out by a recent experiment performed at GSI [60]. T_{lim} values obtained for $^{124}La,^{124}Sn$ heated nuclei have been compared; differences of the order of some hundreds of keV have been seen.

In the following sections we will discuss briefly different ways to extract experimentally apparent temperatures of hot nuclear sources. In Chapt. 3 of this thesis these experimental methods will be used to carry out data analysis on studied reactions.

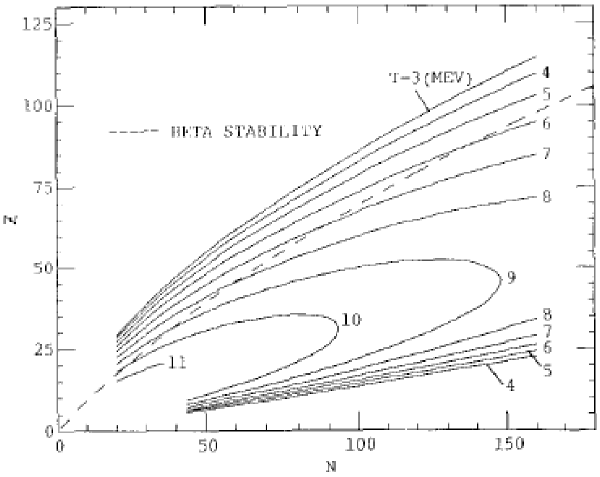

Fig. 1.14: Limiting temperatures of finite nuclei obtained by means of LDM model calculations. Limiting temperatures have been plotted as a function of neutron and proton numbers of studied nuclei [59]. Solid lines indicate equal limiting temperatures; the dashed line indicates roughly beta-stable nuclei.

1.2.3 Measuring temperatures: slopes of particle spectra

The first historical method to extract the temperature of excited nuclei was proposed by Weisskopf [52]; it consists of the analysis of kinetic energy spectra of light particles (typically neutrons, protons and αs) emitted in the de-excitation phase of a given, equilibrated, nuclear source. The de-excitation process is evaporative in nature; for this reason light particle spectra have a shape similar to Maxwell-Boltzmann distributions (obviously with kinematical corrections, because the source is often not at rest, see Sect. 1.1.2). During the sixties, the pre-exponential factor to be used in Maxwell-Boltzmann distribution was extensively debated. In some studies a factor $\propto \sqrt{E}$ (*volume-emission* Maxwellian) was used, in other ones a factor $\propto E$ (*surface-emission* Maxwellian) was adopted. Goldhaber discussed in details, in a famous *Rapid Communication* [62], the differences characterizing the two parameterizations, in light of the different energy ranges of the studied reactions. Today, a commonly accepted method of analysis consists of using different Maxwellian moving sources accounting for the different emitting sources. This is a good method to put constraint on the phase space and to extract values of apparent temperatures and emission multiplicities [31, 63]. In particular, surface or volume emissions are commonly used to reproduce the contribution due to equilibrated emitting sources, while in order to simulate pre-equilibrium emissions (or "*fireball*" emissions) a volume emission Maxwellian is generally adopted.

Moreover we underline that effects that are typical of nuclear dynamics, such as collective expansions, rotations etc (especially at bombarding energies above 40 MeV/nucleon) can lead to changes in spectral shapes of light particles. If these effects are not properly taken into account, the extracted values of temperature by means of moving source analyses can be slightly distorted compared to the real values [64].

1.2.4 Measuring temperatures: double isotope ratios

This method, widely used in the last two decades, can be applied to nuclear systems at thermal and chemical equilibrium; it is supposed in fact that an excited nucleus may exchange particles and energy with the environment, thus equilibrating thermally and chemically. This method consists of the measurement of ratios of isotopes differing by the same number of nucleons. For this reason the method is often called *double isotope ratios.* Isotope thermometers involve often ($^3He,^4He$) and ($^6Li,^7Li$) isotope ratios, due to the simplicity of detecting them. Indicating with $Y_{^6Li}$, $Y_{^7Li}$, $Y_{^3He}$, $Y_{^4He}$ the yields of the emitted isotopes, the apparent temperature of the emitted source may be estimated by using the following formula (see refs. [65, 66] and references therein):

$$T_{HeLi} = \frac{13.3}{ln(2.18 \cdot \frac{Y_{^6Li}/Y_{^7Li}}{Y_{^3He}/Y_{^4He}})} \tag{1.5}$$

where 13.3 is the difference of differences of binding energies of the double couples of isotopes, while 2.18 is a factor depending on masses and spins of involved isotopes. Obviously it is possible to consider many isotopic couples to perform nuclear thermometers based on double isotope ratio method [66].

Also these estimates of temperature will be affected by effects due to secondary decays. To solve this problem, phenomenological corrections have been introduced. One of these, discussed in ref. [67], is based on the introduction of a corrective factor $\frac{ln\kappa}{B}$ such that $\frac{1}{T_{app}} = \frac{1}{T} + \frac{ln\kappa}{B}$, where B is the difference of differences of binding energies of the two couples of isotopes and κ is a phenomenological correction parameter. In ref. [67] a wide range of κ correction parameters is reported, for a quite large variety of thermometers.

Moreover, it has been shown in [68] that the finite-size of analyzed hot nuclear sources may influence the estimate of T_{app} by using the standard formula 1.5 (even if the discrepancies are of the order of few hundreds of keV). In details, it was argued that T_{app} estimates based on various double isotope ratios thermometers for an identical hot source gave different results. In temperature measurements based on double isotope ratios methods, these two corrections must be taken into account to correctly estimate the emission temperature.

1.2.5 Measuring temperatures: population of excited states

This method has the same basic assumptions as the double isotope ratio method. The population distribution among the excited states of a system in statistical equilibrium depends on the temperature of the system and the energy level spacing. For a two-level system at constant volume the dependence is given simply by the Boltzmann factor [69]. Following this picture, the ratio of the populations of two states (if no particle decay takes place) is given by:

$$R = \frac{2j_u + 1}{2j_l + 1} \cdot e^{-\frac{\Delta E}{kT}} \tag{1.6}$$

Here, j_u and j_l represent the spins of the upper and lower state, respectively, and ΔE is the energy difference between these two states. This ΔE value limits the temperature that can be measured by this method, as for temperatures higher than ΔE one reaches saturation, i.e. the ratio R approaches its asymptotic high-temperature value [55].

A comparison between double isotope ratios and population of excited states temperatures obtained in Au+Au collisions from 50 to 200 MeV/nucleon has been performed in ref. [70]. At low bombarding energies the two thermometers give similar results, while at higher energies they disagree. This was explained by considering that the the two types of thermometers are sensitive to different stages of the fragment formation and emission [70].

1.2.6 Measuring excitation energies

An important part of calorimetric studies of hot nuclei is represented by the estimates of the excitation energy reached by nuclear sources produced in incomplete fusion reactions near 20 MeV/nucleon. These measurements are difficult to be performed due to both the limited detection efficiency of experimental devices (for example, often neutrons are not detected) and due to the simultaneous presence of various emitting sources [71]. From a theoretical point of view, if we are able to insulate a given equilibrated source that de-excites by means of light particles emission, the estimate of excitation energy may be obtained by summing up kinetic energies of the emitted particles (taking into account the Q-values of the considered decay channels). Obviously, the kinetic energies of the emitted particles must be considered in the frame of the emitting source [51]. In this calculation of ε^*, also γ rays emitted in the last phases of de-excitation chains should be included.

For the reasons mentioned above, it appears clearly that many difficulties arise from excitation energy estimates. All reaction products must be identified in charge and mass (in order to correctly evaluate the decay channel Q-value). In this context neutrons need to be detected too. Moreover, a multi-detector with 4π coverage is required. Building an ideal detector, satisfying the previously reported requirements, is an extremely difficult task. Many 4π detectors of good quality exist in the world (as Miniball, Indra, Chimera) [72]; however they are not able to isotopically identify *all* emitted particles and, moreover, it is extremely difficult to couple these devices with large area neutron detectors. When neutrons are undetected, the only way to estimate excitation energy consists to make some hypothesis on energies and multiplicities of neutrons by looking at proton emission. One of these consists in the assumption that for each proton emitted, N/Z neutrons are emitted with the same energy of protons (corrected for the Coulomb barrier) [73]. These hypotheses may be used only as a first approximation, due to the fact that pre-equilibrium emission may change the N/Z value of the emitting source compared to the total one.

Early attempts to perform calorimetric studies were done without 4π detectors. In order to estimate the excitation energies, methods different from calorimetry were used; for example, a widely used method was based on momentum conservation, assuming a quasi-binary behavior in incomplete fusion events [74, 75]. This approximation works well especially for reactions in direct kinematics ($A_{proi} \ll A_{targ}$). By imposing momentum conservation in incomplete fusion reactions, where only a part of projectile momentum is transferred to target (*partial momentum transfer* [74]), we can write: $\varepsilon^* \approx \sqrt{\varepsilon_R \cdot \varepsilon_P} - \varepsilon_R$, where ε^* is excitation energy (per nucleon) of the quasi-fusion source, ε_R is the recoil energy (per nucleon) of fused nuclei in the laboratory frame and ε_P is the kinetic energy (per nucleon) of the beam. Such formula gives an approximated measure of the excitation energy; for example Q-values are neglected, even if they play an important role in ε^* estimate especially at relatively low beam energies ($\approx$ 20 MeV/nucleon) [76]. This point may be enlightened by looking at Figure 1.15, where the various contributions to excitation energy estimate are disentangled; kinetic energies of neutrons, light charged particles (p,d,t,$^3He, \alpha$s) and light fragments, together with balance between Q-values and total particle kinetic energy are shown. The data have been obtained by ISiS collaboration [77]. Near 20 MeV/nucleon bombarding energy (roughly corresponding to $\varepsilon^* \approx 3-4$ MeV/nucleon) the contribution due to channel Q-value is not negligible.

Today, the availability of 4π detectors allows to perform good estimates of excitation energies reached by equilibrated sources, even with the right precautions discussed above. Some collaborations used simultaneously both methods (partial momentum transfer and calorimetry) to evaluate excitation energy of quasi-fusion sources; they performed a consistence cross-check between the obtained values, that were found similar one another within hundreds of keV [78].

We end this section by describing an interesting method, used in past times by the HMI-Berlin group, to determine maximum excitation energy reached by quasi-fusion sources in direct-kinematics collisions $^{32}S +^{58} Ni$ at

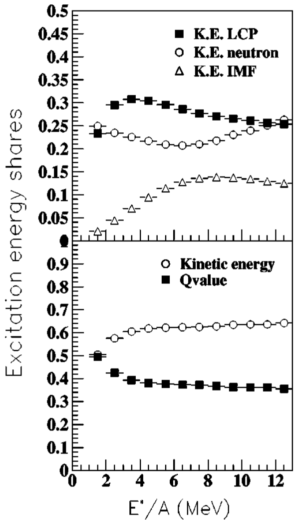

Fig. 1.15: (Upper panel) Excitation energy sharing between different particles emitted in the de-excitation cascade. Emission of protons, neutrons, deuterons, tritons and αs remove the largest part of excitation energy if $\varepsilon^* < 4MeV/nucleon$. At higher excitation energies, also fragments must be included in the calculation of excitation energy. (Lower panel) Balance between kinetic energy versus Q-value contributions in the determination of excitation energy by means of calorimetry. From [77].

25 MeV/nucleon [79]. Experimental apparatus was constituted by a time of flight arm set up at $\theta = 6°$ to measure mass and velocities of recoiling evaporation residues, followed by a sphere of silicon detectors (covering 88% of 4π sr) surrounding the self-supporting target. The sphere was used to detect light charged particles in coincidence with residues. Correlations between evaporation residue velocities (linkable to excitation energy by means of partial momentum transfer method, as discussed above) and light particle multiplicity show a saturation overcoming a given value of excitation energy (see Figure 1.16). Such saturation was associated to the existence of an excitation energy threshold (ε_{crit}) beyond which fusion-evaporation mechanisms would be replaced by fragmentation phenomena.

1.3 N/Z effects near multi-fragmentation threshold

In the last decades, experimental analysis on heavy ion physics in the range 20-100 MeV/nucleon bombarding energy focused especially on the influence that isospin asymmetry (or, analogously, N/Z ratio of nuclei involved in the collision) has on physical observables typical of these nuclear collisions [80]. For example, signals of the N/Z influence on pre-equilibrium GDR

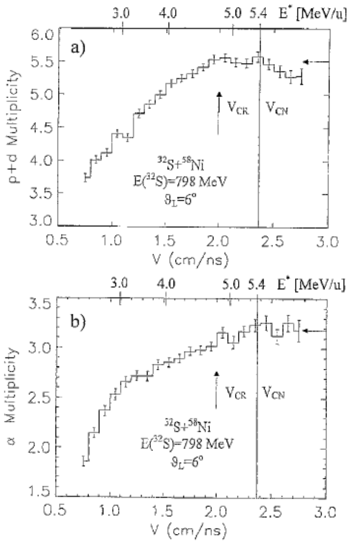

Fig. 1.16: Protons+deuterons and αs multiplicities as a function of recoil velocity of fusion residues emitted in $^{32}S+^{58}Ni$ reaction at 25 MeV/nucleon. Overcoming a certain value of recoil velocity (linkable to excitation energy of hot quasi-fusion sources), multiplicities saturate. Taken from [79].

emission have been searched for; at the same time, the N/Z dependence of neutrons to protons ratios emitted at pre-equilibrium in nuclear reactions at 100 MeV/nucleon was studied. The influence of N/Z on nuclear dynamics constitutes therefore a broad-based question, involving both communities of physicists working at low and high energies [81, 82]. In this chapter we will restrict ourselves to discuss mainly effects of the N/Z ratio on nuclear reactions near 20 MeV/nucleon.

If we draw a plot of the proton number Z vs neutron number N of known nuclei (both stable and radioactive), we obtain a bi-dimensional plot often called the Segrè chart (Figure 1.17). We realize that stable nuclei having masses lower than 40 units have mainly N=Z, while overcoming A=40, they have always $N > Z$. We can explain (in a simplified way) this fact by considering that the increased Coulomb repulsion (due to the high number of protons) must be balanced by an excess of neutrons [83].

Stable nuclei have many isotopes, that populate a quite large range in N/Z. Some remarkable examples are of course given by Calcium isotopes (going from ^{40}Ca, with N/Z=1.0, up to ^{48}Ca, with N/Z=1.4), Kripton (from ^{78}Kr, with $N/Z \simeq 1.17$, to ^{86}Kr, with $N/Z \simeq 1.39$) and Tin (from ^{112}Sn, with $N/Z = 1.24$, to ^{124}Sn, with $N/Z = 1.48$). By using this large variety of isotopes, we are able to perform nuclear reactions characterized by entrance channels differing strongly in N/Z ratios; it will allow to probe the influence of the neutron enrichment on reaction mechanisms and dynamics.

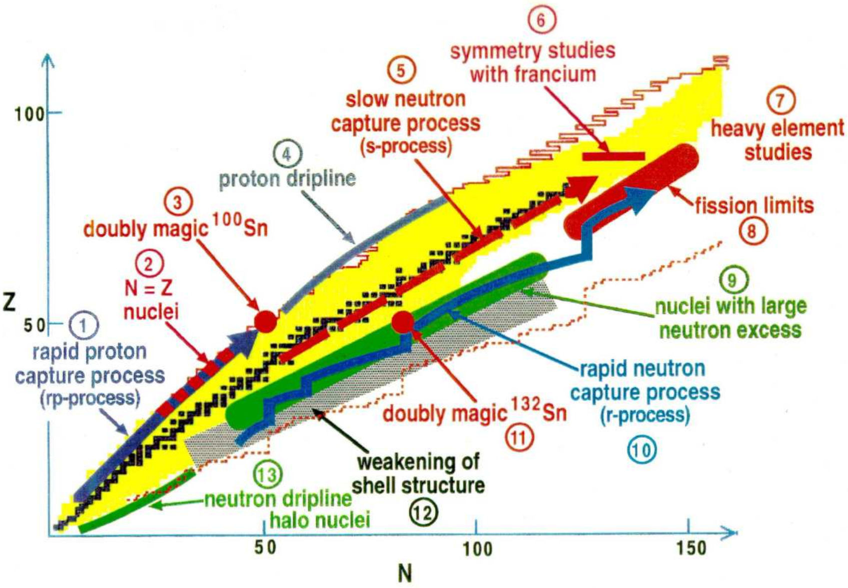

Fig. 1.17: Artistic view of nuclide chart. Stable, radioactive and theoretically predicted radioactive nuclei are shown. From ref. [84].

Moreover, the N/Z ratio (or the isospin asymmetry parameter $\frac{N-Z}{A}$) plays a fundamental role in the symmetry term of the nuclear equation of state [81]. This subject will be discussed in the following subsections.

In the next future the developments of new experimental techniques will allow to produce radioactive beams with high intensity. Several beams are important due to their N/Z ratio; just as an example, the neutron-rich nucleus ^{132}Sn has N=82 and Z=50 and it should be a doubly-magic nucleus with N/Z=1.64. The proton-rich side will also be interesting, as we will show in the next sections; an important case is given by ^{34}Ar, having N/Z=0.89. There is currently a large interest in the study of exotic nuclei very far from the stability valley, both to carry out spectroscopy studies (leading to significant deviations from ordinary shell models) and nuclear dynamics studies. A perspective involving incomplete fusion reactions induced by proton rich nuclei on ^{40}Ca will be discussed briefly in Chapter 2.

1.3.1 The isospin-dependent equation of state

At fragmentation threshold, i.e. near 30 MeV/nucleon bombarding energies, nuclear matter involved in a collision undergoes noticeable compression-expansion and heating phenomena that move it away from saturation point. A parameterization of energy profiles of nuclear matter as a function of density is called "equation of state" [56]. This equation contains a kinetic energy term, linked to Fermi motion of nucleons, and a potential term, accounting for nucleon-nucleon interactions (residual interaction). The last quantity is often parameterized by using Skyrme or Gogny forces. In general, the equation of state is parameterized as [56]: $\varepsilon = \frac{\hbar^2}{2m} \cdot \frac{3}{5}(\frac{3\pi^2}{2})^{2/3}\varrho^{5/3} + U(\varrho)$. This formula is valid only for symmetric nuclear matter at zero temperature. For non-zero temperatures, we must include a term proportional to T^2. It is more difficult to derive an equation of state for asymmetric matter, i.e. if $N/Z \neq 1$. In the kinetic term we must remove isospin degeneration for nucleon, and protons and neutrons densities must be considered separately. Typically, it is more convenient to express all the terms of the equation of state as a function of the total nucleon number. For this reason, in the kinetic term we isolate a term depending on $N + Z = A$, and another one depending on isospin asymmetry $\frac{N-Z}{A}$ that can be derived analytically and is called *kinetic term of symmetry energy*. Besides this term, we must take into account another very important correction term appearing in the asymmetric equation of state: the *potential term of symmetry energy* (often shortened as "symmetry potential"), $U_{sym}(\varrho)$ [81]. This term can be explained by considering that microscopic nucleon-nucleon interactions, n-n, n-p, p-p, are intrinsically different from one another. In mean field theories, the symmetry potential is often parameterized in three factors: $U_{sym}(\frac{\varrho}{\varrho_0}) = S_0 \cdot (\frac{\varrho}{\varrho_0})^\gamma \cdot (\frac{N-Z}{A})^2$ [82]. The S_0 factor is the strength of the symmetry potential, being around 18 MeV [81]. The $(\frac{\varrho}{\varrho_0})^\gamma$ term is the form factor of the symmetry potential; nowadays it is the subject of many research lines in heavy ion physics. Our knowledge of this term far from saturation densities is quite limited. Many physical observable have been suggested to be sensitive to the stiffness parameter γ [81].

Many models have been used to extract information about the density dependence of symmetry potential at medium energies. Two main families of models exists: mean-field approaches (such as IBUU [85] and BNV [86]), where nuclear dynamics is based on the solution of the Boltzmann transport equation, and molecular dynamics approaches (as QMD [19], CoMD [87], AMD [88]), where nuclear dynamics is simulated by solving the equation of motions of interacting nucleons (represented with gaussian wave-packets in phase space).

A recent theoretical development about symmetry potential was proposed in Ref. [89]. Within the context of a molecular dynamics model (CoMD-II) [90], investigators were able to derive microscopically symmetry potential simply starting from bare nucleon-nucleon interactions. As already mentioned before, $n-p$, $n-n$ and $p-p$ interactions are different. These quantities play a fundamental role in the determination of the symmetry potential. Molecular dynamics calculations allow moreover to study the influence of many-body correlations between nucleons, that seem to play an interesting role in the behavior of the symmetry potential [89].

Nowadays, there is a large interest to know details about form factor of the symmetry interaction, especially at quite high densities, because it is a fundamental quantity for all the models making theoretical predictions about the structure and stability of neutron stars [82]. However, description of these models is beyond the aim of the present work. Through the analysis of experimental data on $^{40}Ca+^{40,48}Ca,^{46}Ti$ collisions, we will derive, instead, physical information about the degree of stiffness of the symmetry potential (γ parameter) at near and below-saturation densities ($\approx$ 10% of variation compared to ϱ_0).

1.3.2 N/Z effects on light fragments production

The N/Z of the entrance channel plays an interesting role on a large variety of physical phenomena involved in nuclear reactions; they can be useful to determine the degree of stiffness of the symmetry potential. From low energy data it is moreover possible to extract information about relaxation times of the N/Z degree of freedom in binary-like collisions (*charge equilibration* in deep inelastic events [91]). In the following subsections we will discuss briefly some of these physical effects.

Isotopic effects

From the beginning of nineties, it was observed that by bombarding two targets having different N/Z values (for example ^{112}Sn and ^{124}Sn) with the same beam (for example ^{12}C at 80 MeV/nucleon), the emitted fragments had different isotopic yields, strongly related to the N/Z of the used target [92]. In particular, the larger was the neutron content of the target, the larger was the emission of neutron rich light fragments. Just to make an example, taken from ref. [92], isotopic ratio $^7Li/^6Li$ increased strongly when N/Z of entrance channels increased. A similar behavior was observed in the emission of Beryllium and other light isotopes. These phenomena were called *isotopic effects*, and constitute a good probe of the clusterization process involving light fragment produced in nuclear reactions at intermediate energies [80].

Sizeable isotopic effects were observed also in nuclear reactions at fragmentation threshold. For example, in Figure 1.18 we show isotopic ratios of helium, lithium, beryllium, boron nuclei emitted at 40° in $^{124}Sn,^{124}Xe+^{124}Sn,^{112}Sn$ reactions at 28 MeV/nucleon, as a function of N/Z ratios of the entrance channels. Isotopic effects are quite evident [93].

Neutron enrichment of mid-velocity emission: isospin drift

This effect is related to the gradient of nuclear density in the overlap region between interacting nuclei in semi-peripheral collisions; in particular, dynamical calculations suggest that the strong compression-expansion mechanism occurring in the overlap region during the first phase of the collision

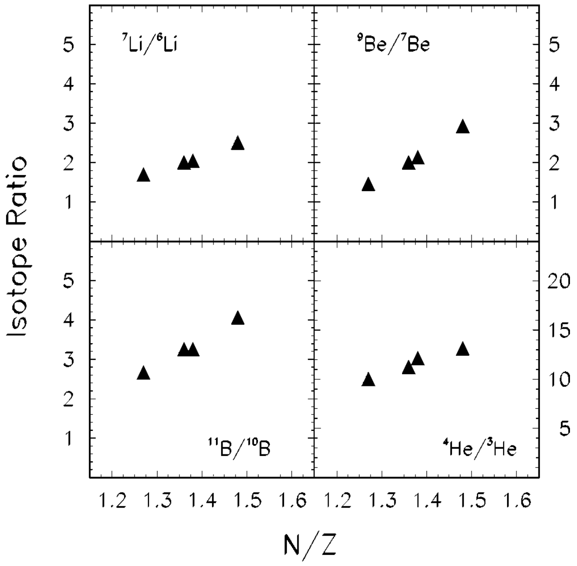

Fig. 1.18: Isotopic yield ratio of helium, lithium, beryllium and boron nuclei as a function of N/Z of the composite system for fragments emitted at a laboratory angle of $\theta = 40°$ in $^{124}Sn,^{124}Xe +^{124}Sn,^{112}Sn$ reactions at 28 MeV/nucleon. Isotopic effects are quite evident. From ref. [93].

may lead to a neutron migration from the projectile- and target-like fragments to the low density neck regions, inducing a neutron enrichment of light fragments emitted at mid-velocity [94]. This effect, called *isospin drift*, is noticeable in the case of intermediate energy collisions; in this case the density gradient is typically larger than 10% and the neutron enrichment of matter belonging to the mid-velocity (MV) region becomes clearly visible [95, 96]. It can be experimentally investigated by analyzing the isotopic composition of light fragments and free nucleons emitted by the mid-velocity region of phase space. As an example, we consider the collision between two identical heavy ions, $^{93}Nb +^{93}Nb$ at 38 MeV/nucleon. In Figure 1.19 [97], the average N/Z ratios characterizing hydrogen isotopes emitted by quasi-projectile and mid-velocity sources are compared. The two contributions (quasi-projectile and mid-velocity emissions) have been selected by means of appropriate constraints on parallel velocity.

In the absence of isospin drift phenomena, mid-velocity emission should be quite similar (neglecting effects due to the different ”temperatures” in these regions of the phase space) to quasi-projectile one. Instead, a clear enhancement of emission of neutron rich hydrogen isotopes (deuterons and tritons) is observed at mid-velocity. This observation, together with many other experimental findings, seems to support isospin drift in heavy ion collisions. A review article on this subject is ref. [94].

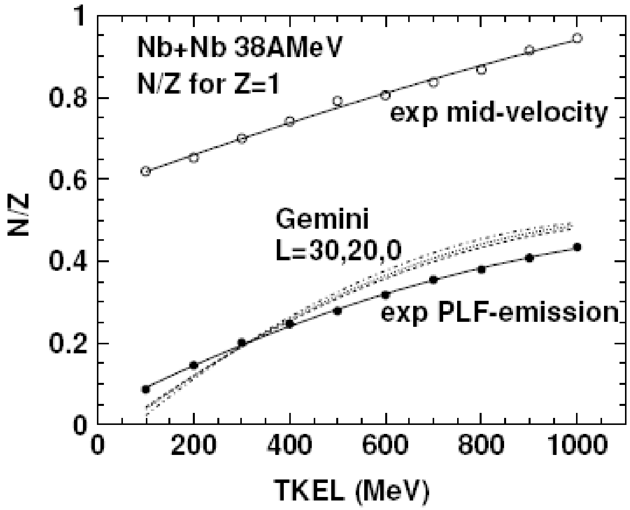

Fig. 1.19: Average N/Z ratio of hydrogen isotopes (p,d,t) emitted by $^{93}Nb + ^{93}Nb$ system at 38 MeV/nucleon. Full symbols indicate quasi-projectile emission, together with statistical de-excitation calculations performed with GEMINI code (dotted lines). Open symbols represent mid-velocity emission. N/Z is plotted as a function of TKEL, that can be linked to the centrality of collisions. From ref. [97].

Isospin diffusion

Few years after the discovering of deep inelastic collisions, the first studies about the phenomenon of N/Z relaxation were carried out in these collisions (1975, [91]). In the energy regime typical of deep inelastic collisions (bombarding energies ranging between 5 and 10 MeV/nucleon), the interaction times between projectile and target constituting the rotating di-nuclear system are quite large. If two nuclei having different N/Z ratios react, the interaction time is quite long to allow a re-arrangement of N/Z in the whole di-nuclear system. This phenomenon was named *charge equilibration.* It is clearly linked to the N/Z gradient of interacting projectile and target nuclei, and was observed in ref. [91] for the first time.

By increasing the bombarding energies, the emission of two main fragments in semi-peripheral reactions is more and more collinear and interaction times are strongly reduced. For this reason, the N/Z degree of freedom could not have time to re-arrange in order to lead to uniform charge distribution in the di-nucleus. Experimental data of semi-peripheral collisions $^{112,124}Sn + ^{112,124}Sn$ at 50 MeV/nucleon have been interpreted as due to a net neutron diffusion from the neutron-rich partner to the neutron poor one [98]. Moreover, at ≈ 30 MeV/nucleon bombarding energy and above, pre-equilibrium emitted nucleons can lead to changes in the N/Z of the in-

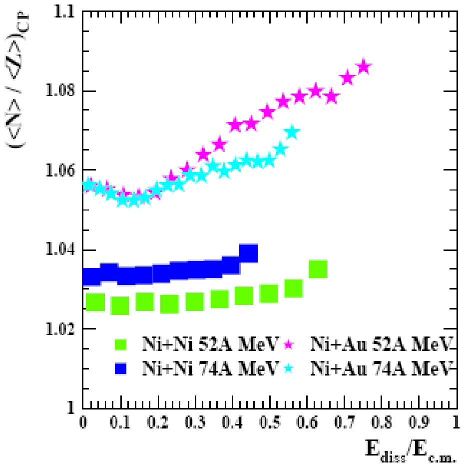

Fig. 1.20: $< N/Z >$ ratio of quasi-projectile source extracted from isotopic composition of light fragments (d,t,He,Li,Be nuclei) emitted in $^{58}Ni + ^{58}Ni$ and $^{58}Ni + ^{197}Au$ reactions at 52 and 74 MeV/nucleon. $< N/Z >$ is plotted as a function of dissipated energy (that can be linked with centrality of collisions). From ref. [99].

termediate system.

In Figure 1.20 we report the reconstructed N/Z ratios of quasi-projectile sources (evaluated experimentally by looking at N/Z of light fragments emitted by these sources) in reactions $^{58}Ni + ^{58}Ni$ and $^{58}Ni + ^{197}Au$ at 52 and 74 MeV/nucleon [99]. Data are plotted as a function of the dissipated energy, a quantity linkable to the impact parameter of the collision and to the interaction time between quasi-projectile and quasi-target nuclei. It is quite evident at both bombarding energies that the $\langle N/Z \rangle$ of the quasi-projectile is strongly affected by the N/Z of the quasi-target used. This is a clear signal of isospin diffusion phenomena in reactions involving projectile and target nuclei with different N/Z ratios ($^{58}Ni, N/Z \simeq 1.07$ versus $^{197}Au, N/Z \simeq 1.49$).

When nuclei having different N/Z values collide, isospin drift and isospin diffusion phenomena affect simultaneously mid-velocity emission. This point makes it difficult to separate the individual contribution of these two phenomena to the neutron richness of the emitted fragments. A simple but strong probe to analyze isospin drift effects without contaminations due to isospin diffusion components is obtained by colliding two nuclei having identical N/Z values (as already shown in Figure 1.19 or as the case of $^{40}Ca + ^{40}Ca$ reaction, discussed in Chapt. 3) at intermediate energies. In this special case, the isospin diffusion phenomenon is absent, and the possible neutron enrichment of light fragments emitted at mid-velocity can be attributed purely to isospin drift effects [100].

At the end of this subsection, we underline that, up to now, there is a large lack of experimental data on isospin diffusion and charge equilibrium themes in nuclear reactions at bombarding energies from 5 to 30 MeV/nucleon. This is often due to unfavorable experimental thresholds to identify both in charge and mass low energy emitted fragments. However, this energy domain is of great interest because it is the best suited to determine with accuracy the relaxation times typical of N/Z degree of freedom in semi-peripheral nuclear reactions. The availability of intense and N/Z-asymmetric beams at the SPIRAL2 facility [101] will provide unique tools to shed light on these phenomena.

1.3.3 N/Z effects on reaction dynamics

Since a long time, theoretical calculations performed by using transport models (LV and VUU, for instance) showed that the N/Z degree of freedom of the entrance channel can affect collision dynamics at low and intermediate energies [102]. Several calculations involving calcium isotopes have been performed involving both stable calcium beams $^{40,48}Ca$ and quite exotic calcium systems such as ^{56}Ca [102]. Calculations showed that cross sections of different reaction paths (such as fusion, binary-like, etc) can be influenced by the neutron richness of the interacting nuclei. Pre-equilibrium emission also seems to be sensitive to the N/Z of the total system. Therefore, beyond fragments emission, collision dynamics is also sensitive to neutron-richness and can provide useful information about the stiffness of the symmetry potential, as it is shown in ref. [103].

Recently, the Chimera collaboration pointed out that in semi-peripheral reactions $^{112,124}Sn+^{58,64}Ni$ at 35 MeV/nucleon the ratio between the yields of fission fragments emitted in statistical and dynamical fission of projectile-like sources is strongly linked to the N/Z of the entrance channel. In particular, the larger is neutron richness, the larger is dynamical emission of fission fragments [104].

In Chapters 3 and 4 I will present data of nuclear reactions involving medium mass nuclei (calcium isotopes, mainly) at 25 MeV/nucleon. I will show that the N/Z of the entrance channel plays a fundamental role in the emission of evaporation residues in incomplete fusion events.

1.3.4 Symmetry potential at low densities: present status

All isospin effects discussed in the previous sections can give useful information about the degree of stiffness of symmetry potential at low densities. Taking inspiration from ref. [105], in Figure 1.21 we show different values of the γ parameter (see Sect. 1.3.1) obtained recently from the comparisons of experimental data (isospin diffusion, pre-equilibrium neutron/proton ratio, iso-scaling and binary-evaporation residue competition) and theoretical

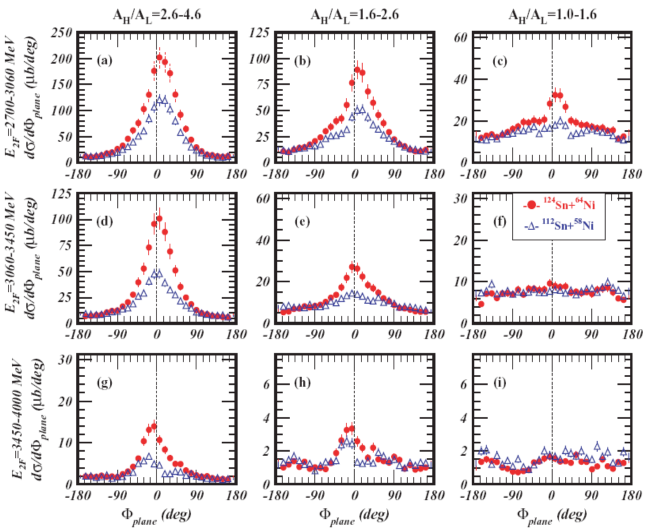

Fig. 1.21: Φ_{plane} distributions of projectile fission fragments emitted in the two reactions $^{112,124}Sn + ^{58,64}Ni$ at 35 MeV/nucleon. An extra-yield of events centered at $\Phi_{plane} \simeq 0$ is seen for the neutron-rich system. They are due mainly to dynamical fission of quasi-projectile nucleus. See ref. [104].

calculations performed with different models. The blue star point is the result of the comparison of experimental data discussed in this thesis with CoMD-II model calculations (see Chapter 3 and 4). As it is seen in Figure 1.22, a solid estimate of the stiffness parameter is not yet achieved nowadays. For this reason, many experimental campaigns have been planned to deeper understand the behavior of the asymmetry term of the nuclear equation of state.

1.4 Conclusions

From the phenomenology discussed in the previous paragraphs, we realize that heavy ion collisions in the bombarding energy range 20−30 MeV/nucleon involving medium mass nuclei constitute an interesting benchmark to study nuclear dynamics and nuclear thermodynamics of excited sources populated in incomplete fusion events. While effects due to mass asymmetry of the entrance channels have been disentangled in past years, only few data on *isospin* effects were reported in literature. It is interesting to underline that information about the degree of stiffness of the symmetry potential can be moreover derived from the analysis of the competition between different reaction channels characterizing this type of semi-central reactions. Semi-peripheral reactions can be also useful in order to understand isospin related phenomena. Signals of isospin diffusion and drift can be derived by analyz-

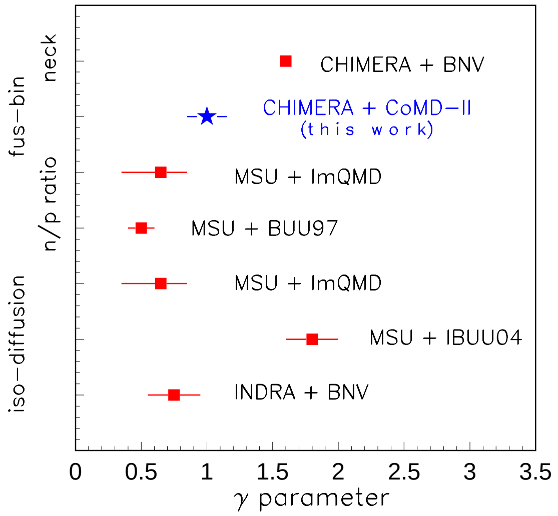

Fig. 1.22: Systematics of evaluated stiffness parameter γ extracted by means of comparisons between experimental data and theoretical calculations. Re-arranged from ref. [105]. The blue star point has been obtained from the data analysis discussed in Chapters 3 and 4 of this thesis.

ing isotopic emission for quasi-projectile and mid-velocity sources. For these reasons we performed the *limiting* and *isospin-1* experiments: $^{40}Ca+^{40}Ca$, $^{40}Ca+^{46}Ti$, $^{40}Ca+^{48}Ca$ and $^{48}Ca+^{48}Ca$ at 25 MeV/nucleon. These reactions have large variation in the N/Z of the total systems, ranging from N/Z=1 up to N/Z=1.4. In Chapters 3 and 4 we will study isospin effects on different physical observables characterizing these reactions.

Chapter 2

Overview of the Chimera detector

In order to perform high quality studies of heavy ion collisions at intermediate energies, two devices must exist in a research laboratory:

- An ion accelerator, capable of delivering beams at medium energies with good quality;
- An highly performing detector, in order to detect almost all the particles emitted in each reaction event. Moreover, it should be capable of identifying charge and mass of the detected nuclei and measuring their energy with good resolution.

At INFN - Laboratori Nazionali del Sud, Catania, Italy, we have the opportunity to use a Superconducting Cyclotron that can accelerate heavy ions up to 80 MeV/nucleon.

Due to the large multiplicity of particles emitted in the exit channels of nuclear reactions at 20-30 MeV/nucleon, it is necessary to use detection devices covering the largest solid angle with good granularity. This would reduce the chance of having multiple hits in a single detector. For such reason, in the '90, a large collaboration involving Italian and foreign scientist started the construction of the Chimera (**C**harged **H**eavy **I**on **M**ass and **E**nergy **R**esolving **A**rray) detector to be installed at the INFN-LNS. We first report the main features that characterize this device:

1. Very high angular coverage (94% of 4π sr);
2. Many identification techniques simultaneously used to identify in mass and charge the emitted nuclei;
3. Low detection thresholds;
4. High granularity achieved with a large number of telescopes (1192).

Originally, the collaboration focused on the construction of a cylindrical configuration for the new multi-detector, centered around the beam axis. In order to recover energy and to identify in mass and charge the emitted particles, $\Delta E - E$ techniques were used. A silicon detector was coupled to a CsI(Tl) crystal read by photodiode. Details about characteristics of these detectors will be described in the following sections [106, 107, 108, 109].

2.1 Detector geometry

The Chimera array is constituted by 1192 $\Delta E - E$ telescopes, grouped into two main sub-systems:

- the forward sub-system, constituted by an array of 688 telescopes, is shaped as a cone. It has a large granularity, allowing a good disentangling of particles emitted at forward angles. Due to the kinematics of collisions with fixed target, the most important part of the emitted particles is focused in forward direction. This part of the Chimera array is mechanically independent; it is constituted by nine self-supporting independent rings, covering a polar angle range of $1^\circ \leq \theta \leq 30^\circ$ (see Table 2.1 for details) and 360° azimuthal angles. The granularity changes with increasing polar angles: the first ring is composed of 32 telescopes, the ninth by 96 detectors. All the rings are put on platforms allowing their independent displacement. From 0° to 1° there is an hole to let the beam pass through.

- the backward sub-system, constituted by 504 telescopes, is a sphere having a radius of 40 cm, centered around the target. It covers polar angles ranging from 30° to 176°. These 504 modules are arranged in 17 rings.

On Table 2.1 we report the general characteristics of the detector, being θ and ϕ the polar and the azimuthal angle respectively.

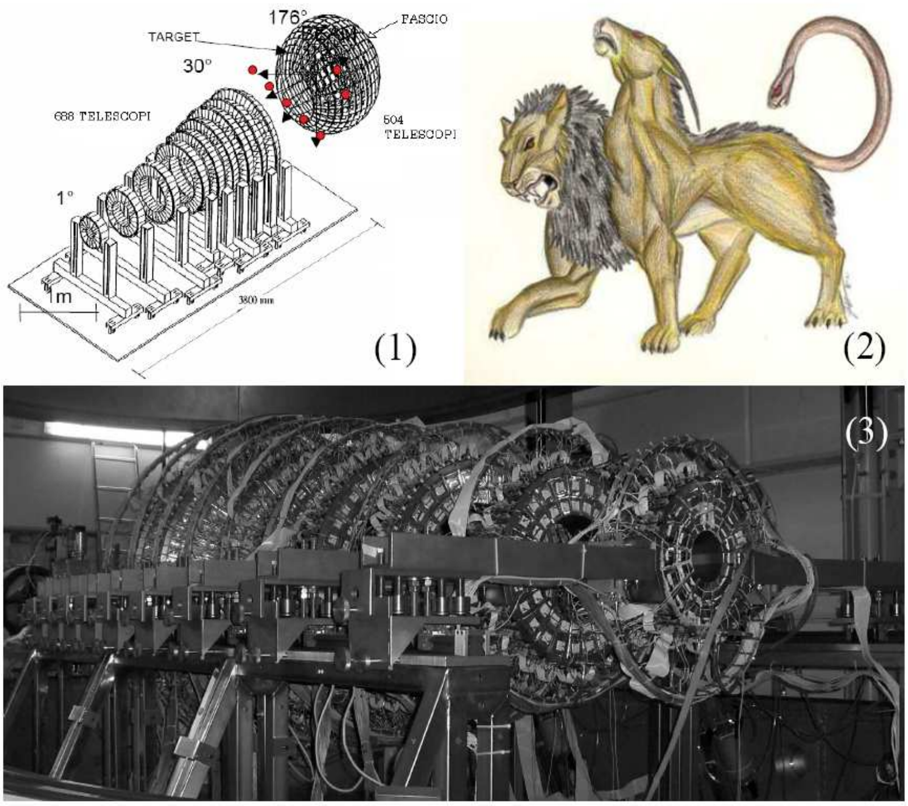

Fig. 2.1: (1) Scheme of the Chimera array. The Rings and the Sphere are shown. (2) A Greek Chimera, as it was drawn by the artist Tina Ponzoni (available on the web). According to Greek mythology, the monster was a fire-breathing female creature of Lycia in Asia Minor, composed of the parts of multiple animals: upon the body of a lioness with a tail that ended in a snake's head, the head of a goat arose on her back at the center of her spine. The Chimera was finally defeated by Bellerophon, with the help of Pegasus. Since Pegasus could fly, Bellerophon shot the Chimera from the air, safe from her heads and breath. A different version reports that he finished her off by equipping his spear with a lump of lead that melted when exposed to the Chimera's fiery breath and consequently killed her (from Wikipedia). (3) Chimera multi-detector, after the transfer to the new Chimera scattering room at INFN - LNS (September 2008). Photo by Domenico Santonocito.

Ruote	Anelli	Dist. (cm)	θ_{min}	θ_{max}	Num. riv.	$\Delta\phi$	Area	$\Delta\Omega$ (msr)
1	1	350	1	1.8	16	22.5	16.3	0.13
	2		1.8	2.6	16	22.5	25.6	0.21
2	3	300	2.6	3.6	24	15	22.2	0.25
	4		3.6	4.6	24	15	29.3	0.33
3	5	250	4.6	5.8	32	11.25	23.3	0.37
	6		5.8	7	32	11.25	28.6	0.46
4	7	210	7	8.5	40	9	24.2	0.55
	8		8.5	10	40	9	29.1	0.66
5	9	180	10	11.5	40	9	24.8	0.77
	10		11.5	13	40	9	28.2	0.87
6	11	160	13	14.5	48	7.5	20.8	0.81
	12		14.5	16	48	7.5	23.1	0.9
7	13	140	16	18	48	7.5	26.2	1.34
	14		18	20	48	7.5	29.1	1.49
8	15	120	20	22	48	7.5	23.6	1.64
	16		22	24	48	7.5	25.7	1.78
9	17	100	24	27	48	7.5	29.5	2.95
	18		27	30	48	7.5	32.7	3.27
10	19	40	30	38	32	11.25	24.5	15.33
11	20	40	38	46	32	11.25	29.3	18.34
12	21	40	46	54	32	11.25	33.6	21
13	22	40	54	62	32	11.25	37.2	23.25
14	23	40	62	70	32	11.25	40.1	25.05
15	24	40	70	78	32	11.25	42.2	26.35
16	25	40	78	86	32	11.25	43.4	27.15
17	26	40	86	94	32	11.25	43.9	27.42
18	27	40	94	102	32	11.25	43.4	27.15
19	28	40	102	110	32	11.25	42.2	26.35
20	29	40	110	118	32	11.25	40.1	25.05
21	30	40	118	126	32	11.25	37.2	23.25
22	31	40	126	134	32	11.25	33.6	21
23	32	40	134	142	32	11.25	29.3	18.34
24	33	40	142	150	32	11.25	24.5	15.33
25	34	40	150	163	16	22.5	56.7	35.45
26	35	40	163	176	8	45	50.9	31.79

Table 2.1: Geometrical characteristics of the Chimera array. See also Refs. [106, 107].

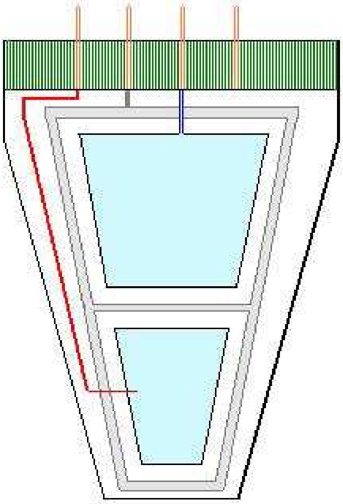

Fig. 2.2: Not in scale scheme of a silicon detector belonging to the rings of the Chimera array. Green: fiberglass support. Azure-blue: detector active areas. Grey: guard ring. Red and Blue: electrical contacts.

The telescopes include some limited dead regions, due to the presence of target rods, metallic supports and so on, thus reducing the geometrical efficiency of the device to about 94% of the whole solid angle.

To reach the high vacuum necessary to the good functioning of the detectors (10^{-6} millibar) root, turbo-molecular and cryogenic pumps are used. Moreover, silicon detectors and pre-amplifiers are cooled by means of a forced circulation of a refrigerant fluid. For further technical details, see ref. [110].

2.2 Silicon detectors

Even if their discovery was relatively recent ('70s), silicon detectors are widely used in nuclear physics due to their relatively low cost and their good energy resolution [111]. Moreover, they are easy to use and to handle both as stopping and transmission detectors. The rise time of typical signals is quite short ($10 - 100$ ns); for this reason they can also be used in time of flight measurements to provide the stop signal. Finally, the response function of silicon detectors is quite linear and independent (apart from small effects due to pulse-height defect) on the mass of the detected ions.

The silicon detectors of Chimera array are produced with passivated planar technology by the MICRON Semiconductor and EURYSIS companies. This option represented, at the time of the development of the Chimera project, one of the best available technologic solutions [112].

The fabrication process starts by constructing a wafer of ultra-pure Si that is n-doped by means of donors. The surface of the wafer is then passivated by creating a thin layer of SiO_2. Subsequently, some regions of passivation are removed to create windows for the incoming particles. A $p-n$ junction is then created by converting a thin layer of silicon (under the entrance windows) from type n to type p by means of a boron ionic implantation. The so-formed p-doped zone is often called *rectifying contact*. To improve the depletion of the junction, a thin layer of As atoms is placed in the rear part of the detector. This region of the detectors is often called *blocking contact*. Radiation damage is prevented by using an annealing technique. It consists of heating the proto-detector at $600°C$ for 30 minutes. The construction process ends by evaporating aluminium on both faces of the detector, in order to guarantee the right electrical contacts. Finally the detectors are separated and framed in fiberglass grooves. Bonding wires assure the electric contacts from the bias pin to the detector.

The nominal thickness of the Chimera Si detectors was about $300\mu m$; they have trapezoidal shapes, as shown in Figure 2.2. The observed rise times are quite short ($10-50$ ns for light ions; for highly charged ions, rise time can overcome 150 ns due to *plasma delay* effect) [106, 107].

To optimize the depletion of the silicon junction, the detectors are over-biased by applying an extra-bias of 30% above the nominal one. Another important tool to achieve good time resolution in time of flight measurements consist in mounting silicon detectors from the rectifying contact (p-n junction); in this way, electron-hole couples generated by the ionization induced by the heaviest ions (typically stopped in the first few microns of the detector) experience a quite high electric field, and this allows a better charge collection and time response.

Silicon detectors belonging to the most forward part of the Chimera array are constituted by a trapezoidal common slice where two active pads have been gained; in this way we optimized the dead zones due to the presence of another fiberglass support. The blocking contact is taken at ground in both pads constituting the slice; the rectifying contacts are instead biased at the same negative potential supplied by charge preamplifiers. The guard rings are also biased by pre-amplifiers, by means of resistors [112].

The silicon detectors of the sphere are single pad detectors. In this case a huge optimization work was done to minimize dead zones due to the fiberglass supports and to kapton flats used to contact detectors and preamplifiers.

2.3 Scintillation detectors CsI(Tl)

The second detection unit characterizing the Chimera $\Delta E - E$ telescopes is constituted by a CsI(Tl) scintillator optically coupled to an HAMAMATSU photodiode ($324mm^2$ surface) [113]. The use of CsI(Tl) has the following advantages in residual energy measurements:

1. Quite high density ($4.51 gr/cm^3$), leading to a large stopping power. This allows to stop high energy particles in a relatively low thickness;
2. Quite low manufacturing costs;
3. Good light emission yield ($\approx 10^4$ photons/MeV), peaked at $\lambda \simeq 550$ nm;
4. Stability of the response, due to the use of photodiodes;
5. Mass and charge identification of light particles by means of fast-slow correlation analysis.

Beyond the advantages above mentioned, some limitations exist: for example, photodiodes have signal to noise ratios not so good as photomultipliers. Moreover, the light response of scintillators (that will be converted in electric signal by the photodiodes) is not linearly related to the energy of particles. In particular, by defining as $\frac{dL}{dx}$ the specific light response of scintillator, this quantity is strongly related to the stopping power of the particle $\frac{dE}{dx}$ through the Birks formula [111]:

$$\frac{dL}{dx} = \frac{A \cdot \frac{dE}{dx}}{1 + B \cdot \frac{dE}{dx} + C \cdot (\frac{dE}{dx})^2} \tag{2.1}$$

From this formula it follows that we will have an almost linear response function only in cases of small stopping power $\frac{dE}{dx}$, i.e. for light particles (such as p,d,t,α) at quite high energy.

CsI(Tl) light output is composed by the overlap of two contributions with a fast ($\tau_1 \approx 500 ns$) and a slow ($\tau_2 \approx 3.2 \mu s$) decay times [111]:

$$L(t) = A_1 \cdot e^{-\frac{t}{\tau_1}} + A_2 \cdot e^{-\frac{t}{\tau_2}} \tag{2.2}$$

The relative weight of fast and slow emission yields, A_1 and A_2, is strongly related to the different charge and mass of incoming particles [111, 113]. For this reason, identification of high energy light nuclei is possible by performing a correlation between fast and slow signal extracted from CsI(Tl) detectors. An example of fast-slow correlation obtained in the *limiting* experiment is show in Figure 2.9.

The thickness of CsI(Tl) crystals varies as a function of polar angles: in particular, at forward angles they are 12 cm thick, while at the most backward angles they are 3 cm thick.

2.4 Electronic chains for Si and CsI(Tl) detectors

To minimize electronic noises, Silicon and photodiode preamplifiers have been assembled into *motherboards* and put in the vacuum chamber, close to the detectors. Heat dissipation is favored by metallic contact with cooled supports. The bias supply of detectors and preamplifiers are placed outside the vacuum chamber, together with other racks of processing electronics.

From the signal delivered by silicon detectors we extract:

- The energy deposited by detected particles;
- A logic signal that is used as a start for time of flight measurements;
- The rise time of the signal.

With the recent implementation of a *pulse-shape* analysis of silicon signals, we are able to extract information about the rise time of signal, that can be very useful to identify in charge those slow nuclei stopped in silicon detectors. In details, silicon signals are slightly shaped, and then processed by two discriminators. They will send logic signals when the shaped signal overcomes respectively the 30% and 80% of total rise time. These two logic signals, together with energy signal, are obtained by using a CAEN *16ch Spectroscopy Amplifier NIM1568B.* The two logic signals are then sent to two TDCs, that will transform into digital information time differences with respect to the radio-frequency (RF) signal used as a common stop: $\Delta T = T_{RF} - T_{30\%}$ and $\Delta T = T_{RF} - T_{80\%}$. The on-line subtraction of these two quantities provides the "rise time" (80%-30%) of the shaped signal: $T_{rise} = T_{80\%} - T_{30\%}$. Energy signals are digitized by means of VME QDCs.

The gate generation for QDCs and TDCs is performed by a common trigger signal, based on the multiplicity of each reaction event. A summary scheme of electronic chain following silicon detectors is shown in Figures 2.3 and 2.4.

The main feature of the CsI(Tl) electronic chain, shown in Figure 2.6, is characterized by the processing of the fast and slow components of the signal. Signals are processed by SILENA amplifiers with shaping time $2\mu s$. Signals are then stretched, leading to the presence of a level (of the same amplitude of the peak) lasting for $\approx 5\mu s$. At the same time, a magnified copy (×10) of the amplified signal is generated. Stretched and magnified signals, linked to fast and slow light emission, are sent to two different QDC to be digitized and acquired. We send two synchronous gates to the two QDCs.

The used gate signals start a few μs later than the time of peak. Thus, the QDC outputs will correspond to the charge of the stretched fast signals and to the charge integral of the tail of the signal (mainly dominated by the slow component). The correlation between these two quantities allows one to identify in charge and mass light charged particles (mainly hydrogen and helium isotopes).

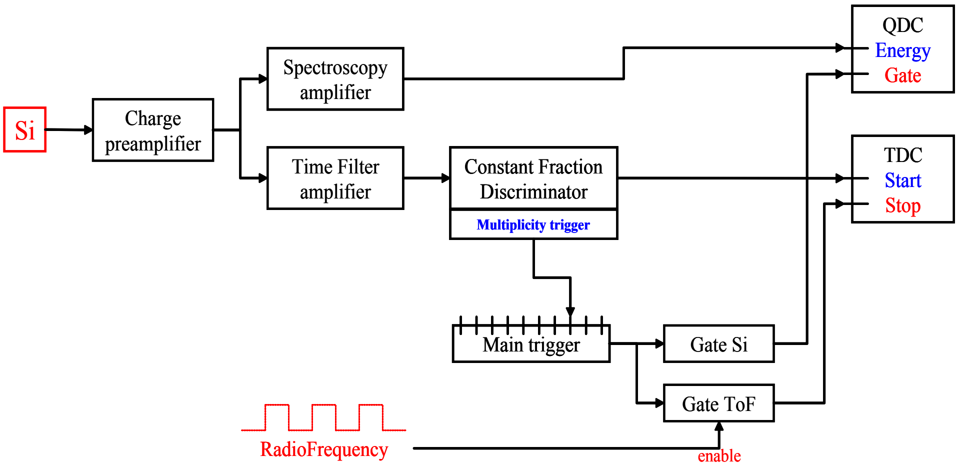

Fig. 2.3: Scheme of the electronic chain following silicon detectors in rings 1-3 and 14-26. For these detectors, during the Exochim campaign, pulse-shape techniques for silicon detectors are not used. Amplifiers and CFDs are CAMAC based and manufactured by CAEN. A similar scheme was used in all the previous campaigns with the Chimera array.

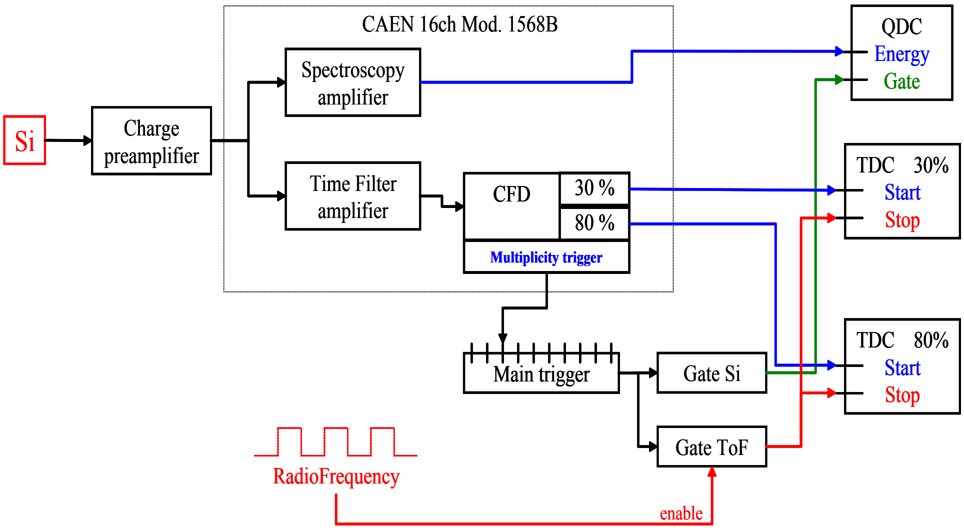

Fig. 2.4: Scheme of the electronic chain following silicon detectors in rings 4-13. For these detectors we extracted also rise-time information. The main component of chain is constituted by a multipurpose CAEN module NIM1568B. It provides an amplified and stretched energy signal, a multiplicity signal (useful to perform electronic trigger, with a step level of 25 mV/hit) and two logic signals corresponding to the instants when the signal overcomes 30% and 80% of its peak value.

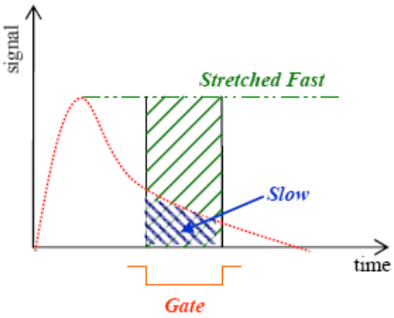

Fig. 2.5: Scheme of treatment of CsI(Tl) signals. The fast and slow components have been extracted by means of a single gate method.

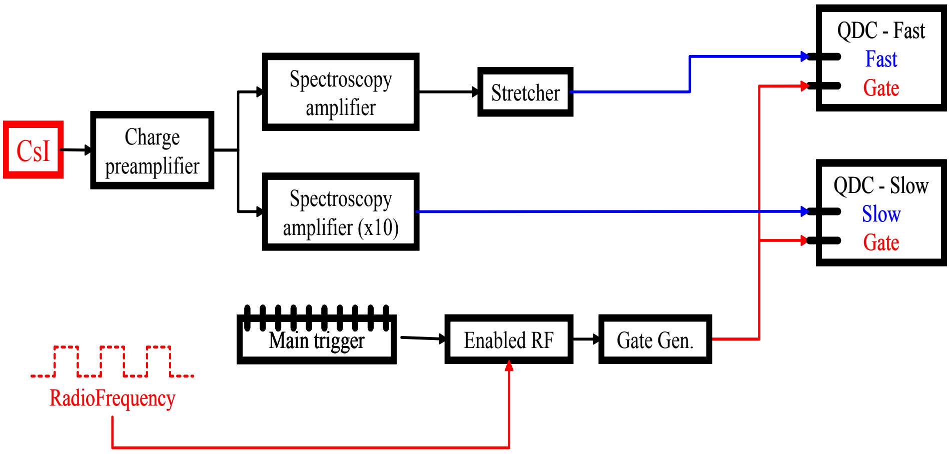

Fig. 2.6: Sketch of the electronic chain treating CsI(Tl) signals. The used amplifiers have NIM standard, and are manufactured by SILENA; they manage 16 Channels. The stretchers are also NIM based modules. The QDCs are VME modules treating 64 channels with a common gate.

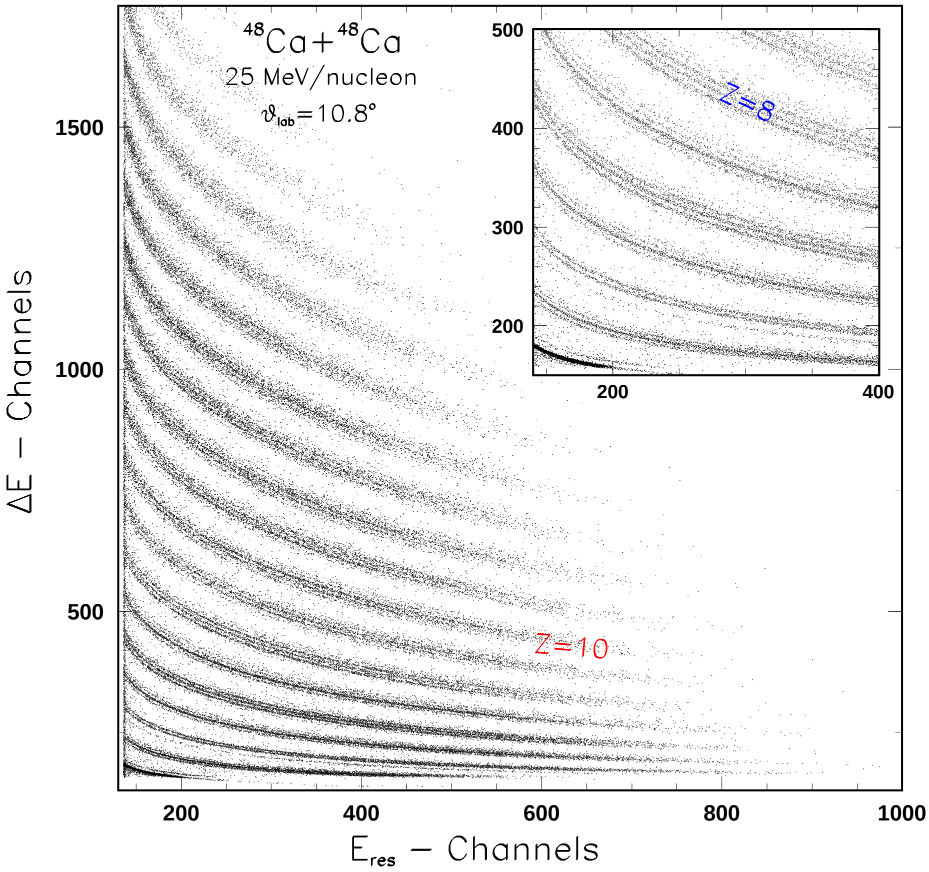

Fig. 2.7: $\Delta E - E$ matrix obtained during the *isospin-1* experiment for a well performing telescope. In this special case, mass identification up to Z=13 isotopes has been obtained. The insert shows a very good mass identification for light ions.

2.5 Particles identification and energy calibrations

During the phase of experimental data taking, all parameters coming from QDCs and TDCs are stored in memory to be analyzed later. The first phase of the analysis consists of data reduction, mainly based on the identification in charge and mass of the emitted particles and on the energy calibrations of the detectors. We will describe briefly the different steps of data reduction performed in the analysis of $^{48}Ca +^{48} Ca$ reaction at 25 MeV/nucleon.

1. **Suppression of QDC pedestals**: pedestals are high and narrow peaks corresponding to zero-energy events in QDC. Being fake signals they must be discarded in order to avoid to produce very large and

unmanageable data files on disk.

2. **QDC gain matching**: Chimera QDCs work in double range of conversion. The main range is called *low gain*, while the secondary, zoomed, range is called *high gain.* The first 512 channels of the low gain fall in the secondary range (4096 high gain channels): for low energy particles we can use a larger number of channels for the conversion, so achieving a better resolution. In order to avoid different matching between the two ranges, we can use pulser signals to extract with accuracy gain and offset parameters.

3. $\Delta E - E$ **identification**: we can identify in charge and eventually in mass those nuclei punching through silicon detectors by means of a $\Delta E - E$ correlation between Si and CsI(Tl) signals. Users must put by hand reference points along the various ridge of scatter plot that will serve as grid for a semi-automatic fit procedure [108]. Functional form of equation describing the ridges is based on Bethe-Bloch formula. Chi square analysis and visual check of identification of various isotopes establish the quality of identification procedure for the different telescopes. Quality codes are assigned to each telescope. In Figure 2.7 we show a $\Delta E - E$ matrix obtained for a particularly good telescope during the experiment *isospin-1* ($^{48}Ca +^{48} Ca$).

4. **Energy calibration of Si detectors**: during *isospin-1* experiment, we performed dedicated energy calibrations of Si detectors by means of four elastic scattering of ^{16}O and ^{12}C nuclei at 30, 50, 60, 80 MeV impinging on ^{197}Au target.

5. **Mass estimate of nuclei stopped in Si detectors**: after the Silicon energy calibrations and charge identification for particles that pass through the Si and stop into the CsI(Tl), by using such information and simple kinematical relations we are able to extract the time offset t_0, that is a fundamental quantity in time of flight measurements. This value must be independent from charge and mass of detected nuclei. A visual check, performed by using dedicated macros of PAW program, allows to verify this property. Check of t_0 extraction procedure constitutes moreover a quite important benchmark for energy calibrations and identification procedures: if something is wrong, calibrations and identification grids must be re-checked. A typical time of flight matrix $\Delta E - ToF$ obtained in the *isospin-1* experiment is shown on Figure 2.8.

6. **Fast-slow identification**: correlations between fast and slow components of light emitted by CsI(Tl) detectors show clearly different ridges, corresponding to various isotopes of light elements, such as hydrogen and helium. A semi-automatic procedure, similar to that

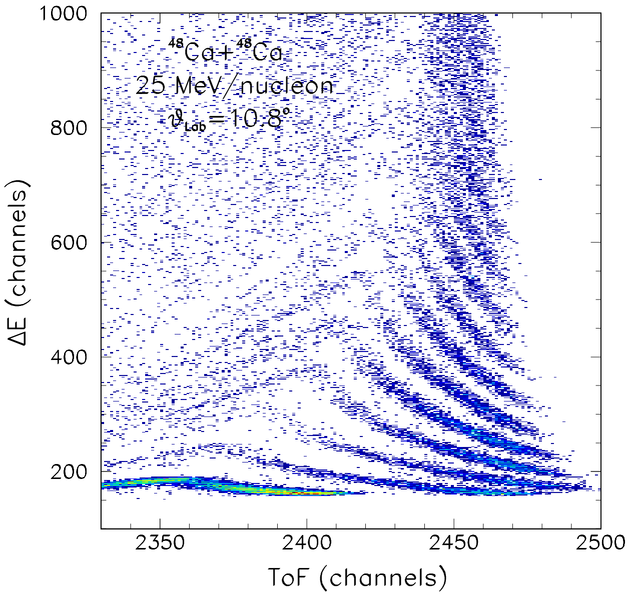

Fig. 2.8: $\Delta E - ToF$ matrix obtained for a silicon detector of ring 5 ($\theta = 10.8°$) for $^{48}Ca +^{48} Ca$ reaction at 25 MeV/nucleon.

described for $\Delta E - E$ identification, has been used. As an example, we show in Figure 2.9 a typical fast-slow matrix obtained during the *limiting* experiment ($^{40}Ca +^{48} Ca$).

For the *limiting* experiment we performed also an energy calibration of CsI(Tl) light output for protons, by using three elastic scattering points (energies from 10 to 62 MeV). Such calibration was cross-checked with the alpha calibration extracted from the *Bose* experiment [1]. The $\alpha - d$ correlation function has been obtained from experimental data: the peak corresponding to the first excited state of ^6Li at $E^* = 2.16$ MeV is clearly visible at the right energy (see [115]), testifying the good quality of the energy calibrations. Energy calibration of CsI(Tl) for protons was re-performed at the beginning of Exochim campaign (2008) by using five elastic and inelastic scattering points on various targets (ranging from 10 to 62 MeV bombarding energy). As seen with previous calibrations, we confirm a good linearity in the energy-light response over the whole energy range considered (see Figure 2.10).

---

[1] Nuclear reaction $^{40}Ca+^{12}C$ at 25 MeV/nucleon. The main aim of the experiment was to search for α particles emitted by the 7.5 MeV excited state of ^{12}C, in connection with a possible signature of Bose-Einstein condensate in dilute nuclear matter. For details, see ref. [114].

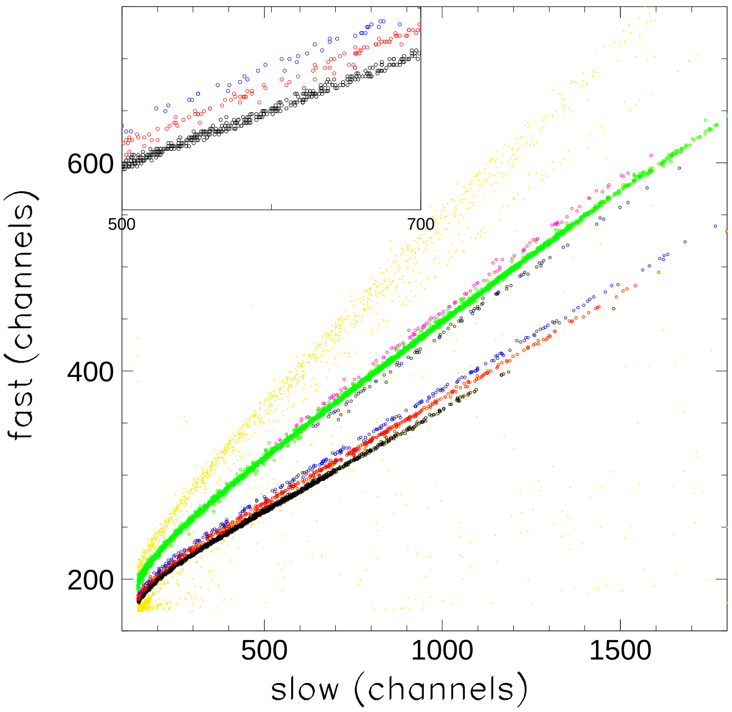

Fig. 2.9: *Fast-slow* correlation obtained for a CsI(Tl) detector during *limiting* experiment. Protons are in black, deuterons in red, tritons in blue. ^3He are in dark blue, ^4He in green, ^6He in violet. Other particles are in yellow. In the insert, a zoomed part of hydrogen lines is shown.

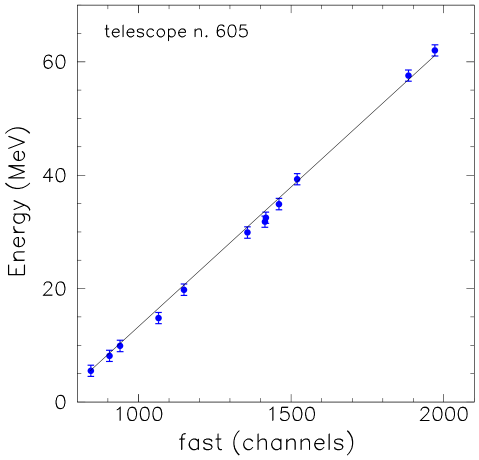

Fig. 2.10: Energy calibration of CsI(Tl) for protons, performed during *calibration* measure. Calibration points have been obtained by using elastic and inelastic scattering of protons on carbon, gold and tin targets, at bombarding energies ranging from 10 up to 62 MeV.

2.6 Recent developments: *pulse shape* on Si detectors

It has been reported that the rise-time of signals obtained from silicon detectors following the interaction of heavily ionizing particles carries with it a Z-signature [116, 117, 118]. Many factors have an influence on rise-time of silicon signals: resistivity, capacitance, trajectory of impinging ions, second-order effects on electrons and holes mobilities, shape of electric field inside detector and, especially, ionization density along the track of particles inside the detector [119].

In particular, the ionization processes that occur after the entrance of heavy particles in silicon detectors have been studied in details in the '80s and '90s. For the sake of simplicity, the ionization and charge collection processes for nuclei impinging on silicon detectors can be divided into three parts [118]: (1) the formation of the initial ionization column; for heavily ionizing nuclei, along the tracks, a "plasma column" is formed; (2) the "erosion" of plasma region by charge removal due both to recombination effects and to the presence of applied electric fields; (3) the drift of charge carriers (holes and electrons) up to the collecting electrodes, due to the applied bias field.

Process (1) is very rapid, occurring within 1-2 ps from the impact of the particle; the most important contributions to the signal rise time τ_{RT} are due then to processes (2) and (3): $\tau_{RT} \approx \tau_{er.time} + \tau_{trans.time}$. $\tau_{er.time}$ is

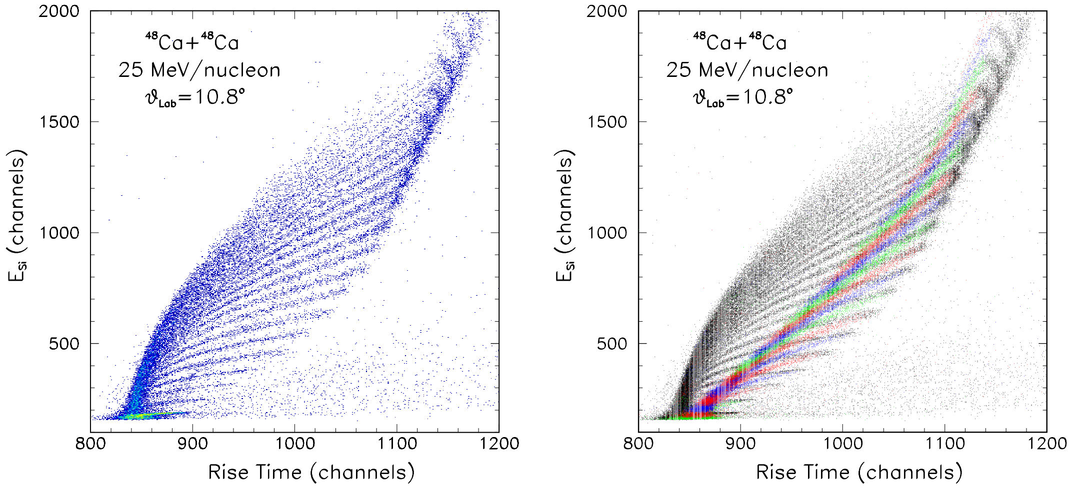

Fig. 2.11: (left panel) Energy-Rise Time matrix obtained for a silicon detector of ring 5. Only particles stopped in silicon have been shown. We can appreciate the very good Z discrimination obtained. (right panel) The same of left panel, but including also particles punching through the silicon detector (in colors). Different colors correspond to the various charges identified by means of $\Delta E - E$ analysis.

called *plasma erosion time*, while $\tau_{trans.time}$ is often named as *transit time*. Some calculations, based on plasma physics and diffusion theory, attempt to parameterize $\tau_{er.time}$ as a function of charge (Z) and mass (M) and energy (E) of incident nucleus [118]:

$$\tau_{er.time} \simeq a \cdot \sqrt{MZ^2} \cdot \sqrt{B(\frac{1}{E} ln \frac{4m_0 E}{MI})/F} \tag{2.3}$$

Here a is a normalization constant, m_0 is the mass of electron, B is the Bethe-Bloch constant, depending on Silicon properties and Avogadro's number, I is the average ionization energy for silicon and F is the applied bias field. Transit times can be calculated easily (as a first approximation) if we assume a constant drift velocity V: $\tau_{trans.} \simeq \frac{W-R/2}{V}$, where W is the thickness of silicon detector and R is the range of the particle in the silicon detector. It is evident that both the terms contributing to τ_{RT} are strongly dependent on the charge of the incident particles. For this reason it is possible to identify in charge (and, eventually, in mass) nuclei stopped in silicon detectors by measuring their rise-time as a function of the incident energy. An example of $E - \tau_{RT}$ correlation obtained for a well performing detector of Chimera array during *isospin-1* experiment is shown on Figure 2.11. The rise-time is measured by means of CAEN 16-ch Spectroscopy Amplifiers that have been described briefly in Sect. 2.4. Charge identification of nuclei from helium up to calcium can be achieved, with identification thresholds of $E \approx 4 MeV/nucleon$ for Z=3,4 ions [120, 121].

2.7 Use of Chimera with unstable beams

The growth and development of new facilities devoted to the production of high intensity radioactive beams open the way to new investigation about isospin physics at low and intermediate energies [1]. By using radioactive beams it is possible to populate intermediate systems with exotic values of N/Z (both on the proton-rich and the neutron-rich side of the nuclide chart, see Figure 1.17) [122]. As an extension of the experimental program described in Chapters 3 and 4, we plan to study incomplete fusion phenomena induced by radioactive beams [123]. The aim is to investigate deeper and deeper the influence of the N/Z degree of freedom on reaction mechanisms, and in particular on the competition between evaporation residue and binary like emission in incomplete fusion events at 25 MeV/nucleon.

As a physics case we will study, by means of in-flight techniques, ^{34}Ar beams at $\approx$ 25 MeV/nucleon bombarding energy, starting from a primary beam of ^{36}Ar fragmenting on a thick ^{9}Be target [124]. By using secondary ^{34}Ar beam (having $N/Z \simeq 0.89$) with intensities around 10^5 particles per second we plan to study incomplete fusion processes in proton-rich systems. For example, we can study the reaction $^{34}Ar +^{40} Ca$ (at 25 MeV/nucleon). We may suppose a reasonable intensity of 10^5 ^{34}Ar nuclei per second impinging on a ^{40}Ca target having a thickness of $2mg/cm^2 \simeq 3 \cdot 10^{19} atoms/cm^2$. The incomplete fusion cross section is of the order of 100 mbarn (see also Figure 1.7); we can expect, as a first approximation, $N = 10^5 \cdot 3 \cdot 10^{19} \cdot 100 \cdot 10^{-3} \cdot 10^{-24} = 0.3$ incomplete fusion events per second (assuming a 100% efficiency for the 4π Chimera array). By using just 3 days of beam time, we will expect around 100000 useful events, a number that is quite sufficient to perform some physical analysis on the N/Z influence on evaporation residue emission.

Fragmentation beams produced and transported up to the Chimera chamber are cocktail beams (i.e. containing different isotopes with similar magnetic rigidity) with a rather large emittance. The use of cocktail beams represents a good opportunity for our investigations. It will allow in fact to study, in the same experiment, nuclear reactions involving nuclei with different N/Z contents. Therefore we need to build a tagging system that will be able to identify in charge and mass, without ambiguities and one by one, nuclei populating the cocktail beam. This device must obviously work in transmission; the energy range of beam particles is about 30-60 MeV/nucleon and the cocktail beam has large emittance. To this aim, we assembled a tagging system based on a large surface micro-channel plate

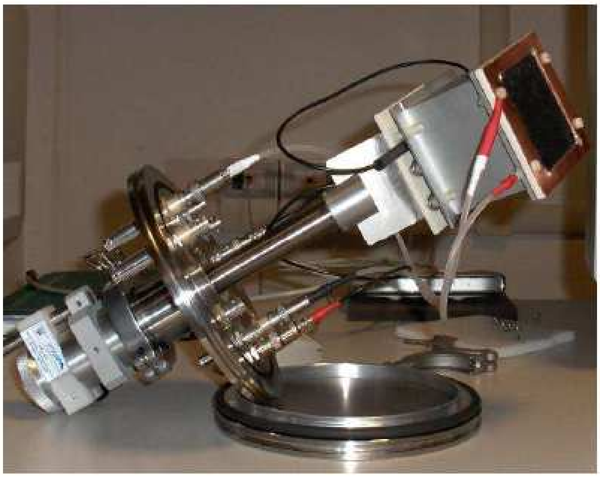

Fig. 2.12: The large surface MCP detector, mounted on a standard ISO-flange.

(MCP) coupled to a double sided silicon strip detector (DSSSD). Details about this device will be shown in Sect. 2.8.

Chimera was built to be a detector for charged particles. However, as it was already discussed in Chapter 1, gamma and neutron detection in coincidence with charged particles is a very important tool to be achieved for new generation 4π detectors. Therefore we decided to perform also a preliminary test by installing four BaF_2 (22.5 cm long) crystals [40] inside the Chimera scattering chamber at a distance of 40 cm from the target, inside the mechanical frame of the Sphere. Preliminary results, discussed in Sect. 2.9, show that a combined analysis of rise-time and time of flight information allows the discrimination of charged particles, γ-rays and neutrons.

2.8 A large surface MCP for the tagging of exotic beams

A large surface MCP [125, 126, 127], to be coupled to the Chimera array for the tagging of exotic beams produced by means of in-flight technique, was assembled starting from the bare micro-channel glasses ($43 \times 63 mm^2$, $700 \mu m$ thick), made by Topag Lasertechnik [128]. MCP glasses were mounted in chevron configuration. We provided also the right electrical contacts and mechanical stability to the whole ensemble. We used an aluminized mylar foil ($2 \mu m$ thick) with an evaporation of LiF ($15 \mu g/cm^2$) as source of electrons that are emitted when the beam impinges on the foil [129]. Those electrons are driven, by using an electric field, to the upper surface of the MCP glasses.

The electron drift region is constituted by a metallic box supporting

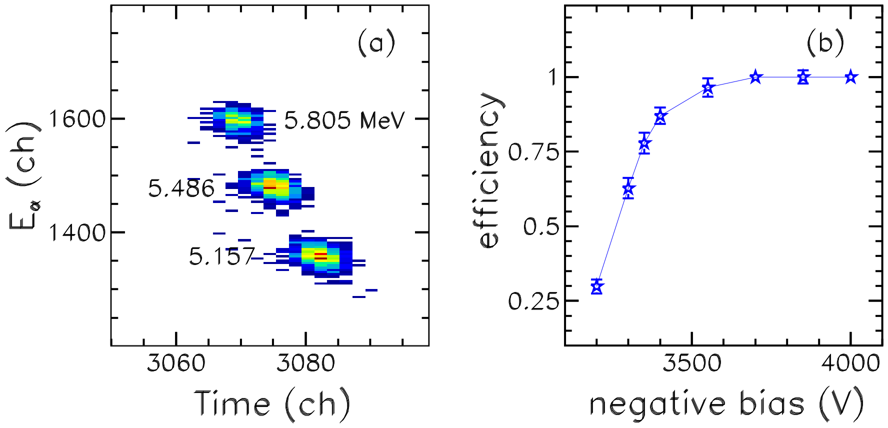

Fig. 2.13: (a) E-TOF matrix obtained by using three peaks alpha source. The TDC conversion factor is $\simeq 230\frac{ps}{ch}$. (b) Efficiency curve of the large surface MCP for α particles, as a function of the bias to the resistive divider.

a grid biased at the same voltage of the upper surface of the MCP. Such box has a lateral opening to allow the beam crossing [129]. The fast signal emitted from the biased MCP is collected by a planar anode. A resistive divider provides the right bias voltages to the emitting foil ($V_f \approx -4200$ V), grid ($V_g \approx -2300$ V) and rear ($V_r \approx -300$ V) [126, 130]. The MCP assembly, mounted on a ISO-flange, is shown on Figure 2.12.

We performed preliminary tests of the tagging system by using a spectroscopic alpha source. In this way, we are able to evaluate efficiency, time and energy resolution of such device. We mounted the alpha source under vacuum, followed by the MCP and, 70 cm far, by a 16×16 strips Double-Sided Silicon Strip Detector (DSSSD) $140\mu m$ thick. Assuming 100% efficiency for the silicon detector, we estimated the efficiency of the MCP, by triggering the MCP signal with the silicon one. By varying the input voltage, we performed the efficiency curve for alpha particles (Figure 2.13b). We are able to get 100% efficiency at ≈ 3700 V to the divider, corresponding to ≈ 1500 V to the chevron.

To evaluate the time resolution of the tagging system we select only one pixel of the DSSSD. In this way we minimize time spread of alpha particles having different trajectories. The time resolution of the MCP-DSSSD was estimated to be about 500 ps FWHM. The new MCP is able to sustain a rate up to 10^6 particles/s without degradation of efficiency and resolution.

In Figure 2.14 we plot the schematic view of the setup of the tagging system used for fragmentation beams. The MCP was mounted ≈ 13 m far from the DSSSD detector. The DSSSD was placed along the beam pipe,

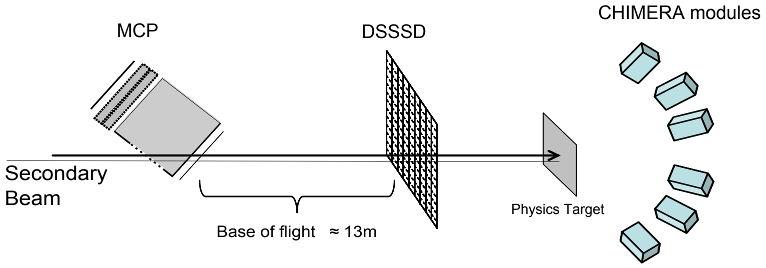

Fig. 2.14: Schematic view (not in scale) of the tagging system setup.

about 1.9 m far from the target. It measures the position of the impinging beam and its energy loss. In Figure 2.15 the identification scatter plot obtained using the energy loss information from one front strip of the DSSSD detector (140μm thick) and the time of flight (TOF) measured respect to the MCP is shown. A primary beam of ^{18}O at 55 MeV/nucleon impinging on a ^{9}Be target 1.5mm thick was used to produce fragmentation beams. The achromatic fragment separator magnets [124] were optimized for the transmission of ^{11}Be ions. In the picture we note many bumps, each one corresponding to a single isotope.

The beam identification can be obtained by comparing these results with predictions of LISE++ calculations [131], using various reference points. For example, in the plot we note a series of isotopes detected with approximately the same TOF (bumps centered at 150 ns). These isotopes have the same velocity; and therefore they must have the same A/Z ratio. In particular, by comparing the picture with LISE++ calculations, we recognize that these isotopes are $^{6}He,^{9}Li,^{12}Be,^{15}B$, having $N = 2 \cdot Z$.

Radiation damage does not degrade noticeably the performances of DSSSD, especially when it is used to tag light intermediate energy ions. During the performed experiments, we irradiated the 140μm detector with a total flux of about 3.6×10^9 ions. The observed increase of total reverse current was only $\approx 200nA$.

The evaluation of the MCP efficiency is a fundamental point, being different for the different detected ions. In Figure 2.16 we plot again the events of Figure 2.15, together with the events for which we do not have a signal from the MCP. For these events we measure the time respect to the Cyclotron radio-frequency (RF).

From the comparison of the two panels we note a much clear identification obtained using the MCP. It allows in fact a correct measurement of the TOF, while with RF we must limit our time measurement to a maximum time interval of only 30 ns (the RF cycle). However the plot with RF can be useful, especially for very light ions, to recover those events where we do not have the MCP signal because of efficiency of this device. The two plots have the same scale on the z axis; we can therefore evaluate the effects of

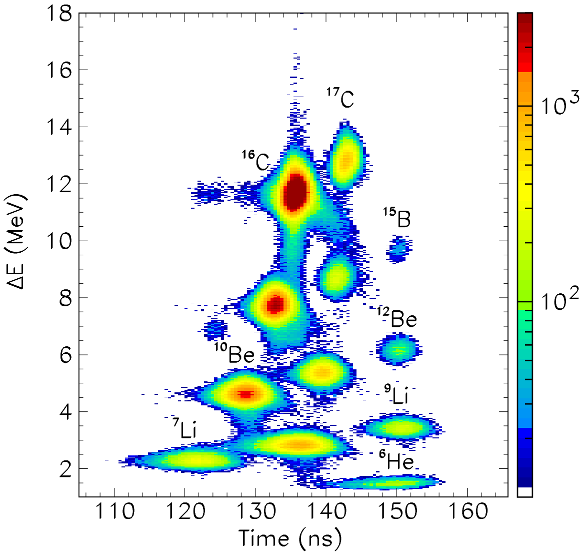

Fig. 2.15: $\Delta E - TOF$ scatter plot obtained by correlating energy loss and time of flight given by DSSSD and MCP of the tagging system. Some of the isotopes composing the cocktail beam have been labeled.

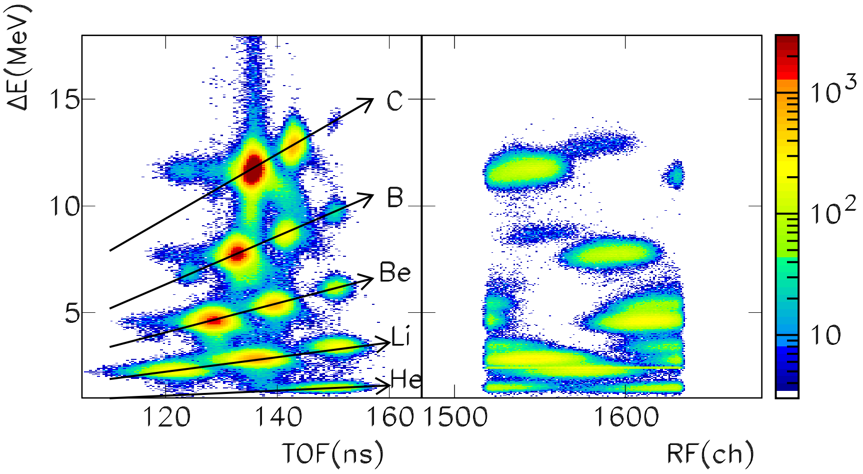

Fig. 2.16: (left panel) $\Delta E - TOF$ scatter plot for fragmentation beams. MCP signals are used as start signals for TOF measurements. (right panel) $\Delta E - TOF$ scatter plot obtained for those events where MCP time signals are absent; in this case we use RF as time reference for TOF calculation.

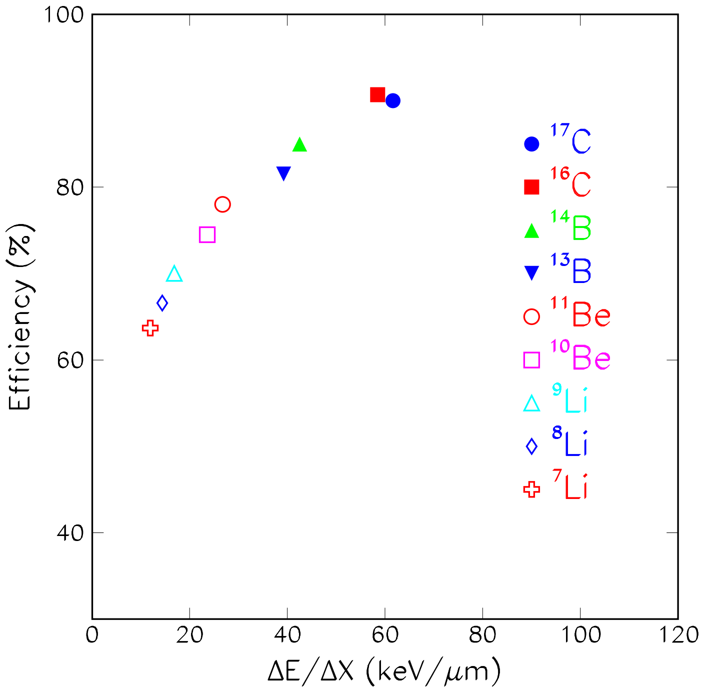

Fig. 2.17: Efficiency of MCP as a function of the $\Delta E/\Delta X$ for different fragmentation beams.

the MCP efficiency as a function of the detected ion. By observing the population of the two scatter plots of Figure 2.16 we note that while relatively few events are lost in case of heavy fragments, we have a smaller efficiency in the case of light fragments. In Figure 2.17 we plot the detection efficiency for fragments collected as a function of their specific energy loss ($\Delta E/\Delta X$) on the aluminized mylar + LiF emitting foil. As suggested in ref. [132], we infer that the efficiency is correlated to this physical quantity, that can be linked to the electron emission probability of the surface. Other parameters that may influence the efficiency are the electric field of the collecting grids and the electronic threshold of the discriminator. It is interesting to underline that, by extrapolating the results from Figure 2.17, with ^{34}Ar beam we may expect an efficiency near to 100% for our micro-channel plate.

2.9 Test of BaF$_2$ detectors for γ and neutron emission

Barium Fluoride (BaF_2) have been widely used as radiation and particles detectors in various experiments (both at medium and high energies). Their main characteristic is to emit two components of light (fast and slow). The fast component has a very rapid decay constant ($t \simeq 600ps$); it is therefore useful in determining the stop signals with very good time resolution in time of flight measurements. Moreover the relative weight of the fast and the slow component is strongly dependent on the ionization density of the incoming particles; in particular the fast component shows large variation as a function of the stopping power dE/dx. For this reason, it is possible to discriminate charged particles and gamma rays by performing a pulse shape analysis on BaF_2 signals [133].

In our test, we used four BaF_2 taken from the TRASMA array [40]. In previous measurements, they were used in air to detect gamma rays coming from heavy ion collisions at 10 and 25 MeV/nucleon [42, 134]. Due to their large thickness (22.5 cm) they are able to detect GDR gamma rays with a good efficiency. Before inserting BaF_2 crystals into the Chimera chamber, we performed many laboratory tests: we put crystals in vacuum ($10^{-2}mbar$) and we measured signals due to a ^{60}Co source. Peak-to-valley ratio was found to be not so good due to the deteriorated optical matching between the crystal and the phototube. The stability of detector response was tested on a long time measurement with a ^{60}Co source; as expected, due to the heating of phototube in vacuum, during the first 6 hours of data acquisition, the signal drifted towards lower channels. After 12 hours, however, thermal equilibrium with the surrounding environment is achieved and the gain stabilizes (see Figure 2.18). However, for the sake of safety, during the experimental shifts, the stability of gains of phototubes was checked by means of a *light pulser*. It was based on a LED, followed by optical fiber put in contact with the crystal. The LED was biased by means of a waveform generator.

The four used crystals were inserted into the frame of the Sphere, at polar angles of $\theta = 74°$ and $106°$. The flight length from the target was $\approx 40cm$. The anode output was sent directly to a CAEN Pulse-Shape Spectroscopy Amplifier (see also Sect. 2.6). This multi-purpose module give us a standard amplified signal ($2\mu s$ shaping time), that we sent to a QDC for the analog to digital conversion. Inside the pulse-shape module, a fast timing amplifier processed the anode signal with a $200ns$ shaping time. Two discriminators provide two logic signals at 30% and 80% of the peak maximum. Due to the scintillation properties of BaF_2, the rise time of this processed signal will be sensitive mainly to the fast component of the emitted light, that is different for γs and charged particles [135, 136, 137]. Simultaneously, a time of flight measurement was performed, taking the radio-frequency of our cyclotron as a stop signal and 30% logic signal from CAEN Spectroscopy Amplifier as a start reference. The correlation between rise-time and time-of-flight signals obtained during $^{48}Ca +^{48} Ca$ shift at 25 MeV/nucleon is shown on Figure 2.19a. Three mainly populated regions can be distinguished in the rise-time time-of-flight scatter plot $\{rt; tof\}$: (1) a strong bump well centered

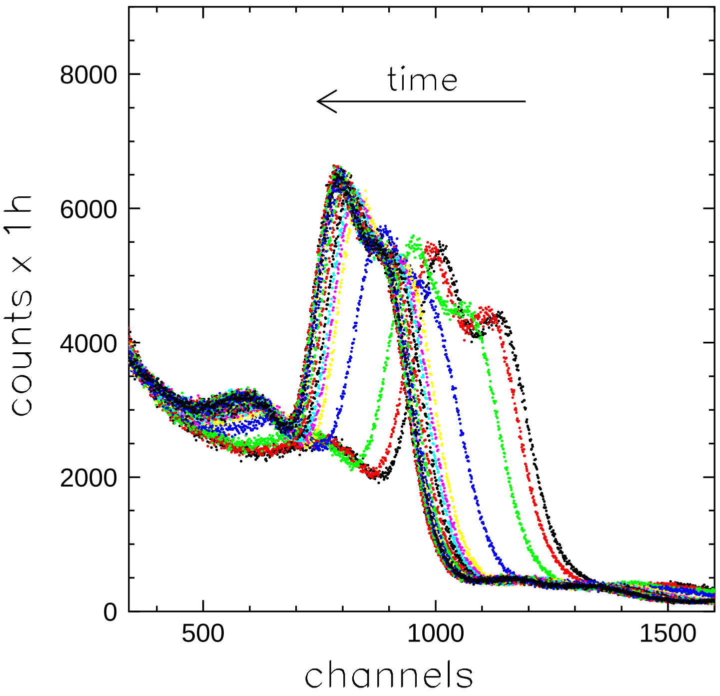

Fig. 2.18: Response of large volume BaF_2 crystal of the TRASMA array for a standard ^{60}Co γ source as a function of time. Crystals were used under vacuum ($10^{-2}mbar$). The rightmost spectrum is taken after 1 hour of acquisition from the switch-on of the phototube; from right to left, other spectra are taken continuously after one hour of data acquisition. We followed the behavior of detector response continuously for 19 hours; after $\approx$ 12 hours the gain stabilizes.

at $\{rt; tof\} \simeq \{570; 2580\}$; (2) a broad distribution of events having rise-time similar to that of case (1) ($rt \simeq 570ch$) but with large time-of-flight variations (from 2440 to 2570 channels in tof); (3) a tail of events where both time-of-flight and rise-time are different compared to the previous two cases.

Events labeled as (1) are mainly due to γ rays arriving on BaF_2 crystal. They are strongly peaked to a given value of time-of-flight because of the fixed value of speed of light. Events indicated as (2) have the same rise-time of previously mentioned γ rays but with a broader range of time of flight values. They are then expected to be neutrons entering into the BaF_2 crystal and leading to (n,γ) reactions in the detector: in this respect, they will have the same rise time of direct γs, but with time of flight shorter[2] than in the region (1). Region of events labeled as (3) are instead due to charged particles (as p, d, t, α). We proved this assumption by studying another BaF_2 crystal, put at the same polar angle as the previous detector, that was covered by a thick (2 cm) aluminium absorber. With this absorber, we stopped almost all high energy light charged particles (up to protons having $E \approx 70MeV$, according to the LISE++ program). For this masked detector, in the rise-time vs time-of-flight correlation, the region of events (3) disappears, strongly confirming that events labeled as (3) are due to charged particles. In Figure 2.19b we plot the energy spectrum of γ rays of region (1) (they have been selected with a graphical cut). The shape of the spectrum is similar to that obtained selecting γ rays emission during data taking with the TRASMA array (see Figure 1.12). Panel (c) shows instead the energy spectrum of particles in region (3): it seems clearly due to the sum of light charged particles spectra. In panel (b) a time of flight spectrum of neutron detected as (n,γ) is shown. We can transform this spectrum into energy spectrum; the obtained energy spectrum must be convoluted with the neutron efficiency curve evaluated by the TAPS collaboration for the same type of BaF_2 crystals [138]. These results show that using BaF_2 crystals at backward angles coupled to the Chimera array it is possible to obtain at the same time information about emission of γ rays and neutrons. Both these signals, taken in coincidence with charged particles detected by the Chimera array, can be of extreme importance to disentangle the poorly known behavior of the symmetry potential in the nuclear equation of state (see Chapter 1).

---

[2] We remember that we are measuring time of flight in reverse logic: time of flight = start time - stop time + offset. For this reason time of flight distribution is reversed: the fastest particles, i.e. γ rays, appear to have the largest time of flight.

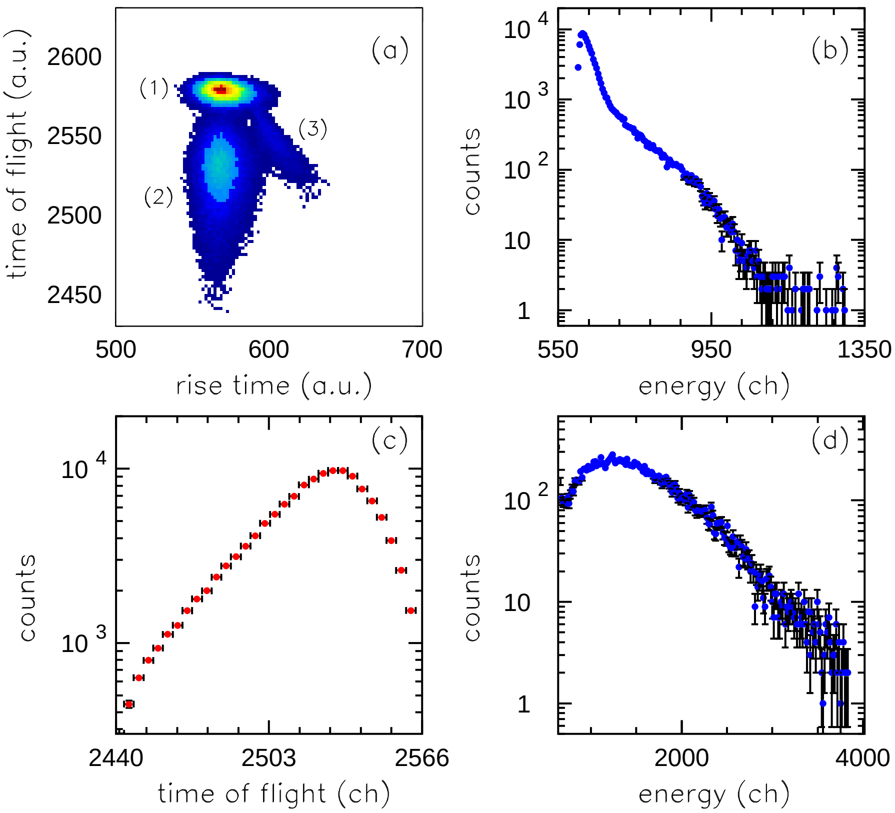

Fig. 2.19: (a) Rise time - time of flight correlation for signals given by a BaF_2 crystal during $^{48}Ca +^{48} Ca$ shift at 25 MeV/nucleon. (b) Energy spectrum of γ rays, region (1), see text. (c) Time of flight spectrum for neutrons, mainly laying in region (2). (d) Energy spectrum for charged particles, region (3) of the scatter plot.

Chapter 3

N/Z effects on Ca+Ca,Ti reactions at 25 MeV/nucleon

In this Chapter we show some results obtained by analyzing nuclear reactions $^{40}Ca + ^{40,48}Ca, ^{46}Ti$ at 25 MeV/nucleon (*limiting* experiment). These reactions cover a wide range of N/Z in the entrance channels (from N/Z=1 for $^{40}Ca + ^{40}Ca$ up to N/Z=1.2 for $^{40}Ca + ^{48}Ca$). This allowed us to investigate on the influence of the isospin degree of freedom in inclusive, semi-central and semi-peripheral collision events.

After a brief description of the experimental settings, we will analyze the inclusive emission of light isotopes and isotones. The dominating reaction mechanisms are inferred from Dalitz and velocity correlations of the largest fragments emitted in each event of the studied reactions. In Section 3 we analyze semi-central incomplete fusion events, where only a part of the projectile fuses with the target. A strong influence of the N/Z on the competition between heavy residues production and binary-like events has been observed. Calculations performed with the CoMD-II model [89] agree nicely with the experimental mass distributions when we parameterize the symmetry potential with a stiff ($\gamma = 1 \pm 0.15$) density dependence. We studied also thermodynamical quantities (apparent temperature and excitation energies) characterizing incomplete fusion sources populated in the mentioned reactions.

Semi-peripheral collisions have also been investigated. In particular, our aim was to extract information about the N/Z content of quasi-projectile (QP) and mid-velocity (MV) sources to probe isospin diffusion and drift phenomena. In Section 5 we will discuss isospin transport effects by studying the production of isotopes ($^{6,7}Li$ and $^{7,9}Be$) and isobars (^{7}Li and ^{7}Be) in the studied reactions at 25 MeV/nucleon.

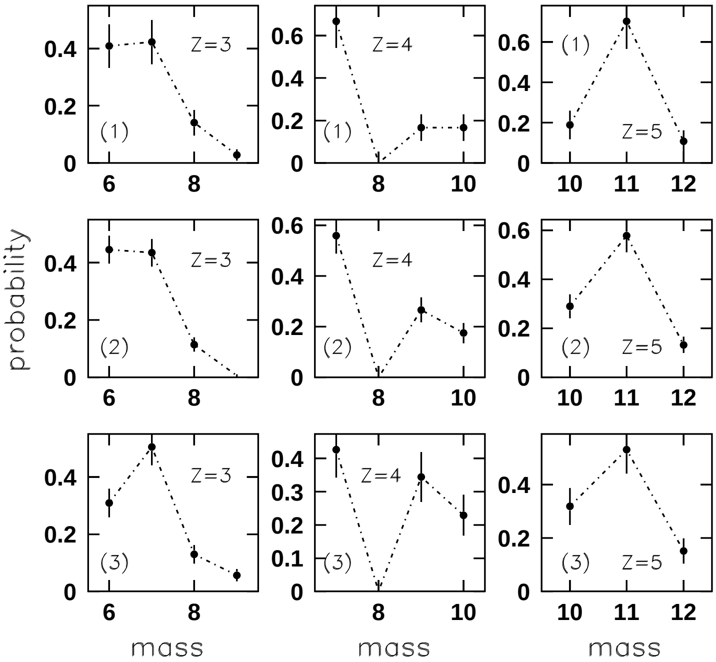

Fig. 3.1: Isotopic yield distributions of different light isotopes (Z=3,4,5) for the studied reactions at polar angles $\theta_{lab} = 8.5°$. First row (1): $^{40}Ca + ^{40}Ca$ reaction. Second row (2): $^{40}Ca + ^{46}Ti$ reaction. Third row (3): $^{40}Ca + ^{48}Ca$ reaction. The yields have been normalized to the total yields for a given atomic number, Z.

3.1 Details on experimental phase

The experiment was performed at INFN-LNS Super Conducting Cyclotron facility. A beam of ^{40}Ca at 25 MeV/nucleon with intensity ≈200 pA impinged on self-supporting, isotopically enriched targets of ^{40}Ca (thickness 1.24 mg/cm^2), ^{48}Ca (thickness 2.87 mg/cm^2), ^{46}Ti (thickness 1.06 mg/cm^2). To detect the nuclear products we used Chimera, already described in Chapter 2. The time resolution obtained during the experimental shifts is $\approx 800ps$ FWHM, dominated mostly by the timing characteristics of the beams. The obtained mass resolution ($\frac{\Delta m}{m}$) is around 5% for nuclei having masses $A \approx 50$, typical of evaporation residues detected in these reactions.

In order to remove spurious reaction events, we imposed an off-line selection criterion, defining as ”good” events only those having a total detected charge $32 \leq Z_{tot} \leq 40$ for the $^{40}Ca +^{40,48} Ca$ reactions, and $32 \leq Z_{tot} \leq 42$ for the $^{40}Ca +^{46} Ti$ one. In order to ensure the completeness of selected events, we also required the sum of all fragment momenta to be larger than 70% of the initial momentum. Thus spurious reactions on oxygen contaminants were rejected and pile-up events are strongly reduced.

Energy calibrations were performed, both for silicon and CsI(Tl) detectors, using elastic and inelastic scattering of calibration beams (see also Chapt. 2). To remove the most peripheral collisions, the experimental on-line trigger required at least the presence of 3 silicon detectors fired by charged particles.

3.2 GENERAL CHARACTERISTICS OF THE COLLISIONS

3.2.1 Emission of isotopes and isotopic effects

The analyzed collisions involve systems having different N/Z values in entrance channels. In particular $N/Z_{^{40}Ca+^{40}Ca} = 1$, $N/Z_{^{40}Ca+^{46}Ti} = 1.05$, $N/Z_{^{40}Ca+^{48}Ca} = 1.2$. In order to check isotopic effect, discussed in Section 1.3.2, we plot in Figure 3.1 the inclusive isotopic distribution for Z=3,4,5 nuclei emitted at forward polar angles (8.5^o, black circles).

In the case of Li isotopes emission, we observe that ^6Li and ^7Li are about equally emitted for $N \simeq Z$ systems ($^{40}Ca +^{40} Ca$ and $^{40}Ca +^{46} Ti$). In contrast, in the case of the neutron rich system $^{40}Ca +^{48} Ca$, the ^7Li emission probability is much higher than the ^6Li one. A similar trend can be observed by studying the emission of ^7Be and ^9Be (central column of Figure 3.1). While for $N \simeq Z$ systems we observe a high probability of emitting ^7Be compared to $^{9,10}Be$, for the neutron rich system we observe an higher probability of emitting the neutron rich Be isotopes. It becomes more difficult to make similar observation for the boron isotopes; in all cases, the isotopic distribution is peaked at ^{11}B. In general, however, a strong isotopic effect is observed for light isotopes.

3.2.2 Odd-even effects in Z- and N-distributions

When the dynamical stage of a nuclear reaction at energies well above the Coulomb barrier ends, one can observe the production of one or more excited nuclei. These fragments must de-excite by means of neutrons and light charged particles emission in an evaporation cascade. The experimentally observed yields of the final detected fragments can be therefore related to the last steps of the de-excitation chain. In particular, the separation energies of one proton and one neutron for fragments having low atomic number ($Z < 12$) play an important role in determining structure effects on final isotopic distributions experimentally observed. In the literature, a number of isotopic distributions of fragments emitted at forward angles has been reported, especially for collisions at bombarding energies larger than 5 MeV/nucleon [139, 140, 141, 142, 143]. At variance, it is more difficult to find in the literature measurements of isotonic distributions of good quality [91]. In order to highlight this topical subject, we show in Figure 3.2 Z- and N-distributions for light fragments ($Z \leq 13, N \leq 10$) emitted in the three studied reactions and identified in charge and mass by means of the $\Delta E - E$ technique (see Chapter 2).

A local minimum is seen clearly at Z=4 and Z=9 (beryllium and fluorine production) in the Z-distributions. The local minima at Z=4 can be explained by studying the one-proton and one-neutron separation energies of ^{9}Be. If in the final stage of a de-excitation chain a weakly excited nucleus of ^{9}Be is populated ($E^{*} \sim 2 - 3$ MeV), it has a large probability of de-exciting with an emission of one neutron, due to the low one-neutron separation energy ($E_S^{1n} = 1.66$ MeV). The resulting ^{8}Be nucleus is unbound and decays into two alpha particles. This can qualitatively explain the depletion of beryllium (Z=4) yields compared to other fragments.

The depletion of fluorine emission (Z=9) is probably due to the fact that the most stable nuclei near to the fluorine isotopes (such as $^{20,21,22}Ne$) have high values of the one-proton separation energy ($E_S^{1p} \approx 13$ MeV); even if one of these Ne isotopes is produced in an evaporation cascade with a relatively high excitation energy ($E^{*} \lesssim 13$ MeV), it is impossible for them to de-excite by means of one proton emission. Similar qualitative arguments can be performed for the N-distributions.

Figure 3.2 displays another interesting feature; excluding Z=4 and N=4 (for $N \approx Z$ systems) cases, Z- and N-distributions show an odd-even effect, i.e. fragments with even Z- or N- values are emitted with a higher probability as compared to those with odd values. This effect can be explained by taking into account the pairing effect in nuclei; in particular, nuclei with an even number of protons are more bound with respect to nuclei with an odd number of protons (the same argument is obviously valid for the neutron number). One proton or one neutron separation energies are higher for even N or Z as compared to the odd cases. For this reason particle

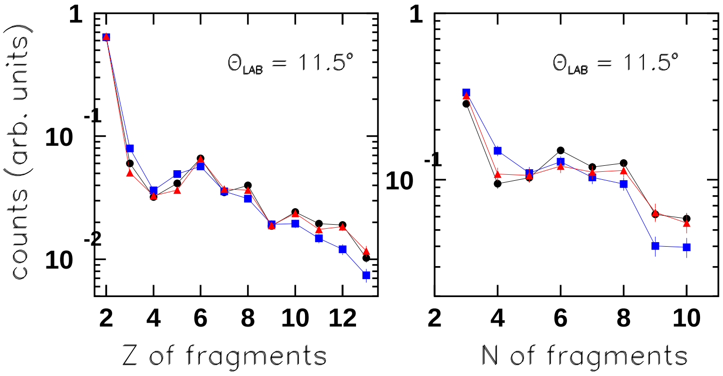

Fig. 3.2: (Left panel) Z-distributions of fragments emitted at forward polar angles ($\theta_{lab} = 11.5°$) for the $^{40}Ca +^{48} Ca$ (blue squares), $^{40}Ca +^{46} Ti$ (black circles) and $^{40}Ca +^{40} Ca$ (red triangles) reactions. (Right panel) N-distributions of fragments emitted at forward polar angles. The use of symbols and colors is the same of the left panel. Isotopic discrimination is obtained by means of $\Delta E - E$ technique in Si-CsI(Tl) telescopes.

emission thresholds for nuclei with odd N or Z are considerably lower, thus increasing the probability of de-excitation by one particle emission in the last stages of the de-excitation cascade. Another observation on Figure 3.2 concerns the different amplitudes of staggering effects for the three studied reactions. On the left panel we observe that a stronger even-odd effect on charge distribution is seen for the $N \simeq Z$ systems $^{40}Ca +^{40} Ca,^{46} Ti$ compared to the neutron rich $^{40}Ca+^{48}Ca$ reaction. This finding is consistent with experimental findings previously reported in the literature [140, 143]. A phenomenological explanation of such a behavior has been recently proposed in refs. [141, 142]; it was based on pairing effects on separation energy distributions characterizing light nuclei lying near the stability valley.

3.2.3 General features of the collision dynamics

In the energy regime of ≈ 20 MeV/nucleon, two classes of reaction mechanisms dominate the evolution of a nuclear collision, as a function of the impact parameter [1, 51]. In semi-peripheral collisions the presence of binary-like phenomena has been reported. This kind of mechanism can be considered as a high energy evolution of deep inelastic processes (DIC) dominating nuclear collisions at over-barrier energies. Differently from low energy DIC, in this energy range the emission of the two main fragments (quasi-projectile and quasi-target) can be accompanied by other fragments emitted by the excited zone of overlap of the two colliding nuclei, travelling at mid-velocity in phase space. At more central impact parameters, quasi-compound nuclei with high excitation energies are formed essentially by means of the incomplete fusion mechanisms (see Chapt. 1).

We probed the characteristics of dominating mechanisms by constructing Dalitz correlation plots using the three largest fragments emitted in each event of the studied reactions. The behavior is similar for the three reactions, and it is shown in Figure 3.3. Events characterized by the emission of one large and two small fragments in the exit channels dominate, as testified by the large peaks at the vertex of the triangles. This type of events can be associated to incomplete fusion scenarios. We observe also an abundant presence of binary-like collisions, where two fragments having similar masses are emitted. These events lay at the sides of the Dalitz triangles. The cross section for ternary emission (three fragments of similar size, center of the triangles) is lower with respect to the other two cases, due to the relatively low bombarding energy involved.

Binary-like and incomplete fusion events can be separated, for example, by means of constraints on the mass of the largest fragment (m_1) and on the velocities of the two largest fragments (v_1, v_2) emitted in each event of the studied reactions. For example, in Figure 3.4 we show the correlation between the velocities of the two largest fragments emitted (we show the case of $^{40}Ca +^{46} Ti$ reactions, the other two systems give similar results). If we select events where $m_1 \geq 46$ amu, i.e. events where an heavy residue is detected, velocity correlations show a large bump at v_1 near (but slightly lower than) the center of mass velocity ($v_1 \simeq 0.085c$; $v_{cm} = 0.107c$) and v_2 around 0.15c (the projectile velocity, v_{beam}, is equal to 0.23c). Such type of events belong to incomplete fusion mechanisms, where a part of the projectile nucleus fuses with the whole target. These events are characterized by the emission of evaporation residues with large mass and velocity slightly lower than the center of mass one due to momentum conservation [2]. The mean velocity of the second largest fragment, v_2, is noticeably higher than the center of mass one, testifying that the second largest fragment is a fast remnant of projectile nucleus. We can observe also from Figure 3.4 (right panel) that $v_2 < v_{beam}$, a typical feature of kinetic energy damping involving massive transfer phenomena. The inverse process, where a part of the target nucleus fuses with the whole projectile, is cut because the targets used in the experiment are relatively thick ($\approx 1-2mg/cm^2$); in this way slow quasi-target remnants are stopped in the target and the detected events do not fulfil the constraints on charge and momentum completeness.

We analyzed also velocity correlation where the largest fragment mass is $m_1 \leq 30$, lower than the projectile and target masses. In this case, the correlation shows clearly two main bumps in two regions of v_1 and v_2 near to the projectile velocity ($\approx 0.2c$) and target velocity ($\approx 0.03c$). These events are produced in damped binary-like events. Also charged particles multiplicity (m_{cp}) seems to be a rough selector of impact parameters (see also [144]). In Figure 3.5 we plot the v_1, v_2 correlations as a function of different

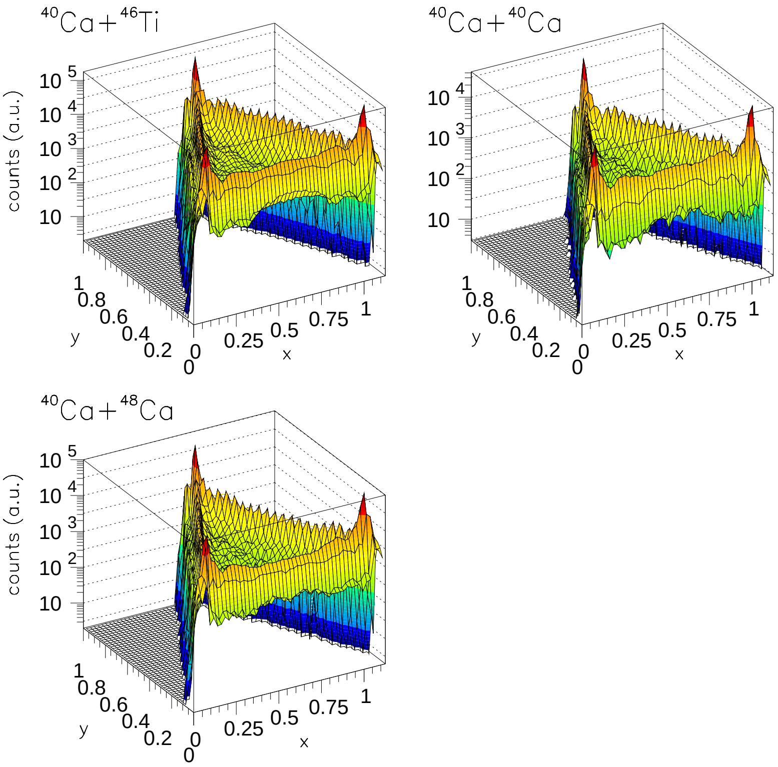

Fig. 3.3: Dalitz plots obtained by analyzing the masses of the three largest fragments emitted in each event of collision for the three reactions $^{40}Ca +^{48} Ca$, $^{40}Ca +^{46} Ti$ and $^{40}Ca +^{40} Ca$. m_1, m_2, m_3 are the masses of the three largest fragment emitted. In the y-axis we put the quantity $y = \frac{m_i}{\sum_{j=1}^{3} m_j}$ for $i = 1, 2, 3$. In the x-axis we put $x = \frac{m_i + 2m_k}{\sqrt{3}\cdot\sum_{j=1}^{3} m_j}$ for $i = 1, 2, 3$ and $k \neq i$. In this way, correlations are symmetrized.

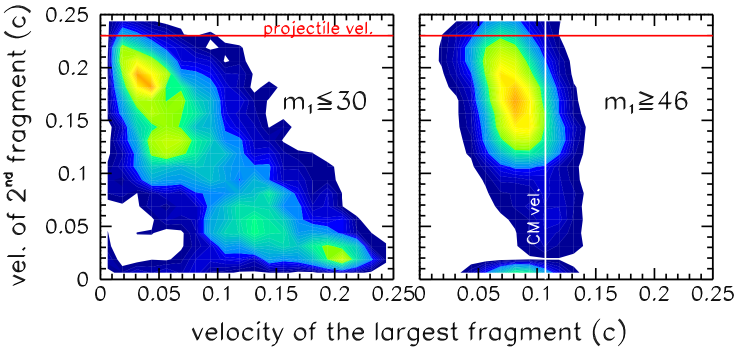

Fig. 3.4: Velocity correlations for the two largest fragment emitted in ^{40}Ca+^{46}Ti reaction. Red horizontal line: projectile velocity ($v_{proj} \simeq 0.23c$). White vertical line: Center of Mass velocity ($v_{cm} \simeq 0.107c$).

bins of m_{cp}, for ^{40}Ca+^{46}Ti reaction. A clear evolution from gentle collisions ($m_{cp} < 5$), characterized by two large fragments having velocities similar to those of projectile and target nuclei, to damped collisions ($m_{cp} > 7$), where the largest nucleus has a velocity similar to the center of mass one, can be observed.

In conclusion, it seems that the different reaction mechanisms mostly involved in the analyzed nuclear reactions can be discriminated by means of constraints on charged particle multiplicity and on the mass and velocity of the largest emitted fragments, provided that we detect almost all the particles emitted in the collisions.

3.3 N/Z EFFECTS ON DYNAMICS OF CENTRAL COLLISIONS

3.3.1 Competition between different reaction mechanisms

The isospin asymmetry dependence of the competition between different reaction mechanisms could represent a strong probe of the influence of the symmetry term of the Equation of State on the dynamical evolution of a nuclear reaction. We will show that the reaction dynamics for semi-central collisions is strongly influenced by the different N/Z contents in the entrance channel [145, 146, 147]. In this section we discuss these experimental results. First of all, following the indications of Figure 3.5, we discarded the most peripheral events by means of constraints on the multiplicity of charged particles (m_{cp}). m_{cp} distributions are displayed in Figure 3.6 for ^{40}Ca+^{48}Ca (blue solid histogram), for $^{40}Ca +^{46} Ti$ (black dots), and for $^{40}Ca +^{40} Ca$ (red gridded histogram) reactions. The maximum in m_{cp} distributions is shifted back by one unit in the case of ^{48}Ca targets; this is probably due

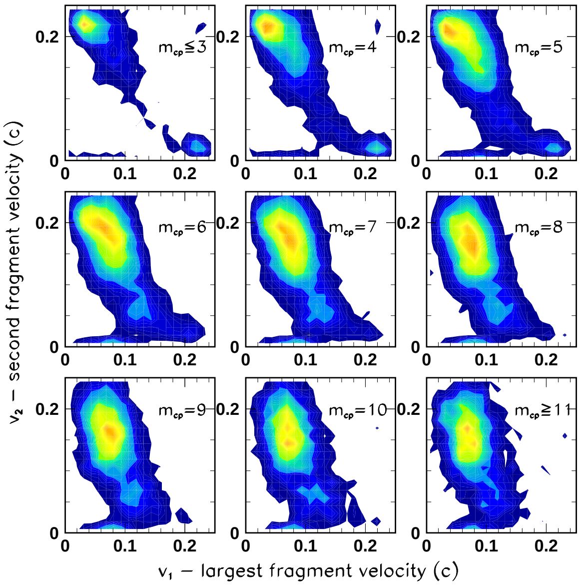

Fig. 3.5: Velocity correlations for the two largest fragment emitted in $^{40}Ca + ^{46}Ti$ reaction, as a function of different bins of charged particles multiplicity (m_{cp}).

to the larger probability of emitting neutrons (that are undetected) in this neutron-rich reaction. Taking into account this finding, only events with $m_{cp} \geq 5$, in the case of ^{48}Ca target, and $m_{cp} \geq 6$ in the case of ^{46}Ti and ^{40}Ca targets, have been selected.

We constrained also the velocity of the second or third heaviest detected fragment to be larger than 0.13c, to better select events where incomplete fusion occurs. In these incomplete fusion reactions, the part of the projectile that does not fuse with the target is expected to move with a velocity close to that of the projectile ($v_{proj} \simeq 0.23c$). The applied selection suppress events where only a part of the target fuses with the projectile and the remaining part behaves like a spectator. Correlation plots between the mass, m_1, and the velocity, v_1, of the largest fragment emitted in the selected events of $^{40}Ca+^{48}Ca$, $^{40}Ca+^{46}Ti$ and $^{40}Ca+^{40}Ca$ reactions are displayed on Figure 3.7.

The distribution on Figure 3.7a is peaked in the region of velocities $v_1 \approx 0.09c$, similar to the center of mass velocity ($v_{cm} = 0.105c$), and with mass $m_1 \simeq 50$ amu. These large fragments are evaporation residues produced in incomplete fusion events. The distributions obtained for the other two reactions (Figure 3.7b,c) regardless their similarities, show some marked differences. Target-like nuclei, with a velocity lower than 0.04c, are seen more copiously in the case of a ^{46}Ti targets (Figure 3.7b) than in the case of

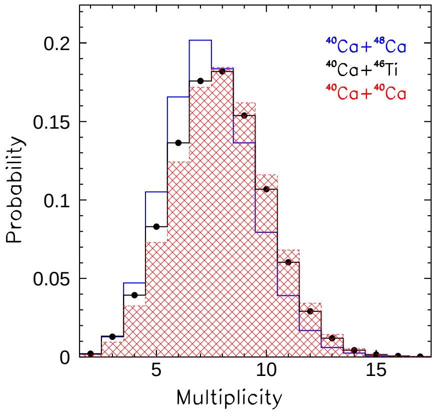

Fig. 3.6: Charged particle multiplicity distributions for $^{40}Ca +^{48} Ca$ (blue solid histogram), $^{40}Ca +^{46} Ti$ (black dots), $^{40}Ca +^{40} Ca$ (red gridded histogram) reactions.

a ^{48}Ca targets (Figure 3.7a). This effect can be attributed to the different thicknesses of the targets used in the experiment. The ^{46}Ti target was thinner than ^{48}Ca; therefore slow target-like nuclei produced by ^{46}Ti are less trapped into the target material.

Mass distributions for the largest fragment emitted in the three reactions are rather different; it is better observed in Figure 3.7d, where we show the projections of the (m_1, v_1) scatter plots on their mass axis (the cut $0.04 \leq \frac{v}{c} \leq 0.15$ was used to exclude target-like and projectile-like fragments). The distributions are pushed to lower masses in the case of $^{46}Ti,^{40} Ca$ targets. A bump around mass 50 is clearly seen for $^{40}Ca+^{48}Ca$ reaction, and gradually disappears moving from $^{40}Ca +^{46} Ti$ up to $^{40}Ca +^{40} Ca$ reactions.

To investigate in more detail mass correlations, and to give a quantitative definition of the two classes of reaction mechanisms that we study (i.e evaporation residue vs binary-like emission), we plot on Figure 3.8a the difference between the masses of the two largest fragments normalized to the total initial mass of the systems: $\Delta M_{nor} = \frac{m_1 - m_2}{m_{tot}}$. In order to exclude target-like contributions biased by differences in target thickness, we take into account only fragments having velocities greater than 0.04c. The ΔM_{nor} observable minimizes effects due to the small mass difference between the entrance channels and enhances isospin asymmetry effects.

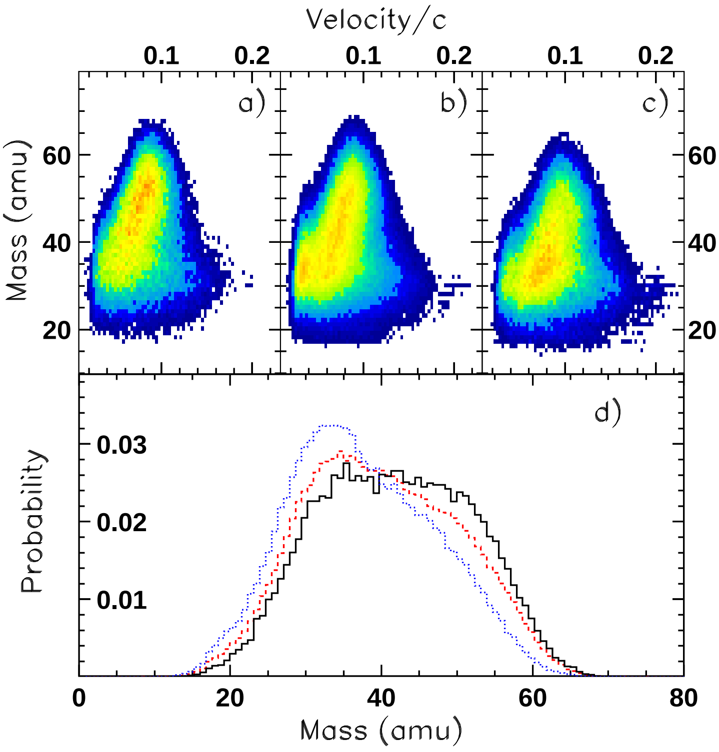

Fig. 3.7: Mass-velocity correlations (m_1, v_1) for the largest fragment emitted in $^{40}Ca + ^{48}Ca$ (panel a), $^{40}Ca + ^{46}Ti$ (panel b), $^{40}Ca + ^{40}Ca$ (panel c). Mass distributions of the largest fragment detected (under the constraint $0.04 \leq \frac{v}{c} \leq 0.15$) in $^{40}Ca + ^{48}Ca$ (black line), $^{40}Ca + ^{46}Ti$ (red dashed line), $^{40}Ca + ^{40}Ca$ (blue dotted line) reactions.

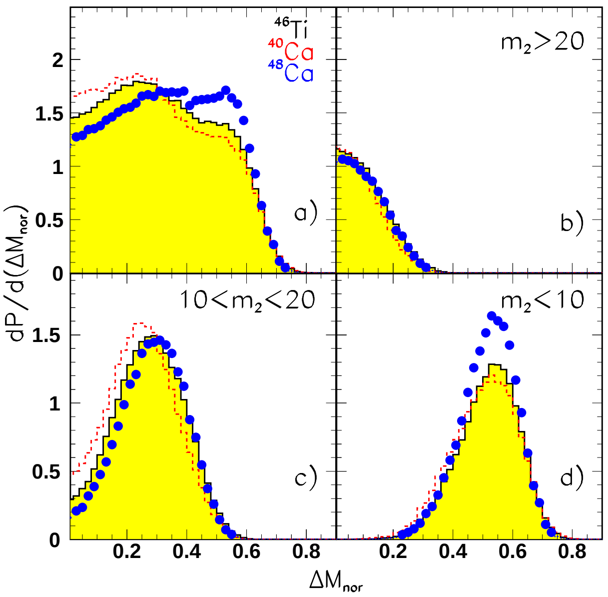

Fig. 3.8: Experimental ΔM_{nor} distribution shown as a function of the different targets used in the experiment. (a) No selection on m_2. (b) Selection $m_2 \geq 20$. (c) Selection $10 \leq m_2 \leq 20$. (d) Selection $m_2 \leq 10$. Blue dots: $^{40}Ca + ^{48}Ca$. Red dashed histogram: $^{40}Ca + ^{40}Ca$. Shadow area histogram: $^{40}Ca + ^{46}Ti$.

In the ΔM_{nor} spectra (Figure 3.8a) we can recognize a local minimum at $\Delta M_{nor} \approx 0.4$. The operative discrimination between the two class of reaction mechanisms can be therefore obtained assuming that events with $\Delta M_{nor} \geq 0.4$ belong to the first class, producing essentially an evaporation residue. By looking at Figure 3.8a, for the case of $^{40}Ca + ^{48}Ca$ reactions, it is evident the enhancement in the region $\Delta M_{nor} \approx 0.5$. On the other hand, in the $N = Z$ symmetric reaction $^{40}Ca + ^{40}Ca$, the distribution is clearly pushed to lower ΔM_{nor} values.

The differences between the three studied systems can be disentangled by looking at the ΔM_{nor} distribution as a function of different selections on m_2, the mass of the second largest fragment (Figure 3.8b,c,d). The constraint $m_2 \leq 10$ amu selects well incomplete fusion events. In this case ΔM_{nor} distributions peak around 0.55; this region corresponds to the emission of evaporation residues. In particular, the probability of populating this region of ΔM_{nor} distribution is higher for $^{40}Ca + ^{48}Ca$ reactions as compared to the other two systems (as it can be seen in Figure 3.8d). This is a clear confirmation of the enhanced production of evaporation residues in the $^{40}Ca + ^{48}Ca$ system. On the contrary, the constraints $m_2 \geq 20$ and

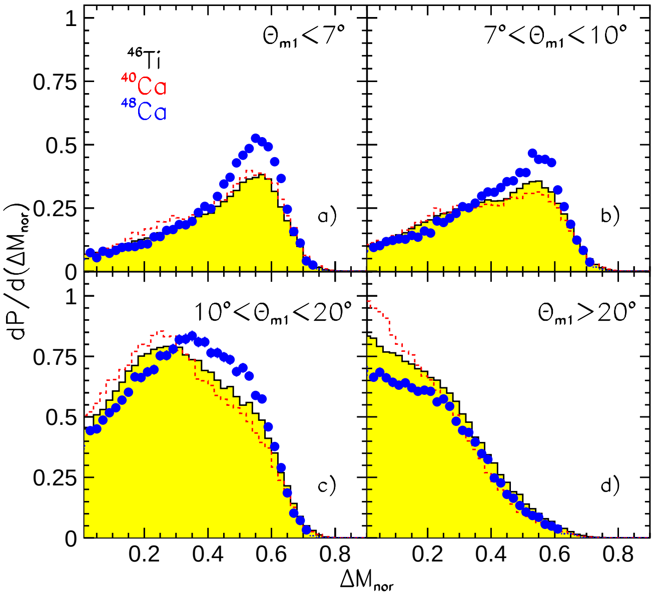

Fig. 3.9: Experimental ΔM_{nor} distributions shown as a function of the different targets used in the experiment. (a) The largest fragment is emitted at a polar angle $\Theta_{m1} \leq 7°$. (b) The largest fragment is emitted at a polar angle $7° \leq \Theta_{m1} \leq 10°$. (c) The largest fragment is emitted at a polar angle $10° \leq \Theta_{m1} \leq 20°$. (d) The largest fragment is emitted at a polar angle $\Theta_{m1} \geq 20°$.

$10 \leq m_2 \leq 20$ are associated to binary-like and fusion-fission phenomena; in fact the ΔM_{nor} distributions are pushed to lower values.

It is also interesting to investigate the ΔM_{nor} distributions as a function of the polar angle of the largest emitted fragment (Θ_{m1}). We are therefore able to study the reaction mechanisms dominating the different angular regions of the space by means of this kind of angular distributions. For example, in Figure 3.9a,b we selected events where the largest fragment m_1 was emitted at very forward angles ($\Theta_{m1} \leq 10°$). In this angular region, the ΔM_{nor} spectra are peaked near 0.6 (a value associated typically to the production of evaporation residues), and the $^{40}Ca +^{48}Ca$ system shows the highest probability of populating high values of ΔM_{nor}. It seems therefore that fusion-evaporation events dominate this angular region. In the panels 9c,d, we selected events where the largest fragment was emitted at larger angles; in this case the ΔM_{nor} distributions are shifted to lower values. This is a clear signal that reaction mechanisms dominating this angular region are of a binary nature, and are associated to the production of two or more fragments of similar masses.

In a qualitative way, the experimentally observed large probability of producing heavy residues for $^{40}Ca +^{48} Ca$ reaction could be related to the larger neutron content of the $^{40}Ca +^{48} Ca$ system. Hot quasi-compound nuclei formed in this neutron rich system are pushed close to the stability valley. On the contrary intermediate systems formed with the $N \simeq Z$ targets are much closer to the proton drip line. In the next section we will show comparisons of our data to dynamical calculations. This will allow a deeper understanding of the role played by the symmetry potential in reaction dynamics.

3.3.2 Comparisons to CoMD-II calculations

In order to explore the mechanisms responsible for the observed effects, we compared our experimental results to calculations performed with the CoMD-II (Constrained Molecular Dynamics II) model [89, 90]. In this model, the dependence of the symmetry interaction per nucleon on the total overlap integral, s, between the wave-packets is characterized by a form factor $F(\frac{s}{s_{gs}})$ (the label gs corresponds to the ground state configuration). This form factor can be expressed, for compact configurations, as $F(\frac{s}{s_{gs}}) = \frac{s}{s_{gs}} \cdot F'(\frac{s}{s_{gs}})$ [89]. Depending on the specific choice of $F'(\frac{s}{s_{gs}})$, one can select a different stiffness of the density dependence of the symmetry energy. Specifically, we used $F'(\frac{s}{s_{gs}}) = \frac{2(s/s_{gs})}{1+(s/s_{gs})}$ (Stiff1); $F'(\frac{s}{s_{gs}}) = 1$ (Stiff2); $F'(\frac{s}{s_{gs}}) = (s/s_{gs})^{-\frac{1}{2}}$ (Soft), suggested from equation of state static calculations and widely used in Boltzmann-Uehling-Uhlenbeck mean-field calculations [82]. The strength factor used for the symmetry interaction is 27 MeV [145]. We underline that the ratios $\frac{s}{s_{gs}}$ and $\frac{\rho}{\rho_{gs}}$ are equivalent within 1%[1]. Another kind of functional for the form factor, which is widely used in the literature, is $\Phi(\gamma, \frac{s}{s_{gs}}) = (\frac{s}{s_{gs}})^{\gamma}$ where γ can be used as a measure of the degree of stiffness. We note that for the Stiff2 option the functional F and Φ are identical (with $\gamma = 1$). To compare with the functional Φ the other two options used, we can reasonably assume that the dynamical evolution of the system strongly depends on the value of the maximum density overlap, s_{max}, achieved during the first 100 fm/c.

At this stage of the dynamical evolution of the system, at the investigated energy, the quantity $\frac{s-s_{gs}}{s_{gs}}$ is relatively small ($\approx 10\% \div 15\%$), so that one can approximate $F'(\frac{s}{s_{gs}}) \approx 1+\delta \cdot \frac{s-s_{gs}}{s_{gs}}$. The form factors used in the case of Stiff1, Stiff2, and Soft iso-vector potentials correspond, respectively, to $\delta = 0.5$, $\delta = 0$ and $\delta = -0.5$. In the same limit it is easy to verify that $F'(\frac{s}{s_{gs}}) = \Phi(\gamma, \frac{s}{s_{gs}})$ with $\gamma = \delta + 1$. The best agreement between calculations and experimental results is obtained using the Stiff2 option ($\gamma = 1; \delta = 0$ case). Such calculations are reported in Figure 3.10 as hatched area histograms.

---

[1] ρ indicates the nuclear density.

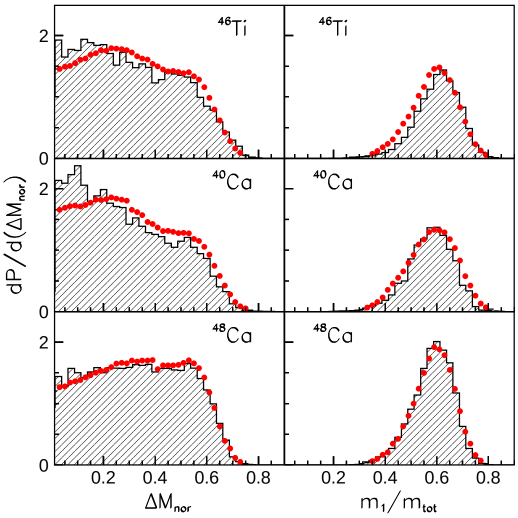

Fig. 3.10: CoMD-II + GEMINI calculations (hatched area histogram) and experimental results (dotted histograms) for the ΔM_{nor} and $\frac{m_1}{m_{tot}}$ distributions (the latter distribution is obtained with the constraint $m_2 \leq 10$). Stiff2 option has been used for the density related part of the symmetry potential.

The dynamical evolution of the system has been determined up to 600 fm/c. Secondary decays of the excited primary fragments produced at the final stage of the CoMD-II calculations are simulated with the GEMINI statistical code [20]. The ensemble of the simulated events have been finally filtered through the angular coverage and detector efficiency of Chimera. Moreover, a selection on the events reflecting the main criteria of the data analysis has been also included. We verified that all these corrections (GEMINI stage and filters) produce only second order effects and that the different behavior of the explored reactions is generated during the first stage of the collisions simulated by CoMD-II calculations. Even if some discrepancies appear, the trend of the data is satisfactorily reproduced.

In order to show the sensitivity of our simulated observables to different choices about the stiffness of the density dependence of the symmetry energy, we plot in Figure 3.11 the results obtained with ^{48}Ca target using the Stiff1, Stiff2 and Soft options. The disagreement with the data for the Stiff1 and Soft options is rather clear. In the Stiff1 and Stiff2 cases, the many-body correlations generate an attractive interaction as the nuclear density grows, inducing a higher yield of heavy residues. On the contrary, the Soft iso-vectorial potential maintains and enhances the repulsive contribution producing a fragmentation of the source. In the bottom panels in the same figure, the dashed line histograms correspond to the results obtained from CoMD-II simulations performed without the final GEMINI secondary

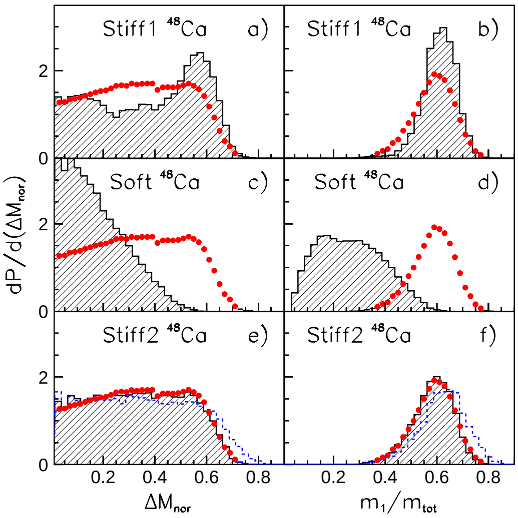

Fig. 3.11: CoMD-II + GEMINI calculations (hatched area histogram) and experimental results (dotted histograms) for the ^{48}Ca case for: a,b) Stiff1 parameterization; c,d) Soft parameterization; e,f) Stiff2 parameterization. Blue dashed histograms correspond to CoMD-II calculations without the GEMINI stage.

decays of primary excited fragments. The comparison with the shaded area histograms shows that secondary decays shift the peaks in the mass distributions to slightly lower values. However, the overall shape of these distributions remains the same. The mentioned many-body correlations [89] affect significantly the effective strength of the iso-vectorial interaction. This explains the large changes observed in the mass distributions for the three different parameterizations in Figure 3.11. According to the sensitivity shown by calculations to the different options used for the form factors describing the symmetry interaction, we can estimate that the $\gamma = 1$ value extracted from the comparison with the experimental data is affected by an error of the order of 15%. As it has been discussed above, the extracted value of the parameter can be affected by many-body correlations characterizing the CoMD-II model. On the other hand, these correlations are responsible for fragment and cluster formation processes. The role played by these many-body correlations in dynamics driven by isospin dependent forces may be better highlighted by comparing our simulations to results obtained with mean-field model approaches using the same strength and form factors.

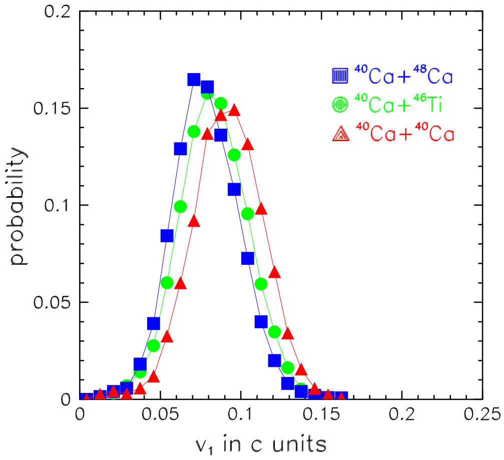

Fig. 3.12: Experimental velocity distribution for heavy residues having masses $m_1 \geq 46$ for the three reactions $^{40}Ca +^{46} Ti,^{40,48} Ca$ at 25 MeV/nucleon.

3.4 THERMODYNAMICAL ANALYSIS ON INCOMPLETE FUSION EVENTS

3.4.1 Apparent temperature measurements

In this section we analyze the thermodynamical feature of hot sources populated by means of massive transfer phenomena, where a part of the projectile fuses with the whole target. The populated systems have a considerable difference in N/Z, allowing for the search of the isospin dependence of thermodynamical parameters in quasi-fusion reactions. In order to evaluate the apparent temperature of the hot sources, we analyzed kinetic energy spectra of emitted protons. To obtain proton energy spectra belonging to fusion-evaporation, we selected those events leading to the presence, in the exit channels, of an evaporation residue having mass larger than 46 amu.

This constraint reduces the statistics of the spectra, but select clearly incomplete fusion events, where a part of the projectile fuses with the whole target (see Sect. 3.2). As a first step, we performed a two component moving source fit of spectra at different polar angles ($\theta_{lab} = 6.4, 7.8, 23, 25.5, 28.5, 34, 50°$) using two Maxwellian distributions, having the same functional form of refs. [24, 63] (see also Chapter 1). The first Maxwellian accounts for the statistical emission by the hot incomplete fusion source; the slope parameter T represents the apparent temperature (averaged upon the entire de-excitation chain) of this source. The second Maxwellian simulates the emission of protons in the dynamical stage (pre-equilibrium), where the in medium nucleon-nucleon collisions lead to the presence of fast neutrons and protons.

By looking at the mean values of velocity distributions for heavy residues, shown in Figure 3.12, we can reasonably assume a mean velocity $v^{ICF}_{^{40}Ca+^{40}Ca} =$

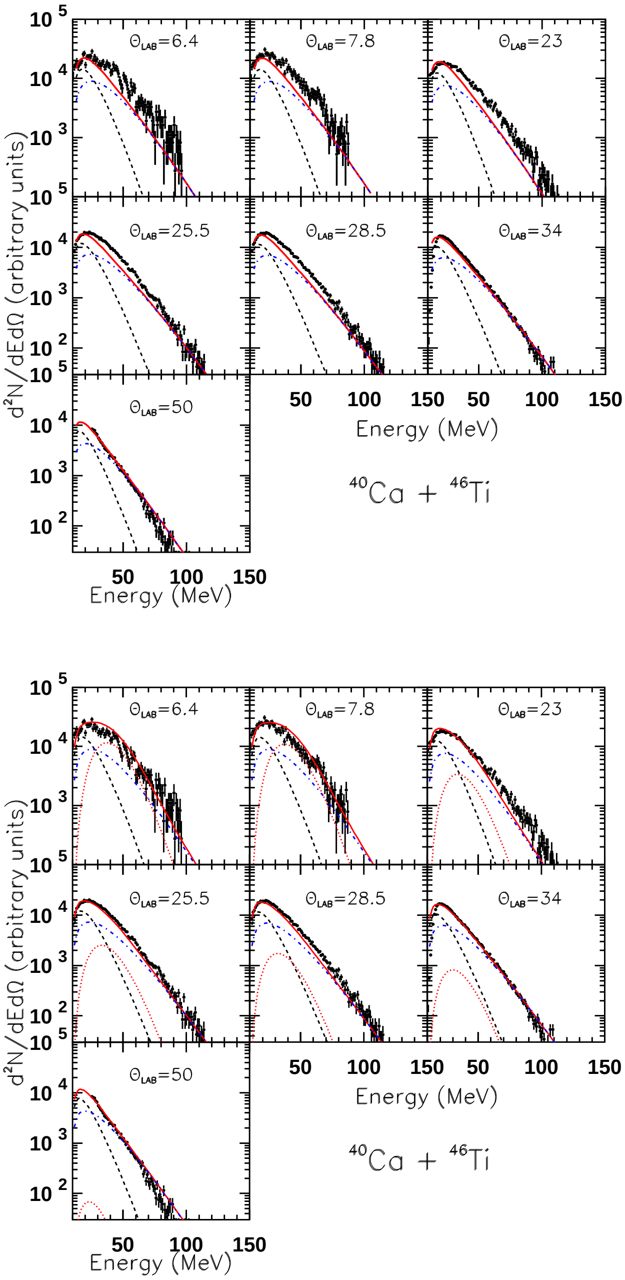

Fig. 3.13: (Upper panel) Kinetic energy spectra of protons emitted in $^{40}Ca +^{46} Ti$ reaction, under the constraint $m_1 \geq 46$. Black dashed line: incomplete fusion source. Blue dash-dotted line: pre-equilibrium contribution. Red thick line: sum of the two contributions. Circles with error bars: experimental data. (Lower panel) Quasi-projectile emission has been included (red dotted line).

$0.09c$; $v^{ICF}_{^{40}Ca+^{46}Ti} = 0.085c$; $v^{ICF}_{^{40}Ca+^{48}Ca} = 0.08c$ for incomplete fusion sources. The slight shift of the centroids can be attributed to the slight differences in reaction kinematics. Pre-equilibrium velocity is fixed very near to the half value of the beam velocity ($\simeq 0.12c$). Results of the fit procedure with two moving sources are shown in Figure 3.13 (upper panel) for the $^{40}Ca +^{46} Ti$ reaction. Similar behaviors have been observed for the other two analyzed systems. The overall agreement between the experimental data and the fit procedure is reasonable, even if at forward angles ($\theta_{lab} = 6.4 - 28^o$) the fit slightly underestimate the experimentally observed high energy proton emission. This region of the phase-space belongs mainly to quasi-projectile emission. A third maxwellian source has been included to account for the quasi-projectile emission; we fixed the temperature and velocity parameters ($T \approx 3.8$ MeV, $v \simeq 0.2c$) characterizing this emitting source. The results are shown in Figure 3.13 (lower panel); in this case a better agreement between experimental data and calculations is observed.

The average temperatures obtained for hot incomplete fusion sources from the fit analysis are similar for the three reactions. In details, we have obtained the following values of apparent temperatures: $T_{^{40}Ca+^{40}Ca} = 5.3 \pm 0.5 MeV$, $T_{^{40}Ca+^{46}Ti} = 5.2 \pm 0.3 MeV$, $T_{^{40}Ca+^{48}Ca} = 5.4 \pm 0.4 MeV$. Another observation regards the inverse slope values for pre-equilibrium emission. These values ($T \simeq 9.4 MeV$) are in agreement with systematic of data obtained in nuclear collisions at similar bombarding energies. Moreover, such values are in agreement with the slope of bremsstrahlung γ-ray emission in the same reactions at the same bombarding energies [42]. This feature, already observed in the literature [25, 36] shows that both pre-equilibrium particle emission and γ-ray bremsstrahlung emission are originated in the early phases of a nuclear reaction during nucleon-nucleon scattering process [148].

We can cross-check the estimate of apparent temperature by using another type of nuclear thermometer, based on double isotope ratios [3, 66]. In particular we used the double isotope ratios $\frac{^3He/^4He}{^6Li/^7Li}$ (labeled He-Li), $\frac{^6Li/^7Li}{^{11}C/^{12}C}$ (labeled Li-C) and $\frac{^{11}C/^{12}C}{^{12}C/^{13}C}$ (labeled C-C). To reduce contaminations due to quasi-projectile emissions we looked at isotopes detected at polar angles larger than 20°. Moreover, in order to avoid pre-equilibrium contaminations, we discarded in our computation ^3He and ^4He isotopes overcoming the energy limits of 75 and 100 MeV, respectively. Isotopes are identified by means of $\Delta E - E$ technique; for this reason their emission is partially cut due to identification thresholds. However ratios involving the yields of couples of isotopes reduce these threshold effects [149]. We verified this assumption by means of a simple simulation, supposing that the equilibrated source (at a given temperature) shows a $\frac{d^2N}{dEd\Omega}$ parameterizable as a single Maxwellian moving source. We can evaluate in this way kinematics and threshold effects for the isotopic emission. In the case of Li and C isotopes emitted at

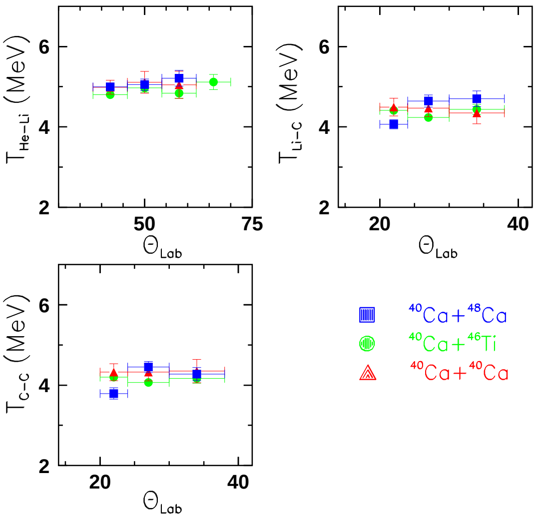

Fig. 3.14: Apparent temperatures estimated for the three studied reactions by means of double isotope ratios He-Li, Li-C, C-C, under the constraint $m_1 \geq 46$. Values of apparent temperature have been plotted as a function of the polar angle of emission of the isotopes used in double isotope ratios.

$T \approx 5MeV$ these effects are of the order of a few percent, and we do not apply correction to the experimental isotopic ratios. For the case of ^3He and ^4He, kinematic effects coupled to the presence of identification threshold modify slightly the $^3He,^4He$ emission as a function of polar angle. We obtained from calculations some corrective parameters taking into account for these effects on $^3He/^4He$ ratio. In Figure 3.14 we plot the apparent temperature values for the incomplete fusion events belonging to each reaction, as a function of polar angles in the laboratory frame.

We can observe that the estimated apparent temperatures are nearly constant as a function of the polar angle. This point indicates that there is not relevant mixing of contributions due to sources having different temperatures and moving with different velocities (for example a quasi-projectile emission mixed with incomplete fusion emission). Moreover the He-Li temperature is only slightly higher than Li-C emission, indicating that contaminations due to pre-equilibrium α particles has been avoided. For each thermometer we see that the apparent temperatures are very similar despite of the N/Z differences of the systems populated by means of incomplete fusion (the maximum temperature difference is $\approx$ 0.5MeV). In absolute values, we can see that He-Li and Li-C temperatures remain around 5-4.5 MeV for the three systems, in agreement with the temperatures evaluated by means of slope analysis. C-C temperatures are slightly lower compared to the other two thermometers ($\approx$ 4.3 MeV); this fact can be attributed both to finite-size effects for the studied systems (having relatively light masses) and to side feeding effects, as already discussed in Chapter 1 and shown in details in refs. [67, 68].

3.4.2 Excitation energy measurements

The estimate of the excitation energies achieved by central quasi-fusion sources in nuclear reactions at intermediate bombarding energies is a difficult procedure (see Chapter 1). In case of mass symmetric reactions, calorimetry is the main method to perform quantitative estimate of excitation energies.

We applied this method for very central events, leading to the presence of an heavy residue and light particles as $n, p, d, t, ^3He, ^4He$ in the exit channels. For this analysis it is mandatory to improve the completeness of the detected events. In particular we analyzed events where we detected at least 94% of the total initial charge. The used calorimetric method consisted of summing the kinetic energies (in the reference frame of emitting sources) of light charged particles evaporated by the compound nucleus, taking into account also the Q-value; obviously pre-equilibrium emission must be excluded. We assume that the emitting source velocity is given by the experimentally observed velocity vector of the detected fusion residue, i.e. we assume that during the evaporation phase, the random emission of evaporated particles does not change appreciably the velocity vector of the emitting sources. In order to evaluate pre-equilibrium emissions, we can observe the crossing point of the two moving source fits of Figure 3.13, and we assume (as an approximation) a sharp cut-off limit for the energy of the particles, beyond which the particles can be considered emitted during the pre-equilibrium stage. The masses of heavy residues are mainly detected by means of time of flight techniques. In this case the charges of these residues (useful for the Q-value calculations) are estimated by using a parametrization derived in ref. [150].

As previously reported, Chimera is not able to detect neutrons. For this reason we are forced to make some hypotheses on neutron emission. In particular, multiplicities and energies of neutrons are supposed to be similar to the proton ones for systems having $N/Z \simeq 1$ ($^{40}Ca + ^{40}Ca, ^{46}Ti$), while for the reaction $^{40}Ca + ^{48}Ca$ (N/Z=1.2) the neutron multiplicity has been supposed to be directly linked to the proton number through the N/Z of the entrance channel. By using all these ingredients it is possible to evaluate the Q-value of the reaction event by event.

In Figure 3.15 we plot the reconstructed values of the excitation energies for the selected class of central quasi-fusion events. Despite of the relatively large differences in N/Z of the populated sources, the excitation energy distributions are rather similar (within ≈ 0.3 MeV/nucleon). For the case of $^{40}Ca + ^{40}Ca$ it is possible to compare the mean value of e^* with estimations previously reported in the literature for $^{40}Ar + ^{40}Ca$ reaction at 25

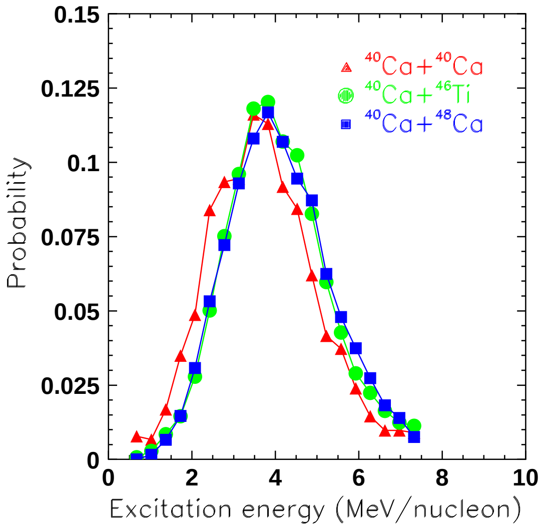

Fig. 3.15: Excitation energy (per nucleon) estimated by means of calorimetry in central quasi fusion events for all the studied reactions. The masses of the quasi-fusion sources have been estimated by summing the mass of the detected evaporation residue with the reconstructed evaporation masses.

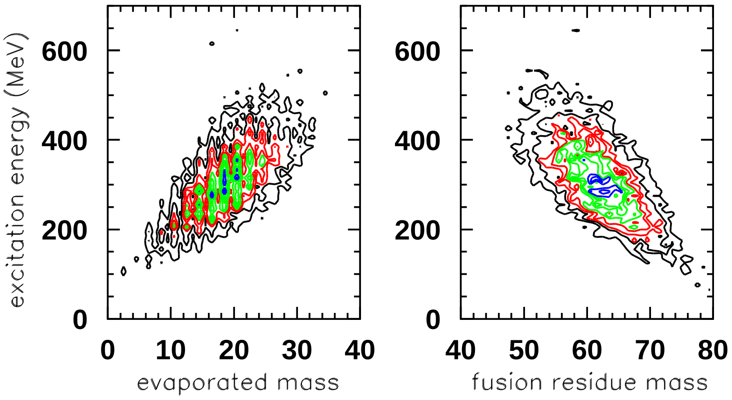

Fig. 3.16: (Left panel) Correlation between the estimated excitation energy and the evaluated evaporated mass, including neutrons. (Right panel) Correlation between the estimated excitation energy and the (detected) mass of the emitted heavy residue. Both the correlations involve central quasi-fusion events (see text for the selection criteria) for the reaction $^{40}Ca+^{46}Ti$; similar behaviors have been observed for the other two reactions.

MeV/nucleon [151]; in both cases the mean value of e^* remains close to 4 MeV/nucleon.

The excitation energy spectrum obtained for $^{40}Ca +^{40} Ca$ shows a little shift ($\approx 0.3 MeV/nucleon$) towards lower values, as compared to the other two distributions. This effect could be attributed to the different kinematics of the analyzed reactions, as observed on Figure 3.12.

In order to check the reconstruction procedure, it is useful to make a correlation plot between the evaluated excitation energy and mass related properties of quasi-fusion events. For example, we can correlate the E^* with the evaluated total evaporated mass (including estimated neutrons) or with the detected mass of the evaporation residues. Such type of correlations are shown in Figure 3.16 for the case of $^{40}Ca +^{46} Ti$ reactions. The most likely value of E^* in the case of $^{40}Ca +^{46} Ti$ reactions remains around 320 MeV (a value similar to the GDR saturation energy reported in ref. [42] and to the estimates of ref. [152] for $^{40}Ca +^{48} Ti$ system at 25 MeV/nucleon), while the total average mass of the initial excited quasi fusion source can be evaluated as the sum of the centroids of the evaporated mass distribution ($\simeq$ 17 amu) and the fusion residue mass ($\simeq$ 61 amu). In this way we obtain the most likely value of $\simeq 4MeV/nucleon$ in agreement with an event by event analysis for the excitation energy distribution in the case of $^{40}Ca+^{46}Ti$ (Figure 3.15). From the above considerations we can evaluate that about 8 nucleons are emitted in the pre-equilibrium phase (in the form of free protons and neutrons, or bound light clusters). Similar behaviors have been obtained for the other two systems.

3.5 ISOSPIN TRANSPORT IN SEMI-PERIPHERAL COLLISIONS

As it was described in Chapter 1, when nuclei having different N/Z values collide at semi-peripheral impact parameters, isospin drift and isospin diffusion phenomena can occur. It is very interesting to investigate these effects in nuclear reactions around 20 MeV/nucleon; this range of bombarding energies seems to be the best suited to see a transition from a complete charge equilibrium (a behavior typical of low energy deep-inelastic collisions) to an incomplete N/Z sharing, that would cause a non-uniform N/Z distribution through the di-nuclear system. We must underline that at 25 MeV/nucleon, as a results of the complex dynamics involved, pre-equilibrium emitted particles can also modify the N/Z distribution of intermediate di-nuclear system. To investigate these phenomena, we need to reconstruct in some way the N/Z content of quasi-projectile (QP), quasi-target (QT) and mid-velocity (MV) sources, produced in semi-peripheral events.

Experimentally, the N/Z content of QP, QT and MV sources can be probed by measuring isotopic distributions of produced fragments [99, 153, 154]. One can alternatively use the ratio between the yields of isobar nuclei

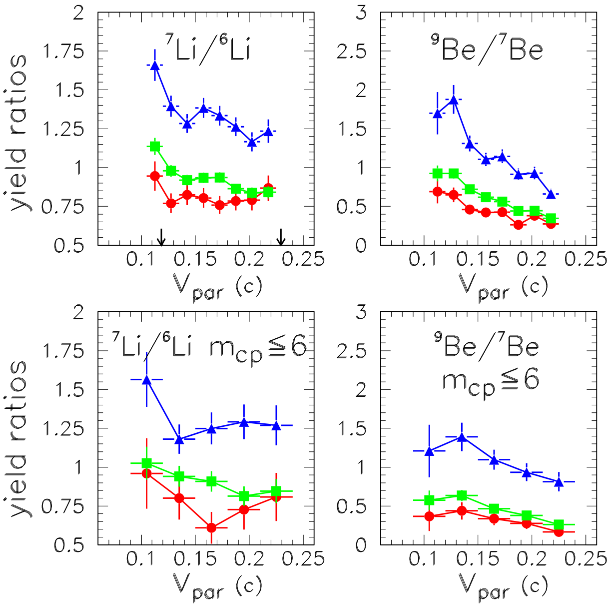

Fig. 3.17: (Upper panel) $^7Li/^6Li$ (left) and $^9Be/^7Be$ (right) isotope yield ratios as a function of the longitudinal velocity in the laboratory frame without any gate on the impact parameter. (Lower panel) Same distributions obtained in semi-peripheral events ($m_{cp} \leq 6$). Blue triangles: $^{40}Ca +^{48} Ca$ reaction. Green squares: $^{40}Ca +^{46} Ti$ reaction. Red circles: $^{40}Ca +^{40} Ca$ reaction. The arrows on the upper left panel indicate projectile velocity and half of projectile velocity.

such as $Y(n)/Y(p)$, $Y(^3H)/Y(^3He)$, $Y(^7Li)/Y(^7Be)$ and $Y(^{11}B)/Y(^{11}C)$. These approaches are based on the assumption that these isobaric ratios reflect the initial neutron/proton composition (N/Z) of their emitting sources [98, 154]. The use of these yield ratio observables allows one to infer the N/Z of primary emitting sources with reduced contaminations from secondary decays [155].

In this paragraph we will investigate isospin transport phenomena by looking at the production of isotopes ($^{6,7}Li$ and $^{7,9}Be$) and isobars (^7Li and ^7Be) in $^{40}Ca +^{40,48} Ca,^{46} Ti$ collisions at 25 MeV/nucleon. The obtained results seem to confirm the presence of isospin drift and diffusion.

3.5.1 Isotopic emission

Isospin effects can be investigated by measuring the ratio between the yields of a pair of isotopes as a function of their parallel velocity [153, 156]. This is shown on Figure 3.17 for $^6Li/^7Li$ and $^7Be/^9Be$ yield ratios. In the upper panel of Figure 3.17 we show inclusive results, while the lower panel shows the results obtained in events selected with charged particle multiplicities $m_{cp} \leq 6$. We can consider m_{cp} roughly as an impact parameter selector, as it was suggested in [144] and discussed in Sect. 3.2.3. In this case the used gate on m_{cp} selects mostly semi-peripheral collision events. Even if the absolute values of isotopic ratios are slightly smaller than those of the inclusive case (especially for Be isotopes), the trends are similar.

Isotopic ratios for fragments emitted with longitudinal velocities near to the projectile one ($v_{par} \approx 0.2c$) in different reaction systems are noticeably different. The interest of this observation relies on the fact that the projectile nucleus used in all the three reactions was the same (^{40}Ca) with $N/Z = 1$. Indeed, this effect seems to be directly related to the N/Z of the different used *targets*. We observe in the region of $v_{par} \approx v_{par}^{proj}$ an enhancement in the emission of neutron rich isotopes for the reaction involving the *target* with larger neutron excess ($^{48}Ca, N/Z = 1.4$) as compared to the other two targets (^{40}Ca and ^{46}Ti, having respectively $N/Z = 1$ and $N/Z = 1.09$). This effect is probably due to the fact that it is possible, in semi-peripheral reactions, to observe isospin diffusion effects especially for the reaction involving projectile and target nuclei with a larger gradient in N/Z ($^{40}Ca +^{48} Ca$). This phenomenon leads to an increase of the N/Z of the QP source, that we experimentally infer by observing the increased isotopic yield ratio in the region of $v_{par} \approx v_{par}^{proj}$.

The method of isotopic yield ratios has the advantage of being established between isotopes that experience almost the same Coulomb interaction when they are emitted by a given source. However it has the disadvantage of involving isotopes, i.e. nuclei with different masses, that contribute differently to the excitation energy removal. For these reasons, and in order to have additional information about the isotopic composition of the different fragmenting sources, we studied also the yield ratios of light mirror nuclei ^7Li and ^7Be.

3.5.2 Mirror isobar yield ratios

It has been shown that a way for extracting information on the N/Z content of a given emitting source consists of measuring the yield ratios of pairs of light isobars, such as $t/^3He$ or $^7Li/^7Be$[154, 158]. Figure 3.17 shows ^7Li (left) and ^7Be (right) kinetic energy spectra (black circles with error bars) measured at polar angles $\theta = 11.5, 14.5, 18, 22, 27, 34, 42, 50, 58, 66°$ in the laboratory frame for the three studied reactions.

In order to increase the statistics we perform the data analysis on inclusive events. For geometrical reasons, the bulk of events belonging to such a class is widely dominated by semi-peripheral collisions. We performed a multi component moving source analysis [24, 63] of the energy spectra shown on Figure 3.18. In particular we fit the spectra with the overlap of three

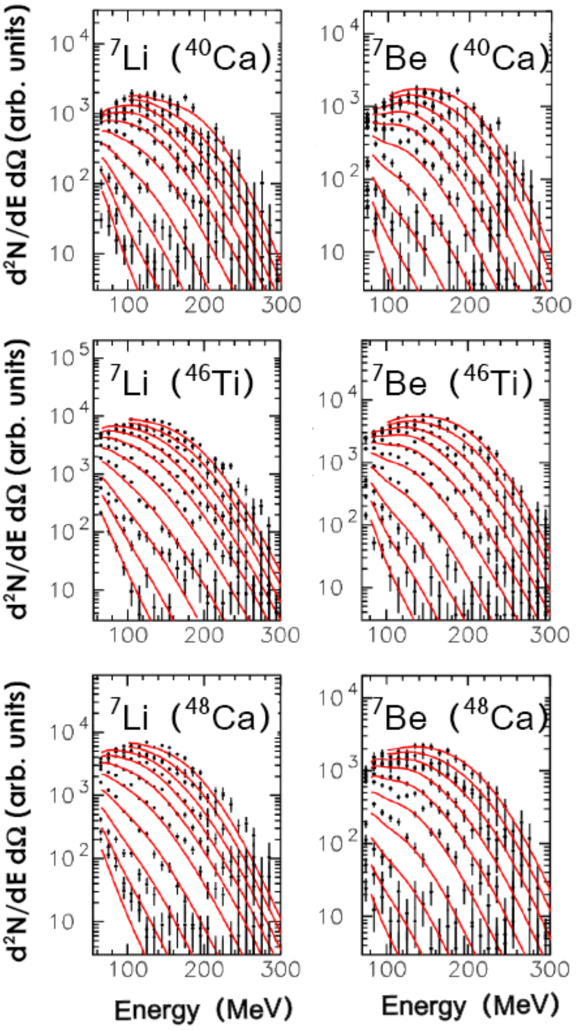

Fig. 3.18: Inclusive energy spectra ($d^2N/dEd\Omega$) of ^7Li (left) and ^7Be (right) nuclei emitted in $^{40}Ca +^{40,48} Ca,^{46} Ti$ reactions, at different polar angles ($\theta = 11.5, 14.5, 18, 22, 27, 34, 42, 50, 58, 66°$, respectively, for uppermost data points and below). The solid line represents the result of the three moving sources fits, as described in the text.

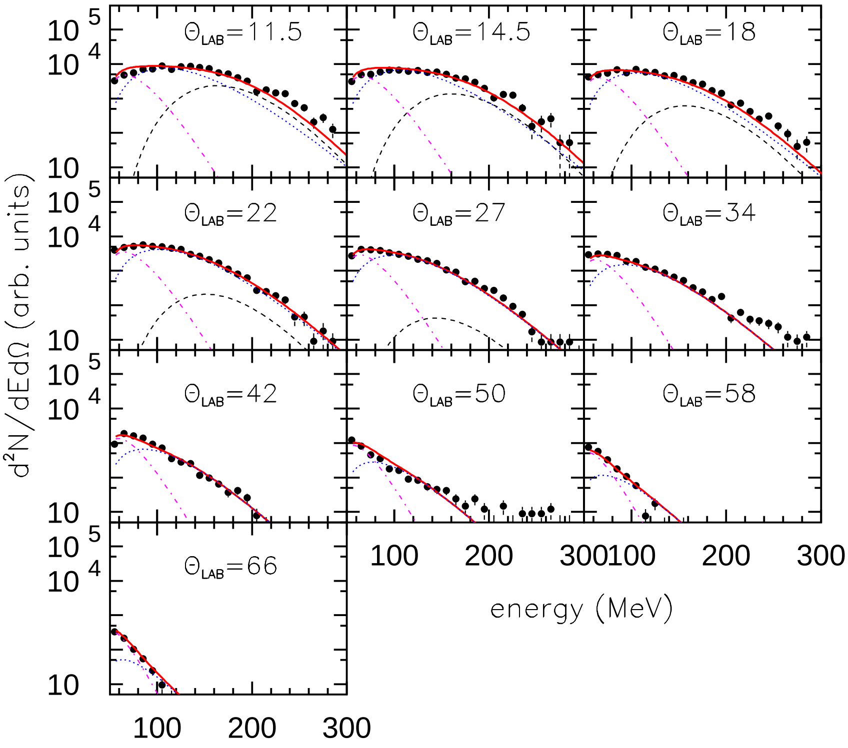

Fig. 3.19: Kinetic energy spectra of ^7Li nuclei emitted in $^{40}Ca +^{46} Ti$ reaction, at different values of polar angle in the laboratory frame (a similar behavior has been observed for the other two reactions). Black dashed line: QP emission. Violet dash-dot line: QT emission. Blue dotted line: MV emission. Red thick line: sum of the three contributions [157].

Maxwellian distributions of the form (see Sect. 1.1.2) [24, 63, 93]:

$$\frac{d^2N}{dEd\Omega} = N_i\sqrt{E-E_c}\exp[-\frac{E-E_c+E_{S,i}-2\sqrt{(E-E_c)E_{S,i}}\cos\theta}{T_i}] \quad (3.1)$$

The ith source emits at temperature T_i and moves along the beam axis with a velocity $v_{S,i}$ in the laboratory frame. In equation (3.1), $E_{S,i} = \frac{1}{2}m{v_{S,i}}^2$ is the kinetic energy of a particle moving with a velocity equal to the one of the emitting source. The normalization constants, N_i, temperatures, T_i, velocities of sources, $v_{S,i}$, and Coulomb barriers, E_c, are determined as free parameters from best-fit to the experimental data. The solid lines on Figure 3.18 show the results of the fitting procedure. The overall agreement with the measured energy spectra is satisfactory.

We also tried to fit the spectra with only two moving sources, representing the QP and MV emission (whose emitted fragments are easily detected and identified by Chimera telescopes due to kinematics). This two-component fit cannot reproduce the spectra of particles emitted at the larger polar angles ($\theta \geq 50°$). The experimental data can be reasonably well described only if a third source, corresponding to quasi-target (QT) emissions, is included in the fit procedure (see full lines on Figure 3.18).

The contributions of the QT, MV and QP Maxwellian moving sources are individually shown on Figure 3.19, for the reaction on ^{46}Ti. The obtained velocities of the three moving sources are $v_{S,i}$ =0.06c, 0.13c and 0.19c for QT, MV and QP, respectively, with uncertainties of $\simeq$ 15% due to energy calibrations and fit procedure. The value obtained for the velocity associated to QT emission is slightly higher as compared to the value expected for perfect binary kinematics ($\approx 0.04c$). These effects are probably due to identification thresholds affecting the reconstruction of QT emission. The slope parameters ($T \approx 5$ MeV) for projectile-like and target-like sources are comparable, simply reflecting the overall mass symmetry in the entrance channels of the three studied reactions. For the QT source we observe slightly larger values for the slope parameters of ^7Li as compared to ^7Be. The slope parameters obtained for the MV source are high ($T \approx 10$ MeV) in all the studied reactions. Probably this effect is due to high dissipative friction modes involving the overlap region between the colliding nuclei [1, 94]. In this scenario the MV source could be considered as an ”ancestor” of the fireball produced at mid-rapidity in heavy-ion collisions at higher beam energies ($E > 70$ MeV/nucleon) [94].

^7Li and ^7Be production cross sections, $\sigma_i(^7Li)$ and $\sigma_i(^7Be)$, for the i^{th} source can be estimated by means of the expression $\sigma_i = 2N_i(\pi T_i)^{3/2}$, with N_i and T_i deduced from the best-fit analysis shown on Figures 3.18 and 3.19 [24]. Then we calculate the isobaric ratios, $r_7 = \frac{\sigma_i(^7Li)}{\sigma_i(^7Be)}$, for each reaction and for QP and MV emitting sources. In Figure 3.20 we show the obtained

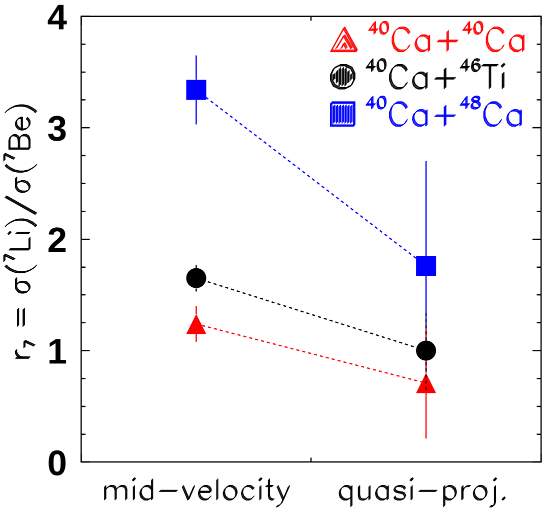

Fig. 3.20: Isobaric yield ratios $^7Li/^7Be$ for the three different reactions $^{40}Ca{+}^{40,48}Ca,^{46}Ti$ at 25 MeV/nucleon, as obtained from the moving source analysis. Reconstructed quasi-projectile (QP) and mid-velocity (MV) emissions are shown [157].

r_7 values for all the reactions (different symbols) and MV and QP emitting sources (horizontal axis).

In this figure we observe a MV emission characterized by r_7 values higher than the QP emission ones, also for the isospin symmetric reaction $^{40}Ca+^{40}Ca$. This finding is in agreement with the results shown in Sect. 3.5.1, obtained by studying the longitudinal velocity emission of light isotopes. We confirm that in the MV region neutron rich isotopes and isobars are emitted with higher probability with respect to the QP region.

By studying isobar emissions by the QP source (rightmost data points on Figure 3.20), we observe that even if the projectile used was the same for the three reactions (^{40}Ca), the r_7 values increase with the N/Z of the target nucleus. This effect, in agreement with the experimental findings of previous sections, shows that isospin diffusion takes place between projectile and target nuclei. During the collision process the two reaction partners exchange neutrons and protons. In particular, the larger is the difference in N/Z between projectile and target nuclei, and the larger is the net neutron diffusion through the di-nuclear system formed during the reaction.

We performed calculations of mid-peripheral $^{40}Ca+^{48}Ca$ collisions at 25 MeV/nucleon with CoMD-II [89, 90], BNV [86] and IBUU04 [85] codes, looking at the N/Z evolution of QP and QT sources up to the re-separation time ($\simeq 150 fm/c$). The three codes give a qualitatively similar behavior for this observable. In Figure 3.21 we show for example the results of CoMD-II

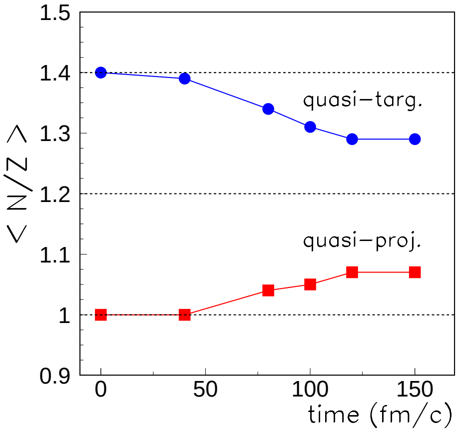

Fig. 3.21: N/Z evolution of quasi-projectile and quasi-target reaction partners as seen in CoMD-II calculations for $^{40}Ca+^{48}Ca$ at 25 MeV/nucleon at $b = 7fm$. The re-separation time of di-nuclear system is $\simeq 150 fm/c$. Blue circles: quasi-target. Red squares: quasi-projectile.

calculations at $b = 7fm$, where we used the Stiff2 option for the symmetry potential [89] (see Sect. 3.3.2). As a results of the complex dynamics involving the early stages of the collisions, the N/Z ratio of the two interacting partners changes as a function of time, trying to reach a similar intermediate value. Calculations show moreover that the complete charge equilibrium value ($N/Z = 1.2$) is not reached at the re-separation.

3.6 Conclusion

In this Chapter we reported different aspects of the study of nuclear collisions $^{40}Ca +^{40,48} Ca,^{46} Ti$ at 25 MeV/nucleon. By looking at inclusive emissions of light fragments we observed isotopic effects due to the different values of N/Z in the entrance channel. Moreover, Z- and N-distributions show clearly odd-even staggering effects that may be attributed to the last steps of the de-excitation chain of hot sources formed in heavy ion collisions. Amplitude of the staggering effect seems to be influenced by the different neutron richness of the reactions.

We explored the main scenarios involved in reaction dynamics by means of *Dalitz plots* and fragment velocity correlations. Evaporation residue emissions and binary-like phenomena dominate, as expected for these relatively light systems at 25 MeV/nucleon bombarding energies. We have seen that the N/Z degree of freedom strongly influences the competition between different reaction mechanisms in *semi-central* events. In particular, for the neutron rich $^{40}Ca +^{48} Ca$ reaction we observed an high probability of producing evaporation residues. On the contrary binary-like mechanisms prevail for the two other systems having $N \simeq Z$. This effect could be attributed to the strong interplay between the Coulomb and the symmetry terms in the nuclear equation of state. We performed CoMD-II calculations of the analyzed systems; in details, we compared experimental data and calculations related to mass distributions of the two largest fragments emitted in each event of the reaction. We used different options for the stiffness of the density dependent part of the symmetry term. The best agreement between calculations and experimental data is obtained by using $\gamma = 1 \pm 0.15$, i.e. an asy-stiff option (see Chapter 1).

We analyzed thermometric and calorimetric properties of hot sources populated in incomplete fusion events. Apparent temperatures of these sources have been estimated by means of different nuclear thermometers. The first one was based on the slope analysis of kinetic energy spectra of protons. The second thermometric method was based on double isotope ratios. The different thermometers provide consistent results. For central quasi-complete fusion events, a calorimetric evaluation of the excitation energy reached by the quasi-fusion source has been performed. Despite of the differences in the N/Z of the entrance channels, apparent temperatures and excitation energies reached by hot sources populated in the three studied reactions are similar. Therefore, in central collisions, the N/Z degree of freedom plays a strong role in the *dynamics* of reaction, while it has only a weak influence on the *thermodynamic parameters* characterizing hot sources formed in the first phase of the collision.

In *semi-peripheral* events, isospin transport phenomena have been investigated by studying the emission of light isotopes (^{6,7}Li, ^{7,9}Be) and isobars (^{7}Li and ^{7}Be). A neutron enrichment of nuclear clusters emitted at mid-velocity is observed by studying isobaric yield ratios. Especially the observed neutron enrichment at mid-rapidity in the case of a N/Z-symmetric reaction (^{40}Ca+^{40}Ca) may be explained as being solely due to the effect of isospin drifting along the low density neck region. In the case of ^{40}Ca+^{48}Ca N/Z-asymmetric reactions, isobaric and isotopic yield ratios show that a net diffusion of neutrons from the neutron rich target ^{48}Ca to the ^{40}Ca projectile has occurred as a consequence of isospin diffusion effects between the interacting nuclear systems.

Chapter 4

N/Z effects on the n-rich ^{48}Ca+^{48}Ca system

In order to deeper investigate N/Z effects on nuclear dynamics (especially at semi-central impact parameters), we studied the reaction $^{48}Ca +^{48} Ca$ at 25 MeV/nucleon [159]. This system has an N/Z value of the entrance channel equal to 1.4, one of the highest values obtainable with medium mass stable beams and targets. Data reduction, involving energy calibrations, $\Delta E - E$ identification, fast-slow analysis and time of flight identification has been performed in a quite short time, due also to improvements of the software dedicated to identification procedures [161]. First results, concerning the emission of evaporation residues in incomplete fusion events, will be discussed. From the data analysis, the key role played by the N/Z of the entrance channels on the interplay between evaporation residue emission and binary-like events is further explored.

4.1 Experimental Details

The experiment ("*isospin-I*") was performed at INFN-LNS Cyclotron in June 2009. A ^{48}Ca beam at 25 MeV/nucleon with an intensity of $\approx 400pA$ impinged on self-supporting, isotopically enriched targets of ^{48}Ca (thickness 2.75 mg/cm^2). Time resolution achieved by the Chimera detectors was $\approx 800ps$ FWHM. A mass resolution of about $\approx 5\%$ was obtained (see Chapter 3). Analogously to previously described analyses, we selected and investigated almost complete events by means of the same constraints on the detected total charge Z_{tot} and total momentum $\overrightarrow{p_{tot}}$. Dedicated energy calibrations were performed at the beginning of the experiment; four elastic scattering point of ^{12}C and ^{16}O were used (see also Chapter 2). The on line trigger required that at least 3 silicon detectors were fired by charged particles.

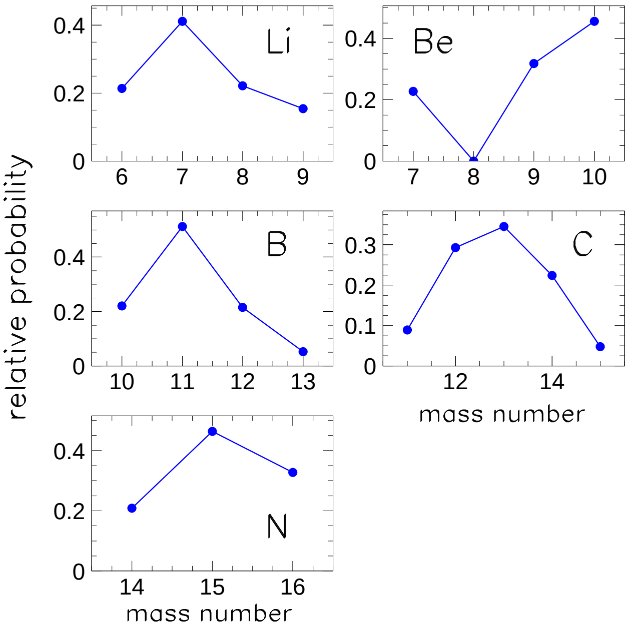

Fig. 4.1: Mass distributions of light isotopes emitted at forward polar angles ($5.2° < \theta < 15.3°$) in $^{48}Ca +^{48} Ca$ reaction at 25 MeV/nucleon. Isotopic identification has been obtained by using $\Delta E - E$ technique (see Chapter 2). Error bars are smaller than dots.

4.2 Isotopic emission

We first investigated inclusive emission of light isotopes at forward angles. In Figure 4.1 we plot isotopic distribution of light nuclei (from Lithium to Nitrogen) emitted in the range of polar angles (in laboratory frame) $5.2° < \theta < 15.3°$. As expected for neutron rich systems, the isotopic distribution are pushed towards the neutron rich side. Particularly interesting are the cases of Beryllium and Carbon distributions. An abundant emission of $^{9,10}Be$ is seen and ^{13}C is the most populated Carbon isotope.

We also studied charge distributions of light fragments emitted at forward angles ($\theta = 11.5°$). In Figure 4.2 we plot the results obtained in the $^{48}Ca +^{48} Ca$ reaction, together with the results of the *limiting* experiment (see Figure 3.2). Structure effects are present in charge distributions, leading to the depletion of boron and fluorine emission, as already discussed in Chapter 3.

We can also observe that the amplitude of even-odd oscillations characterizing the charge distributions (Sect. 3.2) are more and more damped when the N/Z of entrance channels increases. On the contrary, when we look at the yields of fragments emitted as a function of their neutron content (Fig-

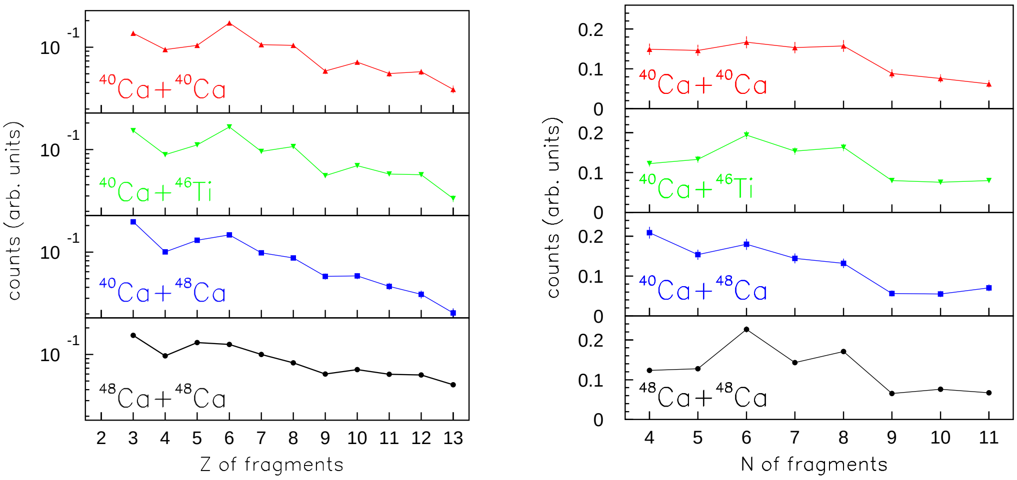

Fig. 4.2: (Left panel) Charge distributions of light fragments emitted at forward angles ($\theta = 11.5°$) in $^{40}Ca + ^{40}Ca$ (red triangles), $^{40}Ca + ^{46}Ti$ (green triangles), $^{40}Ca + ^{48}Ca$ (blue squares) and $^{48}Ca + ^{48}Ca$ (black circles) reactions at 25 MeV/nucleon [160]. (Right panel) The same for neutron distributions.

ure 4.2, right panel), the amplitude of staggering increases by increasing the N/Z of the entrance channel.

These effects can be qualitatively interpreted by considering that, in neutron rich nuclear reactions, light clusters with an excess of neutrons are more likely to be emitted, while in neutron poor reactions, neutron poor fragments are more easily produced. Trying to reach the stability valley, neutron rich excited fragments will de-excite mainly by emitting neutrons, while neutron poor ones will de-excite mainly by emitting protons. For this reason, in *neutron poor* systems (i.e., for example, $^{40}Ca + ^{40}Ca$), the de-excitation cascades involving excited fragments will be dominated by proton evaporation; in this way the final *charge* distribution of light fragments emitted will reflect strongly even-odd oscillations characterizing *one-proton* separation energy distributions of light nuclei near the stability valley. Symmetrically, for neutron rich systems (i.e., for example, $^{48}Ca + ^{48}Ca$), the de-excitation cascade will involve mainly neutron emission; in such a way, the final *neutron* distribution of light fragments will be strongly related to even-odd oscillations characterizing *one-neutron* separation energy distributions.

Quantitative predictions can be obtained with dynamical calculations followed by accurate statistical treatment of excited nuclei. Such analysis goes beyond the aim of the present work.

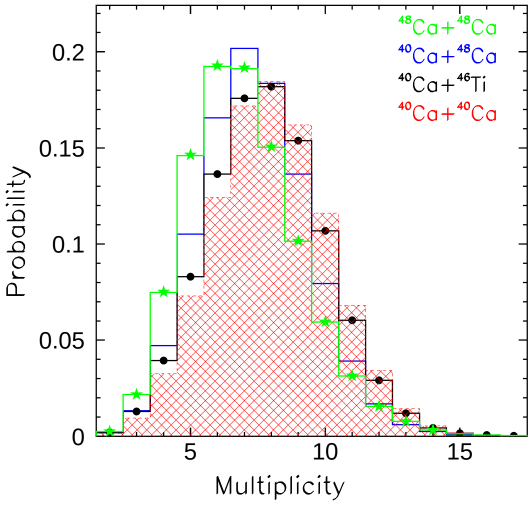

Fig. 4.3: Charged particles multiplicity observed in the four studied systems $^{40}Ca +^{40} Ca$ (red shaded area histogram), $^{40}Ca +^{46} Ti$ (black circles), $^{40}Ca +^{48} Ca$ (blue histogram) and $^{48}Ca +^{48} Ca$ (green stars) at 25 MeV/nucleon. See also [145, 146, 147]

4.3 Incomplete fusion events

The multiplicity of charged particles (m_{cp}) observed in the reaction ^{48}Ca+^{48}Ca is shown in Figure 4.3 together with those measured in the *limiting* experiment. The global behavior of m_{cp} is similar for the four studied reactions, even if the m_{cp} distributions are slightly shifted towards lower values at increasing N/Z of the entrance channel. As already discussed in Chapter 3, this effect could be attributed to the larger probability of emitting neutrons (that are undetected) in neutron-rich systems [145, 146].

As previously observed in the *limiting* experiment (Chapter 3), the competition between evaporation residues production and binary-like mechanisms (that dominates semi-central events of reactions at 20-30 MeV/nucleon bombarding energies, for medium mass systems) can give useful information about the interplay of the Coulomb and Symmetry term in the Equation of State of nuclear matter [145]. We have now the possibility to extend the previous results to the very neutron rich system $^{48}Ca +^{48} Ca$.

In order to verify that the detector response was the same for the two analyzed experiments (*limiting* and *isospin-I*), we studied, during the *isospin-I* experiment, also the reaction $^{48}Ca +^{40} Ca$ at 25 MeV/nucleon. This system is (apart from slight difference in kinematics) equivalent to the $^{40}Ca +^{48} Ca$ one performed in the *limiting* experiment. Therefore, we cross-checked the behavior of many observables related to the two reactions $^{48}Ca +^{40} Ca$

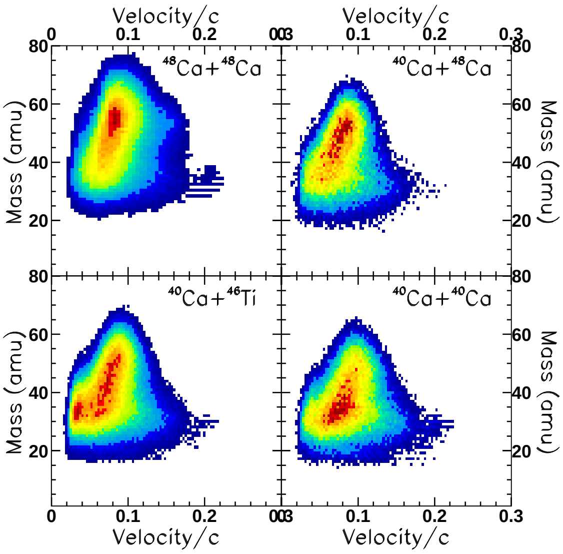

Fig. 4.4: Mass-velocity correlations (m_1, v_1) of the largest fragment emitted in semi-central incomplete fusion events of reactions $^{40}Ca+^{40}Ca$, $^{40}Ca+^{46}Ti$, $^{40}Ca+^{48}Ca$ and $^{48}Ca+^{48}Ca$ at 25 MeV/nucleon.

(*isospin-I*) and $^{40}Ca+^{48}Ca$ (*limiting*). Very similar results were obtained, confirming that detector response was the same for the two experiments.

Analogously to the *limiting* case, we selected incomplete fusion events by looking at semi-central events ($m_{cp} \geq 5$) where the second or third largest fragment emitted was a projectile remnant (having a velocity larger than 0.13c) [145, 146, 147]. With these constraints, we plot on Figure 4.4 the correlation of mass (m_1) and velocity (v_1) of the largest fragment emitted in all reaction systems studied in the performed experiments.

Even if the overall shapes of the correlations are similar, the enhanced emission of evaporation residues in incomplete fusion events of the $^{48}Ca+^{48}Ca$ reaction is quite evident. This finding confirms strongly the conclusions of Chapter 3 and enlightened in refs. [145, 146]: the balance between production of evaporation residues and binary-like mechanisms is strongly affected by the N/Z degree of freedom; in particular, nuclear reactions characterized by a high N/Z value at the entrance channels show a larger probability of producing evaporation residues by means of incomplete fusion [145]. This effect can be enlightened also by looking at mass distributions of the largest fragment emitted in the selected incomplete fusion events, by putting a gate on velocity in order to exclude target-like or projectile-like contaminations ($0.04 < \frac{v_1}{c} < 0.15$) [145]. Figure 4.5 shows mass distributions obtained for the systems analyzed in the *limiting* and *isospin-I* experiments involving Ca isotopes as beams and targets. We underline that our data refer to a very wide range of N/Z spanned by the studied systems (going from N/Z=1

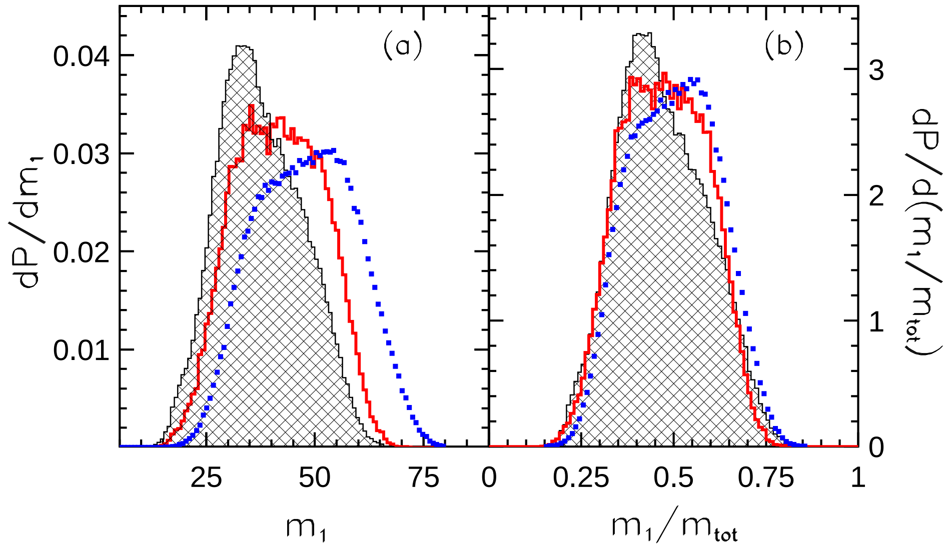

Fig. 4.5: (a) Mass distribution of the largest fragment emitted in semi-central incomplete fusion events (see text). To remove quasi-projectile and quasi-target contaminations, a further constraint on v_1 is imposed: $0.04 < \frac{v_1}{c} < 0.15$. Black shaded histogram: $^{40}Ca +^{40} Ca$. Red solid histogram: $^{40}Ca +^{48} Ca$. Blue dots: $^{48}Ca +^{48} Ca$. (b) Distributions of normalized mass m_1/m_{tot} of the largest fragment emitted in the studied collisions, for the same class of events. In both panels, y-axis have been normalized to the total number of counts and to the width of the bins.

for the $^{40}Ca +^{40} Ca$ reactions of the *limiting* experiment up to N/Z=1.4 for the $^{48}Ca +^{48} Ca$ reactions of the *isospin-I* experiment). Apart from obvious effects due to the different masses of the entrance channels (Figure 4.5, left panel) that can be well reduced by normalizing m_1 to the total mass of the systems m_{tot} (Figure 4.5, right panel), a surprisingly different behavior is observed. Evaporation residues ($m_1 \gtrsim 50$) are emitted with larger probability in neutron rich system $^{48}Ca +^{48} Ca$, while binary-like events prevail in $N = Z$ system $^{40}Ca +^{40} Ca$.

We are able to extract the yields of binary-like (σ_{BL}) and evaporation residues emissions (σ_{ER}) by fitting m_1 distributions with two gaussian. Results of best fits are shown in Figure 4.6, for the four studied systems involving only Ca isotopes. As a cross-check, we also included the distributions obtained from $^{48}Ca +^{40} Ca$ reactions (*isospin-I* experiment); it is quite similar to the $^{40}Ca +^{48} Ca$ reaction case. It appears clearly that, by increasing the neutron richness of the entrance channels, the production of evaporation residues increases to the expenses of binary-like emission. In Figure 4.6(e) we plot the ratio between evaporation residue and binary-like yields (σ_{ER}/σ_{BL})

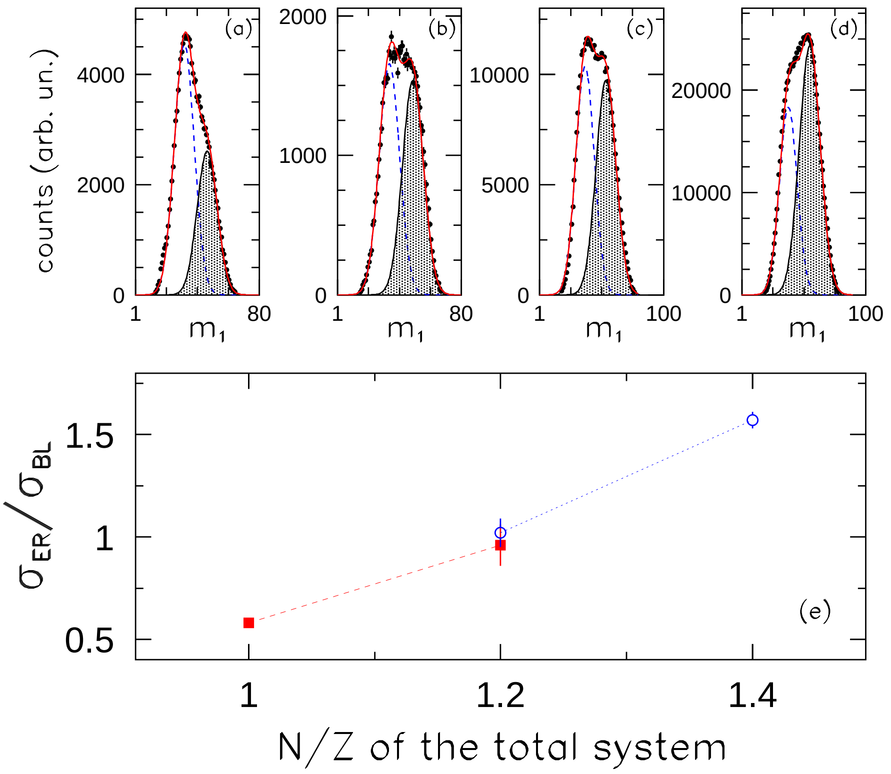

Fig. 4.6: (a,b,c,d) Mass distributions of the largest fragment emitted in reactions involving Ca isotopes. Black dots: experimental data. Red solid line: two gaussians fit. Blue dashed line: binary-like contribute. Shaded gaussian: evaporation residue emission. (a) $^{40}Ca+^{40}Ca$ (b) $^{40}Ca+^{48}Ca$ (c) $^{48}Ca+^{40}Ca$ (d) $^{48}Ca+^{48}Ca$. (e) σ_{ER}/σ_{BL} obtained from the fit procedure, as a function of N/Z of the entrance channels. Red squares: *limiting* experiment. Open blue circles: *isospin-I* experiment.

obtained from the fit as a function of N/Z of the entrance channels. A strong correlation is observed. In particular, σ_{ER}/σ_{BL} in the case of neutron rich $^{48}Ca+^{48}Ca$ reaction is about three times larger than $^{40}Ca+^{40}Ca$ reaction. The points obtained for the mixed systems $^{40}Ca+^{48}Ca$ and $^{48}Ca+^{40}Ca$ (N/Z=1.2) are very close, and they remain at intermediate values as compared to the N/Z=1.0 and N/Z=1.4 cases. These findings strongly confirm the fundamental role played by the N/Z degree of freedom on the emission of evaporation residues by hot nuclear systems populated near the fragmentation threshold.

4.4 CoMD-II model calculations

As already discussed in Sect. 3.3.2, we were able to extract information about the poorly known behavior of the symmetry potential by comparting experimental mass distributions typical of incomplete fusion phenomena with dynamical calculations. In particular, we compared our experimental data with CoMD-II model calculations and we argued that a Stiff2 option ($\gamma = 1.0$) must be used in order to reproduce experimental distributions. Calculations show sensitivity to the different options characterizing the symmetry potential: Stiff1 ($\gamma = 1.5$) and Soft ($\gamma = 0.5$) parameterizations disagree clearly with experimental data.

With *isospin-I* experiment, we had the opportunity to enlarge the systematic to the very neutron-rich reaction $^{48}Ca +^{48} Ca$. Therefore, we performed calculations with the CoMD-II model for this neutron-rich system, by using again the three different options for the stiffness of symmetry potential (Stiff1, Stiff2 and Soft parameterizations used in Sect. 3.3.2). The dynamical evolution was followed by CoMD-II model up to 600 fm/c. Secondary decays of excited fragments have been simulated by using the GEMINI code. Calculations have been finally filtered through the angular coverage and detection efficiency of the Chimera array. The same constraints applied to experimental data have been applied to calculations, i.e. a selection of charged particle multiplicity and of velocities of the second and third largest emitted fragments. The same gate $0.04 < \frac{v_1}{c} < 0.15$ was also used to discard quasi-projectile and quasi-target contaminations.

On Figure 4.7 we show experimental m_1/m_{tot} and ΔM_{nor} distributions, obtained for the $^{48}Ca +^{48} Ca$ system, together with preliminary CoMD-II calculations obtained by using the three different options for the stiffness of symmetry potential. Experimental data and calculations agree nicely when a Stiff2 option ($\gamma = 1.0$) is used, while the disagreement between data and calculations performed with Stiff1 and Soft options is evident. This finding strongly confirms our previous estimate of the degree of stiffness of the symmetry potential. Driven by these results, we are stimulated to continue the investigation of dynamics of semi-central collisions near 25 MeV/nucleon also by using proton rich and neutron rich radioactive beams, enlarging the available range of N/Z of entrance channels. In this way, we will be able to evaluate with increasing precision the value of γ parameter characterizing the behavior of symmetry potential at sub-saturation densities.

4.5 Conclusions

The fate of hot nuclear sources populated in semi-central incomplete fusion events of reaction involving different isotopes of Calcium at 25 MeV/nucleon bombarding energy was investigated. Two main reaction paths were rec-

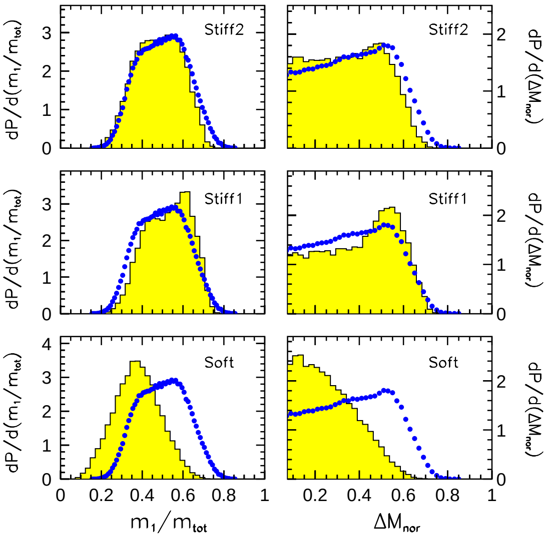

Fig. 4.7: CoMD-II + GEMINI calculations (yellow area histogram) and experimental data (blue dots) of the $^{48}Ca+^{48}Ca$ reaction at 25 MeV/nucleon. Semi-central collisions have been selected as described in the text. Stiff2, Stiff1 and Soft parameterizations have been used in the model calculations to describe the behavior of symmetry potential.

ognized: the production of evaporation residues and binary-like emission. The balance between these two paths is strongly affected by the N/Z of the entrance channel. Quantitative estimates of evaporation residues versus binary-like emissions as a function of N/Z of total systems testify the strong role played by the neutron excess in fusion dynamics at excitation energies near to the limits of existence of bound nuclear systems. In agreement with results of *limiting* experiment, comparisons to CoMD-II model calculations confirm strongly that a stiff dependence of the symmetry potential (with $\gamma = 1.0$) must be used to reproduce the experimental data. All these findings open the way for further investigations to be performed with proton and neutron rich radioactive beams [123].

Summary

> *Somnia ne cures, nam mens humana quod optat, dum vigilat sperat, per somnum cernit id ipsum.* (M. Porzio Catone)

In this Ph.D. thesis I discussed experimental results concerning the reactions $^{40}Ca+^{40,48}Ca,^{46}Ti$ (*limiting* experiment) and $^{48}Ca+^{40,48}Ca$ (*isospin-I* experiment) at 25 MeV/nucleon bombarding energy, i.e. near the fragmentation threshold. The experiments have been performed at INFN-LNS Super-Conducting Cyclotron facility and have been studied by using the 4π Chimera array as multi-detector device. The populated systems have large differences in the N/Z of the entrance channels. For this reason, I had the opportunity to disentangle isospin effects in central and mid-peripheral collisions. The main conclusions of my work can be summarized as it follows.

Strong isotopic effects have been observed by looking at inclusive emission of light fragments. Charge and neutrons distributions of light fragments emitted at forward angles show odd-even oscillations that may be attributed to the last steps of the de-excitation chain of hot sources formed in the first phase of the collisions. The N/Z of the entrance channel seems to play a role on the amplitude of the staggering effect of charge and neutron distributions.

By studying *mid-peripheral* collisions, isospin transport phenomena have been investigated. The emission of light isotopes (^{6,7}Li, ^{7,9}Be) and isobars (^{7}Li and ^{7}Be) from quasi-projectile and mid-velocity sources was studied. A neutron enrichment of nuclear clusters emitted at mid-velocity was found. The neutron enrichment seen at mid-rapidity in the case of a N/Z symmetric reaction (^{40}Ca+^{40}Ca) can be explained as due purely to isospin drift phenomena.

In the case of ^{40}Ca+^{48}Ca N/Z-asymmetric reactions, isobaric and isotopic yield ratios show that a net diffusion of neutrons from the neutron rich target ^{48}Ca to the ^{40}Ca projectile has occurred as a consequence of isospin diffusion effects between the interacting nuclear systems.

Detailed investigations of the behavior of *central* collisions have been also performed. I found that the N/Z degree of freedom strongly influences the competition between different reaction mechanisms (emission of evaporation residues *versus* binary-like phenomena). For the very neutron rich $^{48}Ca +^{48} Ca$ system (N/Z=1.4) an high probability of emitting evaporation residues was observed. At variance, binary-like mechanisms prevail for systems having $N \simeq Z$ (i.e, $^{40}Ca +^{40} Ca$ and $^{40}Ca +^{46} Ti$). An intermediate behavior is observed for the mixed systems $^{40}Ca +^{48} Ca$ and $^{48}Ca +^{40} Ca$ (N/Z=1.2). This effect can be attributed to the interplay between the Coulomb and the symmetry term in the nuclear equation of state. These findings confirm strongly the fundamental role played by the N/Z degree of freedom on the production of evaporation residues by hot nuclear systems populated near the fragmentation threshold.

Experimental mass distributions of the two largest fragments emitted in each reaction event have been compared with Constrained Molecular Dynamics (CoMD-II) calculations. Different options for the stiffness of the density dependent part of the symmetry term have been used. The best agreement between calculations and experimental data (obtained from *limiting* and *isospin-I* experiments) is obtained by using $\gamma = 1$, i.e. an asy-stiff option.

Thermometric and calorimetric analyses of hot sources populated in incomplete fusion events have been performed. Apparent temperatures have been estimated by using two nuclear thermometers. The first one was based on the slope of kinetic energy spectra of protons. The second was based on double isotope ratios. The two thermometers give consistent results. For central quasi-complete fusion events, I evaluated also the excitation energy of quasi-fusion sources. Despite of differences in the N/Z of the entrance channels, apparent temperatures and excitation energies are quite similar.

An analysis of central collisions suggests therefore that the N/Z degree of freedom plays a strong role in the *dynamics* of the reaction, while it has a weak influence on the *thermodynamical parameters* characterizing hot sources formed in the first phase of collision.

These conclusions open the way for further investigations with unstable beams. As a physics case, we plan to perform $^{34}Ar +^{40} Ca$ collision at 25 MeV/nucleon, at FRIBs facility of INFN-LNS in Catania. According to our systematics, we may expect for this proton rich system an enhancement of binary-like emission and a consequent suppression of evaporation residues production. In view of this future project, I have built a large surface microchannel plate that will give the start reference time to improve time of flight measurements.

Bibliography

[1] D. A. Bromley, *Treatise on Heavy Ion Science*, (Plenum Press NY, 1984), Vols. 1-8

[2] H. Morgenstern et al, Phys. Rev. Lett. **52** (1984) 1104

[3] J. Pochodzalla et al, Phys Rev. Lett. **75** (1995) 1040

[4] C. Ngo and C. Le Sech, *Physique Nucleaire*, (Dunod Paris 2010)

[5] A. Sandorfi, in *Treatise on Heavy Ion Science*, (Plenum Press NY, 1984), Vol. 2

[6] H. Lehr et al, Nucl. Phys. **A 415** (1984) 149

[7] R. Bass, Phys Rev. Lett. **39** (1977) 265

[8] N. Arena et al, Phys. Rev. **C 44** (1991) 1947

[9] H. Morgenstern et al, Phys. Lett. **B 113** (1982) 463

[10] C. Ngo and S. Leray, Prog. Part. Nucl. Phys. **15** (1985) 163

[11] H.C. Britt and A.R. Quinton, Phys. Rev. **124** (1961) 877

[12] T. Inamura et al, Phys. Lett. **B 68** (1977) 51

[13] H.-J. Keim et al, Zeit. Phys. **A 327** (1987) 101

[14] F.W. Prosser et al, Phys. Rev. **C 40** (1989) 2600

[15] C. Beck et al, Phys. Rev. **C 39** (1989) 2202

[16] M. Gonin et al, Phys. Rev. **C 38** (1988) 135

[17] C. Cerruti et al, Nucl. Phys. **A 492** (1989) 322

[18] K. Hagel et al, Phys. Rev. **C 50** (1994) 2017

[19] J. Aichelin et al, Phys. Lett. **B 224** (1989) 34

[20] R. J. Charity et al, Nucl. Phys. **A 483** (1988) 371

[21] B. Borderie and M.F. Rivet, Prog. Part. Nucl. Phys. **61** (2008) 551

[22] P. Lautesse et al, Eur. Phys. Jour. **A 27** (2006) 349

[23] L. Shvedov, M. Colonna and M. di Toro, Phys. Rev. **C 81** (2010) 054605

[24] T. C. Awes et al, Phys. Rev. **C 25** (1982) 2361

[25] D. Pierroutsakou et al, Phys. Rev. **C 80** (2009) 024612

[26] D. Mahboub et al, Phys. Rev. **C 69** (2004) 034616

[27] G. Nebbia et al, Phys. Rev. **C 45** (1992) 317

[28] H. Yamada et al, Phys Rev. Lett. **43** (1979) 605

[29] L. Pienkowski et al, Zeit. Phys. **A 334** (1989) 315

[30] P.L. Gonthier et al, Nucl. Phys. **A 411** (1983) 289

[31] R. Alba et al, Phys. Lett. **B 322** (1994) 28

[32] R. Coniglione et al, Phys. Lett. **B 471** (2000) 339

[33] D. Doré et al, Phys. Lett. **B 491** (2000) 15

[34] H. Fuchs and K. Möhring, Rep. Prog. Phys. **57** (1994) 231

[35] K. Hagel et al, Phys. Rev. **C 62**(2000) 034607

[36] D. Santonocito et al, Phys. Rev. **C 66** (2002) 044619

[37] K. Mukhin, *Experimental Nuclear Physics*, (MIR, 1988), Vol. 1

[38] A. Bracco et al, Phys Rev. Lett. **74** (1995) 3748

[39] M. Papa et al, Phys. Rev. **C 68** (2003) 034606

[40] A. Musumarra et al, Nucl. Instrum. Meth. Phys. Res. **A 370** (1996) 558

[41] F. Puhlofer, Nucl. Phys. **A 280** (1970) 267

[42] F. Amorini et al, Phys. Rev. **C 69** (2004) 014608

[43] W. Greiner and J. Marhun, *Nuclear Models*, (Springer, 2004)

[44] D. Santonocito and Y. Blumenfeld, Eur. Phys. Jour. **A 30** (2006)

[45] P.F. Bortignon et al, Phys Rev. Lett. **67** (1991) 3360

[46] M. Alonso and E.J. Finn, *Fundamental University Physics*, (Addison-Wesley, MA 1996)

[47] K. Huang, *Statistical Mechanics*, (Wiley, NY 1987)

[48] D. Griffiths, *Introduction to Quantum Mechanics*, (Pearson, 2005)

[49] E. Suraud et al, Nucl. Phys. **A 462** (1987) 109

[50] E. Segré, *Nuclei e Particelle*, (Zanichelli, Bologna 1988)

[51] W. Noremberg and H. Weidenmuller, *Introduction to the Theory of Heavy Ion Collisions*, (Springer 1980)

[52] W. Blatt and W. Weisskopf, *Theoretical Nuclear Physics*, (Wiley, 1952)

[53] B. Povh et al, *Particles and Nuclei*, (Springer 1999)

[54] J. Natowitz et al, Phys. Rev. **C 65** (2002) 034618

[55] A. Kelic et al, Eur. Phys. Jour. **A 30** (2006)

[56] D. Durand et al, *Nuclear Reactions in the nucleonic regime*, (IOP 2000)

[57] S. Leray, Jour. Phys. **47** (1986) C4-275

[58] S. Levit and P. Bonche, Nucl. Phys. **A 437** (1985) 426

[59] J. Besprosvany and S. Levit, Phys. Lett. **B 217** (1989) 1

[60] C. Sfienti et al, Phys Rev. Lett. **102** (2009) 152701

[61] N. Buyukcizmeci et al, Eur. Phys. Jour. **A 25** (2005) 57

[62] A.S. Goldhaber, Phys. Rev. **C 17** (1978) 2243(R)

[63] G. Lanzanò et al, Phys. Rev. **C 58** (1998) 281

[64] B.E. Hasselquist et al, Phys. Rev. **C 32** (1985) 145

[65] S. Albergo et al, Nuovo Cim. **A 89** (1985) 1

[66] W. Trautmann et al, Phys. Rev. **C 76** (2007) 064606

[67] M.B. Tsang et al, Phys Rev. Lett. **78** (1997) 3836

[68] A. Kolomiets et al, Phys. Rev. **C 54** (1996) 472(R)

[69] D.J. Morrissey et al, Phys. Lett. **B 148** (1984) 423

[70] V. Serfling et al, Phys Rev. Lett. **80** (1998) 3928

[71] V.E. Viola and R. Bougault, Eur. Phys. Jour. **A 30** (2006)

[72] R. De Souza et al, Eur. Phys. Jour. **A 30** (2006)

[73] N. Marie et al, Phys. Lett. **B 391** (1997) 15

[74] H. Nifenecker et al, Nucl. Phys. **A 447** (1985) 533

[75] H. Delagrange and J. Peter, Nucl. Phys. **A 471** (1987) 111

[76] W. Bohne et al, Zeit. Phys. **A 347** (1993) 135

[77] J. Hauger et al, Phys. Rev. **C 57** (1998) 764

[78] A. Chibhi et al, Phys. Rev. **C 43** (1991) 652

[79] P. Figuera et al, Zeit. Phys. **A 352** (1995) 315

[80] B.A. Li and W.U. Schröder, *Isospin Physics in Heavy Ion Collisions at Intermediate Energies*, (Nova Science Publisher, 2001)

[81] V. Baran et al, Phys. Rep. **410** (2005) 335

[82] Bao-An Li et al, Phys. Rep. **464** (2008) 113

[83] E. Persico, *Gli Atomi e la loro energia*, (Zanichelli, Bologna 1970)

[84] See the website: http://www.fynu.ucl.ac.be

[85] B.A. Li, G.C. Yong and W. Zuo, Phys. Rev. **C 71** (2005) 014608

[86] M. Colonna et al, Nucl. Phys. **A 580** (1994) 212

[87] M. Papa et al, Phys. Rev. **C 64** (2001) 024612

[88] A. Ono and H. Horiuchi, Phys. Rev. **C 53** (1996) 2341

[89] M. Papa and G. Giuliani, Eur. Phys. Jour. **A 39** (2009) 117

[90] M. Papa et al, Journ. Comp. Phys. **208** (2005) 403

[91] B. Gatty et al, Nucl. Phys. **A 253** (1975) 511

[92] O.V. Lozhkin and W. Trautmann, Phys. Rev. **C 46** (1992) 1996

[93] D. V. Shetty et al, Phys. Rev. **C 68** (2003) 054605

[94] M. Di Toro et al, Eur. Phys. Jour. **A 30** (2006) 65

[95] J. Lukasik et al, Phys. Rev. **C 55** (1997) 1906

[96] J. Tõke et al, Phys. Rev. Lett. **75** (1995) 2920

[97] S. Piantelli et al, Phys. Rev. **C 74** (2006) 034609

[98] M. B. Tsang et al, Phys. Rev. Lett. **92** (2004) 062701

[99] E. Galichet et al, Phys. Rev. **C 79** (2009) 064614

[100] R. Lionti et al, Phys. Lett. **B 625** (2005) 33

[101] See the website http://pro.ganil-spiral2.eu/spiral2

[102] M. Farine et al, Zeit. Phys. **A 339** (1989) 363

[103] M. Colonna et al, Phys. Rev. **C 57** (1998) 1410

[104] P. Russotto et al, Phys. Rev. **C 81** (2010) 064605

[105] B. Borderie et al, *Contribution to the IWM2009 Conference* (2009) Catania, Italy

[106] F. Porto et al, Acta Phys. Pol. **B 31** (2000) 1489

[107] A. Pagano et al, Nucl. Phys. **A 734** (2004) 504

[108] N. Le Neindre et al, Nucl. Instrum. Meth. Phys. Res. **A 490** (2002) 251

[109] M. Alderighi et al, Nucl. Instrum. Meth. Phys. Res. **A 489** (2002) 257

[110] G. Politi, *Doctoral thesis*, Università di Catania, 1995

[111] G. Knoll, *Radiation Detection and Measurements*, (Wiley, NY 2006)

[112] S. Aiello et al, Nucl. Instrum. Meth. Phys. Res. **A 385** (1997) 306

[113] S. Aiello et al, Nucl. Instrum. Meth. Phys. Res. **A 369** (1996) 50

[114] Ad.R. Raduta et al, arXiv:1009.1267 (nucl-ex)

[115] Ad.R. Raduta et al, arXiv:1004.3234 (nucl-ex)

[116] A. Alberigi Quaranta et al, Nucl. Instrum. Meth. Phys. Res. **57** (1967) 131

[117] W. Seibt et al, Nucl. Instrum. Meth. Phys. Res. **113** (1973) 317

[118] J.B.A. England et al, Nucl. Instrum. Meth. Phys. Res. **A 280** (1989) 219

[119] W. Leo, *Techniques for Nuclear and Particle Physics Experiment*, (Springer 1998)

[120] M. Alderighi et al, IEEE Trans. Nucl. Sci. **52** (2005) 1624

[121] M. Alderighi et al, Nucl. Phys. **A 734** (2004) E88

[122] J.F. Liang et al, Phys. Rev. Lett. **91** (2003) 152701

[123] G. Cardella and M. Papa (for the Exochim collaboration), *Letter of Intent to LNS-PAC* (2009)

[124] G. Raciti et al, Nucl. Instrum. Meth. Phys. Res. **B 266** (2008) 4632

[125] G. Montagnoli et al, Nucl. Instr. Meth. Phys. Res. **A 547** (2005) 455

[126] S. Pirrone et al, Phys. Rev. **C 64** (2001) 024610

[127] P. Figuera et al, Il Nuovo Cimento **A 104** (1991) 251

[128] See the website: www.topag.de

[129] I. Lombardo et al, LNS Activity Report **2007** (2008) 111

[130] A. Musumarra et al, Nucl. Instr. Meth. Phys. Res. **A 612** (2010) 399

[131] O. Tarasov and D. Bazin, Nucl. Phys. **A 746** (2004) 411

[132] D. Shapira et al, Nucl. Instr. Meth. Phys. Res. **A 454** (2000) 409

[133] E. De Filippo et al, Nucl. Instr. Meth. Phys. Res. **A 342** (1994) 527

[134] M. Papa et al, Phys. Rev. **C 72** (2005) 064608

[135] E. Migneco et al, Nucl. Instr. Meth. Phys. Res. **A 314** (1992) 31

[136] R. Novotny, Nucl. Phys. **B 61** (Proc. Suppl.) (1998) 137

[137] T. Matulewicz et al, Nucl. Instr. Meth. Phys. Res. **A 378** (1996) 179

[138] K. Gunzert-Marx et al, Nucl. Instr. Meth. Phys. Res. **A 536** (2005) 146

[139] S. Cavallaro et al, Phys. Rev. **C 57** (1998) 731

[140] L. B. Yang et al, Phys. Rev. **C 60** (1999) 041602(R)

[141] M. V. Ricciardi et al, Nucl. Phys. **A 749** (2005) 122

[142] M. V. Ricciardi et al, Nucl. Phys. **A 733** (2004) 299

[143] E. Geraci et al, Nucl. Phys. **A 734** (2004) 524

[144] C. Cavata et al, Phys. Rev. **C 42** (1990) 1760

[145] F. Amorini et al, Phys. Rev. Lett. **102** (2009) 112701

[146] I. Lombardo et al, Nucl. Phys. **A 834** (2010) 458

[147] I. Lombardo et al, Int. Jour. Mod. Phys. **E 19** (2010) 1170

[148] P. Sapienza et al, Phys Rev. Lett. **73** (1994) 1769

[149] P.M. Milazzo et al, Eur. Phys. Jour. **A** **30** (2006)

[150] R. J. Charity et al, Phys Rev. Lett. **46** (1986) 1354

[151] L. Lassen et al, Phys. Rev. **C** **55** (1997) 1900

[152] T.M.V. Bootsma et al, Zeit. Phys. **A** **359** (1997) 391

[153] E. De Filippo et al, Acta Phys. Pol. **40** (2009) 1199

[154] M. Veselsky et al, Phys. Rev. **C** **62** (2000) 041605(R)

[155] W. P. Tan et al, Phys. Rev. **C** **64** (2001) 051901(R)

[156] R. Planeta et al, Phys. Rev. **C** **77** (2008) 014610

[157] I. Lombardo et al, Phys. Rev. **C** **82** (2010) 014608

[158] T.X. Liu et al, Phys. Rev. **C** **76** (2007) 034603

[159] I. Lombardo, G. Cardella and M. Papa (for the Exochim collaboration), *"isospin-I": proposal to LNS-PAC* (2008)

[160] I. Lombardo et al, Int. Jour. Mod. Phys. **E**, *in press*

[161] E. De Filippo (for the Exochim collaboration), *Program "deefit"* (2010)

Acknowledgements

Esprimo profonda gratitudine ed affetto a coloro che mi hanno seguito come *tutors* durante i periodi del dottorato e della laurea specialistica, ovvero il Prof. *Francesco Porto* e il Dr. *Giuseppe Cardella.* I loro consigli e moniti, oltre che la loro stima, sono stati fondamentali affinché il periodo del dottorato costituisse per me una proficua e piacevole occasione di approfondimento delle tecniche sperimentali e di analisi dati che risulteranno certamente utili nel futuro.

Ringrazio il Dr. *Angelo Pagano* per le sue osservazioni e le sue critiche costruttive su molti argomenti esposti in questa tesi, e i colleghi della collaborazione Exochim *Francesca Amorini, Enrico De Filippo, Elena Geraci, Laura Grassi, Jianlong Han, Elena La Guidara, Gaetano Lanzalone, Sara Pirrone, Giuseppe Politi, Francesca Rizzo, Paolo Russotto, Antonio Trifirò* e *Giuseppe Verde* per la loro amicizia ed i loro consigli. Al Prof. *Salvatore Cavallaro* va il mio ringraziamento per i consigli che mi ha fornito durante le attività di tutoraggio per gli studenti.

Le osservazioni del Dr. *Massimo Papa* hanno avuto notevole importanza; lo ringrazio per aver seguito gli sviluppi sperimentali di questo lavoro di tesi e di aver realizzato, assieme al Dr. *Gianluca Giuliani*, i calcoli con il modello CoMD-II.

Ho avuto modo di interagire molto con i ricercatori dei Laboratori Nazionali del Sud. In particolare, i suggerimenti e le discussioni avuti con i Dr. *Titti Agodi, Rosa Alba, Antonello Anzalone, Maria Colonna, Gianluigi Cosentino, Vincenzo Greco, Cettina Maiolino, Domenico Santonocito e Salvatore Tudisco* sono stati molto stimolanti. Sono riconoscente inoltre ai Dr. *Pierpaolo Figuera* ed *Agatino Musumarra* per i loro consigli circa l'ottimizzazione di microchannel plates, ed al Prof. *Massimo Di Toro* per i suoi commenti ad alcuni argomenti di questa tesi.

Ringrazio i Prof. *Elio Rosato* e *Mariano Vigilante* della Università Federico II di Napoli e *Paolo Guazzoni* e *Luisa Zetta* dell'Università di Milano per aver avuto l'opportunità di poter interagire con loro.

I acknowledge gratefully also Dr. Christian Beck, Bernard Borderie, Abdou Chibhi, Betty Tsang *and* Martin Veselsky *for many discussions about the subjects of this thesis.*

Un ringraziamento "monumentale" ai miei genitori *Luciano* ed *Alfonsina*, a mia sorella *Alice* ed alla mia famiglia che mi ha fortemente supportato in questi lunghi anni di carriera scolastica, vivendo con me i successi e gli insuccessi che essa ha comportato. Sono grato al Prof. *Marcello Persico* per la sua disponibilità e la sua amicizia. Un pensiero va infine a mio zio Maresciallo *Arturo D'Angelo*, prematuramente scomparso, per i suoi consigli disincantati e per il suo grande umorismo.